Understanding Nucleation and Growth of Crystalline Germanium Through in-situ Studies of the ec-LLS Technique

by

Quintin B. Cheek

A dissertation submitted in partial fulfillment
of the requirements for the degree of
Doctor of Philosophy
(Chemistry)
in The University of Michigan
2021

Doctoral Committee:

Professor Stephen Maldonado, Chair
Professor Bart Bartlett
Professor Emmanuelle Marquis
Assistant Professor Charles McCrory

Quintin Cheek

qbcheek@umich.edu

ORCID iD: 0000-0002-7622-7995

© Quintin Cheek 2021

ACKNOWLEDGEMENTS

I want to thank all my family and friends for their support throughout my academic journey. First, I would like to thank my parents, Keith and Amy Cheek, and my siblings, Eric and Emily Cheek. Next, I want to thank all my amazing friends: Nathanael Downes, Paul and Kelly Miller, Brian and Micaela White. Finally, I want to thank my wonderful girlfriend, Erin Gothier. All of you have earned a tremendous amount of my gratitude as I could not have accomplished this without you. Thank you for everything!

TABLE OF CONTENTS

LIST OF FIGURES

LIST OF SCHEMES

LIST OF TABLES

LIST OF EQUATIONS

ABSTRACT

The electrochemical liquid liquid solid (ec-LLS) technique is a novel method for the synthesis of crystalline inorganic covalent semiconductor materials. The crux of the technique involves using a liquid metal working electrode to serve both as a source of electrons for electrochemical reduction of a semiconductor precursor and as a growth solvent to facilitate the growth of crystalline semiconductor material. Ec-LLS combines the precise control of electrochemical reactions with the ability to furnish crystalline semiconductor material of melt crystal growth techniques. Previous research on ec-LLS focused on *ex-situ*, macroscale methods to identify methods to control crystal nucleation and growth, probed how the identity of the liquid metal influenced crystal morphology, and explored the possibility of alloying reactions between a group III liquid metal and group V precursor. These studies were significant and impactful, but several key questions remain.

This thesis describes multiple strategies to study directly ec-LLS growth processes using *in-situ* techniques. The central goal of this dissertation is to provide atomic-level insight into the nucleation and growth crystalline germanium (Ge) via ec-LLS. This thesis details the electrochemical synthesis and simultaneous characterization of crystalline Ge in both real-time and with high spatial resolution.

The first portion of this thesis details a general methodology for the study of electron beam stimulated ec-LLS nanowire growth via liquid cell transmission electron microscopy (LC-TEM). Specifically, Chapter 2 describes the use of liquid metal Ga and In nanodroplets for the growth of Ge nanowires at room temperature. A variety of conditions were explored including liquid metal nanodroplet surface condition, liquid metal nanodroplet size and density, formal concentration of dissolved GeO_2, and electron beam intensity. This work revealed that nanowire growth rate was limited by the heterogeneous reduction of dissolved GeO_2, the high activation barrier for

nucleation in ec-LLS, and the influence of growth rate on defect formation in the growing nanowires.

The second portion of this thesis focuses on the use of X-Ray Reflectivity (XRR) to investigate the liquid metal-liquid electrolyte interface during potentials commonly employed during ec-LLS. Chapter 3 probes the surface of a liquid mercury working electrode at potentials positive of the $4e^-$ reduction of GeO_2 to Ge^0. Three primary findings were revealed. 1) When the electrolyte only contained $Na_2B_4O_7$, a pristine mercury-electrolyte interface was observed. 2) When GeO_2 was introduced to solution, a solid adlayer formed on the surface of Hg when $E \geq$ -0.2 V vs. SCE. 3) When the applied potential was between -0.5 V and -0.9 V an anion adsorbate layer consistent was $HGeO_3^-$ was instead observed on the mercury surface. Chapter 4 shifts the focus to more negative potentials in the same system. Under these conditions, XRR was used to gauge the atomic level structure of the liquid Hg/liquid water interface during the growth of crystalline Ge by ec-LLS. A principal finding was that nucleation and growth occur in the near-surface region of the liquid metal rather than deep in the bulk. Nevertheless, the surface ordering of the liquid Hg was maintained throughout, indicating poor wetting of crystalline Ge by the liquid metal.

The final chapter of this thesis details unresolved work that could serve as future research pathways. Six different projects encompassing LC-TEM, XRR, and general growth strategies for group III-V semiconductor materials are outlined. These works serve to further elucidate the knowledge gaps present in ec-LLS.

CHAPTER 1

Introduction

1.1. Motivation

Many vital technologies in society including photovoltaic, energy conversion, and electronic devices depend on inorganic covalent semiconductor materials.[1-56-8] Obviously, material composition dictates basic properties like the nature (direct/indirect) of optoelectronic bandgaps.[12] The performance of inorganic, covalent semiconductors in these applications also depends strongly on their crystallinity, as properties like electron and hole mobility are strong functions of compositional and crystallographic purity.[10-11] For specific applications like rechargeable batteries, even the form factor of inorganic, covalent semiconductors (e.g. nanowire) dictates their efficacy.[1, 9]

The ability to control the composition, crystallographic, and morphological properties of semiconductor materials is a desirable aspect for any semiconductor synthetic method. Common synthesis techniques for crystalline covalent inorganic semiconductors include molecular beam epitaxy (MBE), metalorganic chemical vapor deposition (MOCVD), and vapor-liquid-solid (VLS) growth. While these techniques yield high purity and high-quality inorganic semiconductor materials, these methods lack another desirable attribute for an ideal semiconductor synthesis method. Simply, these methods are resource intensive, requiring high temperature, low pressures, generating toxic waste products, and require expensive infrastructure.[13-17] Accordingly, these particular methods have an inherently high fiscal and environmental costs.[18-19] The ideal synthetic methodology would retain the control afforded by these methods but eliminate their costs.

This thesis focuses on the development of a separate semiconductor synthetic tactic - electrochemical liquid liquid solid (ec-LLS) growth. ec-LLS and related techniques represent an

alternative strategy for synthesizing inorganic, covalent semiconductors with the potential for realizing high quality, tunable materials but without excessive infrastructure or cost.

1.2 The Electrochemical Liquid Liquid Solid Growth Process

ec-LLS growth processes are a relatively new method for semiconductor synthesis and crystal growth. ec-LLS is fundamentally an electrochemical method but is actually best described as a hybrid mixture of traditional electrodeposition and non-electrochemical melt crystal growth (Figure 1.1). The dissolved oxidized precursor is electrochemically reduced to its zero-valent state. The now zero-valent atoms are dissolved into the liquid metal working electrode. The first two steps will continue until a sufficiently negative bias is no longer supplied to the electrode. Once a critical degree of dissolution is reached, nucleation occurs followed by the growth of a crystalline solid.[20]

The hallmark of the ec-LLS technique is the replacement of the solid working electrode with a liquid metal working electrode for electroreduction and crystal growth. This subtle change affords the benefits of the ambient conditions and precision control of traditional electrodeposition with the ability to furnish crystalline semiconductor material at otherwise low temperatures.[21-25]

In “conventional” electrodeposition, an oxidized semiconductor precursor dissolved in an electrolyte is reduced to its zero-valent state onto a solid working electrode. The advantages of ‘conventional’ electrodeposition are that it can be performed under ambient conditions and with relatively simple apparatus.[26] Specifically, only a container to hold the electrolyte (i.e. a beaker), at least two electrodes, and a source to generate an electromotive force, *emf*, (i.e. a potentiostat or even just a battery) are required to carry out the technique. However, for semiconductors, the resultant material is often not crystalline if performed at or near ambient temperatures. Subsequent thermal annealing is thus required in order to render a crystalline material.[27-29]

An alternative methodology is the family of melt crystal growth techniques. Melt crystal growth techniques are based on liquid metals as growth solvents that facilitate nucleation and growth of crystals. Melt crystal growth is primarily useful for the direct synthesis of crystalline covalent inorganic semiconductor materials.[30-32] However, the use of a temperature gradient to regulate the reaction results in a loss of control over the crystal growth process compared to electrochemical techniques.

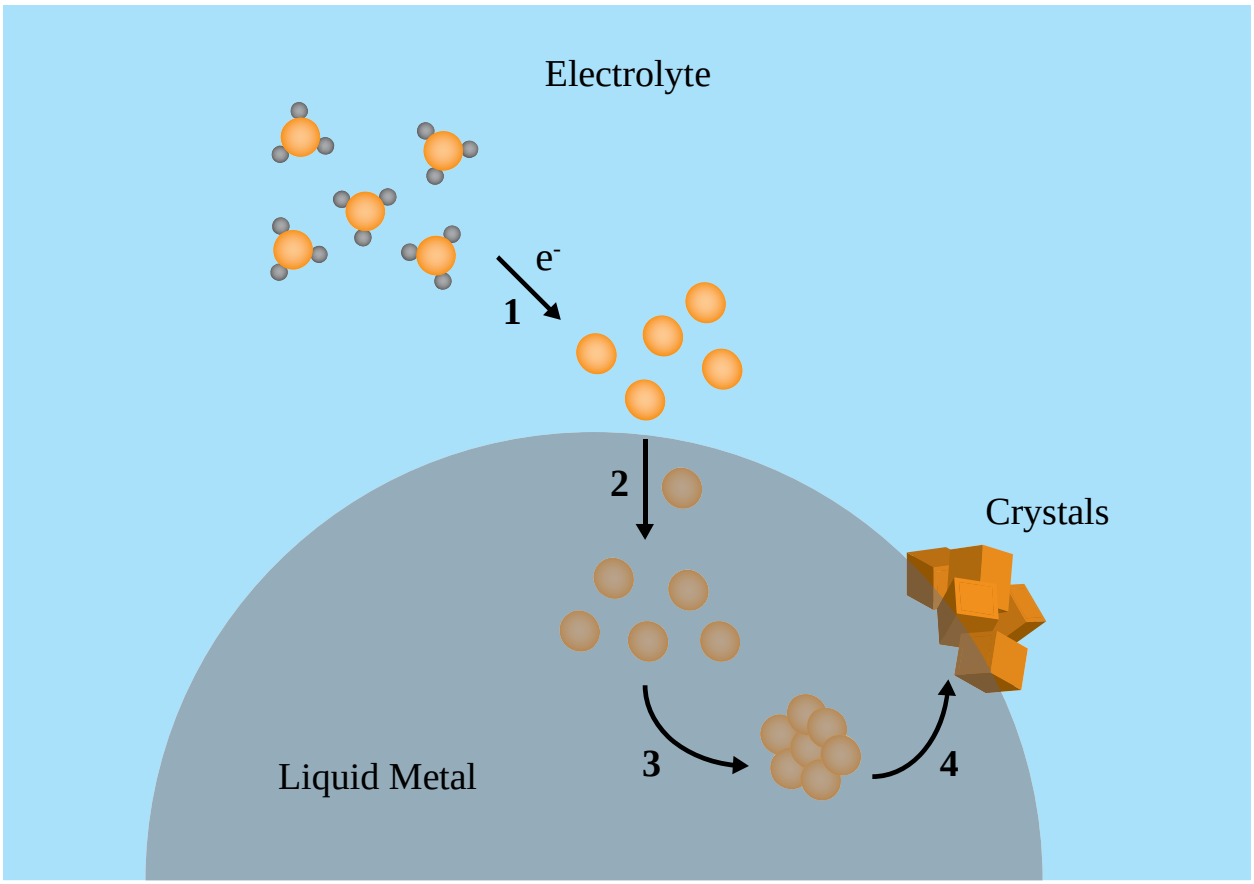

Figure 1.1 Schematic depiction of the steps involved in the growth of crystalline semiconductor material via ec-LLS. The four minimum steps required for ec-LLS to proceed are illustrated. (1) reduction of the oxidized precursor adlayer to a zero-valent state. Following the reduction of the oxidized precursor, steps (2), (3), and (4) illustrates dissolution of the zero-valent semiconductor into the liquid metal electrode, homogenous nucleation of a crystal seed, and finally growth of crystalline semiconductor material.

Since our lab first established the ec-LLS technique in 2011,[21] several points were recognized by previous undergraduate, graduate, and postdoctoral researchers in the Maldonado group. First, the ec-LLS technique supports both homogeneous and heterogenous growth processes. This aspect is ultimately determined by the diffusivity of the zero-valent atoms through the liquid metal bulk. Second, a large degree of supersaturation is observed in ec-LLS semiconductor growth. Third, the identity of the liquid metal working electrode can strongly influence the morphology of the resultant crystals. Fourth, the synthesis of group VI and group III-V are attainable. These points are individually detailed below.

A report by DeMuth et al. investigated methods into controlling the nucleation and growth of crystalline Ge in a liquid metal GaIn alloy.[33] An important aspect to the process of crystal growth is that of supersaturation. Supersaturation can be thought of as the driving force for crystal nucleation and growth.[34] Furthermore, the degree of supersaturation directly influences the rate of nucleation, the rate of crystal growth, and the crystal size. Specifically, as the level of supersaturation increases the rate of nucleation and growth will also increase while the crystal size will decrease.[35-36] Therefore, a better understanding of supersaturation as it relates to ec-LLS would be advantageous in increasing our control over the crystal growth process.

A series of ec-LLS experiment were performed in which the liquid metal thickness and temperature of the electrochemical cell were varied to ascertain which conditions resulted in microwire growth. The governing hypothesis was that the type of nucleation (ie: homogenous vs. heterogenous) which took place was related to how rapidly the zero-valent atoms could reach the semiconductor interface with respect to the local supersaturation. At liquid metal thicknesses, *t*, less than 16 μm, heterogenous nucleation at the bottom interface was observed at all analyzed temperatures (Figure 1.2). When *t* was moderately larger, elevated temperatures (≥60^{o} C) were required to promote heterogenous nucleation, otherwise homogenous nucleation would occur resulting in bulk crystal growth at the surface of the liquid metal electrode. When the liquid metal thickness was ≥ 27 μm homogenously nucleation occurred at all temperatures analyzed. These observations supported the hypothesis that heterogeneous nucleation could be preferentially favored when the liquid metal thickness was below a critical threshold value. The inferred reason was that smaller thicknesses prevented the supersaturation levels from becoming so high that homogeneous nucleation occurred.

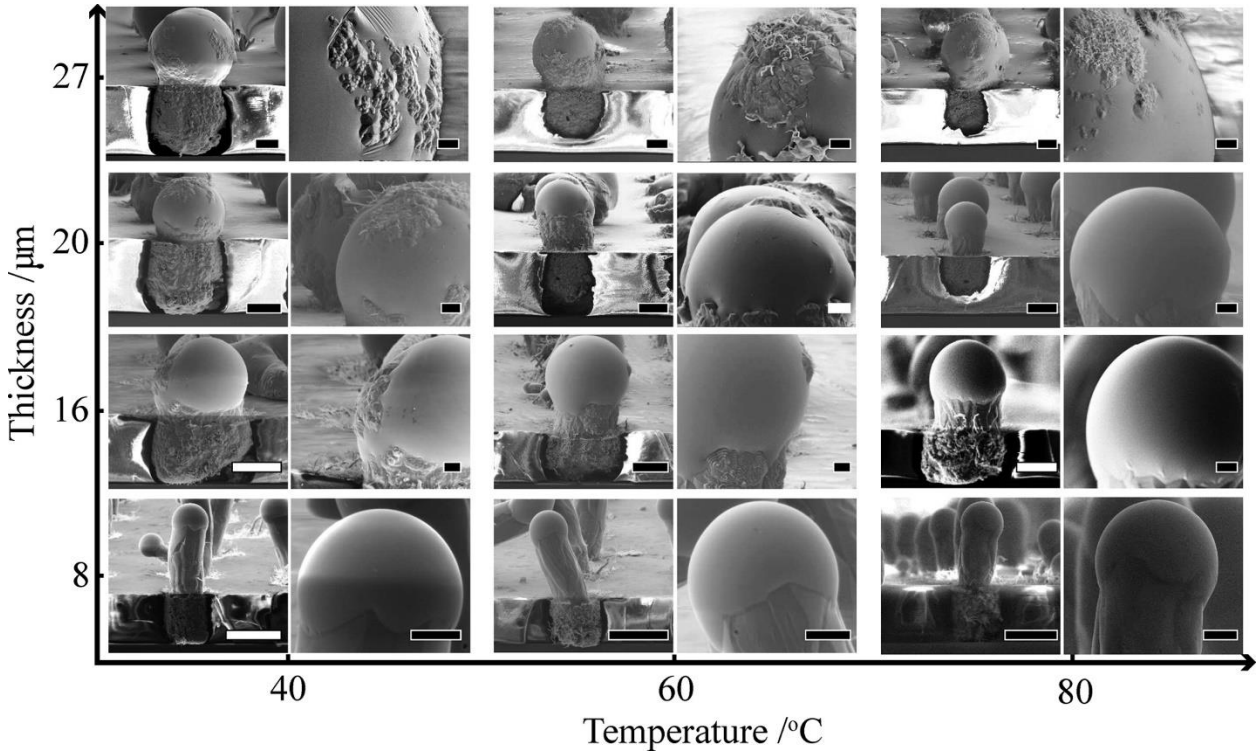

Figure 1.2 Scanning electron micrographs of Ge ec-LLS experiments performed 0.01 M $Na_2B_4O_7$ + 0.05 M GeO_2 at E = −1.6 V for 30 min at T = 40, 60, and 80 °C and with several e-GaIn thicknesses. In each pair, the scale bar for the left image is 10 μm and for the right image is 2 μm. Figured adapted from reference 33.

DeMuth separately performed multiple ex-situ analyses studies to ascertain the growth rate and supersaturation of Ge in the liquid metal prior to semiconductor nucleation in ec-LLS. To estimate the growth rate, Ge microwires were grown for increasing lengths of times (3, 5, 10, and 30 minutes) at equivalent potentials followed by cross section scanning electron microscopy to ascertain the average length of each nanowire array. The growth rate of crystals was found to be linear with a magnitude of ~0.033 μmol min^{-1} at 80° C. The supersaturation was estimated through modeling the flux of Ge^0 into the liquid metal using a 1D finite difference model and was found to be approximately 10^2 higher than the equilibrium concentration. This work provided evidence that supports the hypothesis that the speed of solute diffusion with respect to the local supersaturation dictates nucleation inside the liquid metal. This work also suggested that ec-LLS operates under high supersaturations which could explain the high level of impurities and defects commonly observed in nanowires grown in this way.

A separate report by Acharya et al. focused on the impact of the composition of the liquid metal on ec-LLS.[37] In this work, the fraction of In in liquid GaIn alloys was tuned from 3.1% - 47.6%. These experiments revealed that In content did not influence the Ge crystal growth rate since in each set of experiments the average length of Ge microwires were identical. However, the indium content did affect the wetting angles of the droplet on the emerging Ge crystals, with lower indium contents causing a greater wetting angle. (Figure 1.3) This observation indicates that even at low concentrations of In in the liquid GaIn alloy, there must be some degree of In at the liquid metal-solid Ge interface which can influence the wetting angle.

For an array of microwires grown by ec-LLS, the pitch of the array was separately tuned. Increasing the pitch allowed for each microdroplet to experience less diffusional field overlap, leading to an increase in the growth rate. For example, with a 110 μm pitch, 600 s ec-LLS reaction time was required to reach approximately 50 μm. With a 30 μm pitch, a total time of 1800 s was required to reach the same length.

Atom probe tomography (APT) experiments performed to gauge the level of dopant concentration in crystals grown by ec-LLS. For Ge grown with $Ga_{1-x}In_x$ (x = 16.8 at%) alloys, the Ga concentration exceeded 10 at% while the In concentration was >0.1 at%, indicating that the composition of the liquid metal did not directly translate to the residual metal content in the as-grown crystals. Similar observations were seen previously.[33, 38]

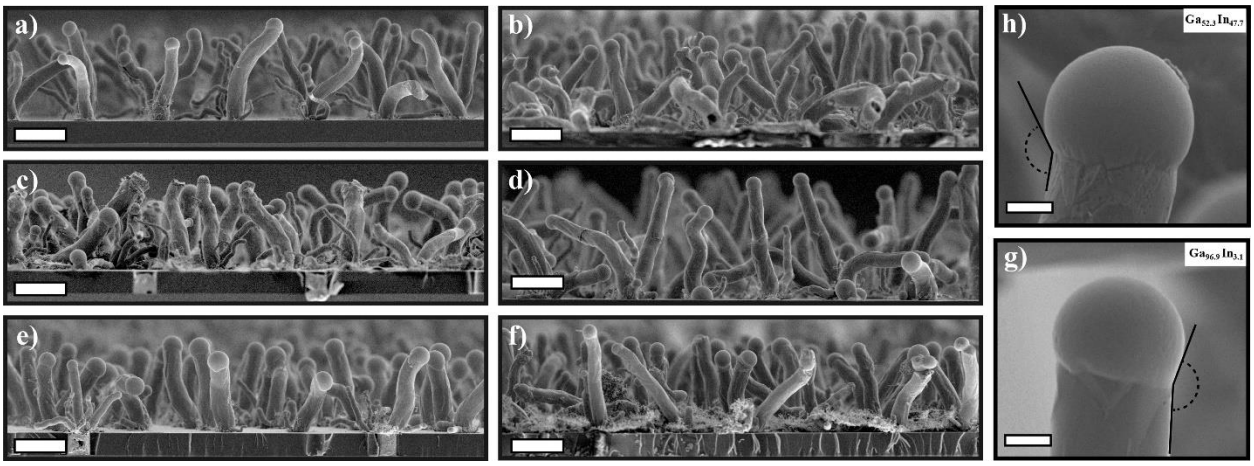

Figure 1.3 Cross-section scanning electron micrographs of Ge microwire ec-LLS experiments performed in an electrolyte containing 0.05 M GeO_2 and 0.01 M $Na_2B_4O_7$ (aq) at T = 80 °C and E = −1.6 V using different compositions of $Ga_{1-x}In_x$ liquid metal, where microdroplet array pitch = 30 μm and t = 1800 s. x = (a) 3.1 at. %, (b) 6.3 at. %, (c) 9.7 at. %, (d) 13.2 at. %, (e) 24.6 at. %, and (f) 47.6 at. %. Scale bars: 20 μm. Additional higher magnification scanning electron micrographs depicting the wetting of the top of the Ge microwire by the corresponding liquid metal droplet are shown for (g) x = 3.1 and (h) x = 47.6 atom %, respectively, with apparent wetting angles of 160° and 145°, respectively. Scale bars: 2 μm. Figured adapted from reference 37.

Separate work explored the efficacy of a different liquid metal based on liquid In.[38] A BiIn eutectic alloy was employed in ec-LLS determine if in behaves differently as a growth solvent in the presence of different metals. An important observation in these studies was the observation of a change in the crystal morphology when In was alloyed with Bi (Figure 1.4). Through a combination of bright field and dark field transmission electron microscopy (TEM), it was concluded that the coiled portion of the nanowire was single crystalline. That is, the coil was a direct result of how the liquid metal wets the emerging crystal. Despite the change in the morphology, these crystals were still highly doped with residual liquid metal at comparable levels as seen previously. However, in this case, indium was not the primary impurity, unlike the case with liquid GaIn. This work has shown that e-BiIn can be used an electrode for the growth of microwires via ec-LLS. Furthermore, the physical properties of the alloy atoms have a strong effect on the morphology and degree of impurities.

Two separate reports led by Fahrenkrug and DeMuth, respectively, explored the deposition of Group V metals into group III metal electrodes.[39-40] The premise was that the negative ΔG_{rxn} values for the reaction between group III and group V elements facilitate the growth of crystalline III-V semiconductors by ec-LLS. Both arsenic and antimony were explored as the group V metal, deposited onto either a gallium or indium working electrode. A series of electrochemical experiments were performed in which 3 parameters were altered to determine the conditions in which group III-V material could be successfully grown: 1) the concentration of dissolved Group V element, 2) the temperature in the electrochemical cell, and 3) the applied potential. Both papers proved the feasibility to grow the respective III-V material in their system. The most significant parameter to control was the nucleation density of group V material on electrode. If the nucleation density was too high, as effected by either high formal concentrations of the group V precursor in the electrolyte or a large applied overpotential, then the deposited material would form aggregates of elemental group V clusters on the surface of the electrode, preventing any alloying reaction.

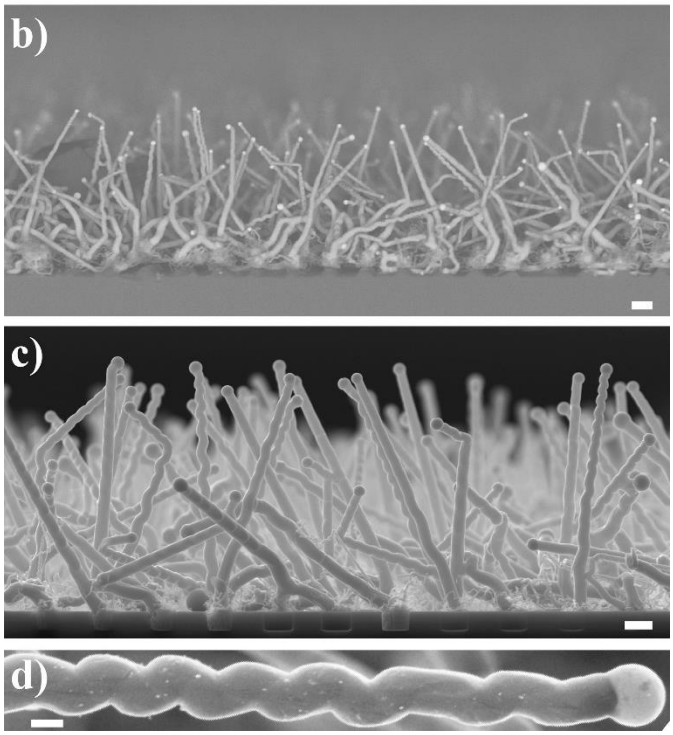

Figure 1.4 (b, c) Scanning electron micrographs of Ge nanowires prepared by ec-LLS as in (a) at (b) low and (c) higher magnification cross-sectional view of a Ge nanowire film. (d) High magnification of individual Ge nanowire highlighting a coiled section. Scale bars: (b) 1 μm, (c) 1 μm, and (d) 250 nm, respectively. Figured adapted from reference 38.

However, if the experimental conditions were chosen properly such that group V clusters did not accumulate on the electrode surface, then crystalline group III-V semiconductors could be grown, as confirmed by Raman and XRD analysis. These works jointly showed that the electrode material could serve even more roles than just as the source of electrons and as crystal growth solvents in ec-LLS.

While the ec-LLS technique has been studied exhaustively through a myriad of ex-situ characterization methods, knowledge gaps still exist regarding ec-LLS which hinder its efficacy to be used as a primary synthesis method for crystalline semiconductor materials. Five outstanding questions about ec-LLS remain:

1) Can the degree of supersaturation in ec-LLS be directly probed? If so, what is the minimum level required to initiate nucleation and growth?
2) Is the growth rate of ec-LLS limited by electrochemical or chemical factors?
3) How does the growth rate influence the concentration of defects in micro- and nanowires? Can these defects be mitigated?
4) Is the liquid metal-liquid electrolyte interface pristine? Does that matter to the efficacy of ec-LLS process?
5) Where and how do crystal nucleation and growth occur in ec-LLS?

To answer these questions, directed studies that address each area are warranted. To be clear, ex-situ analyses will not be sufficient to advance our present understanding. Rather, dynamic and in-situ probes that provide microscopic detail are necessary. Accordingly, the work presented in this thesis focuses on the synthesis and simultaneous characterization of crystals using *in-situ* techniques to elucidate the finder details of ec-LLS processes.

1.3 Relevant In-Situ Techniques

1.3.1 Liquid Cell Transmission Electron Microscopy (LC-TEM)

LC-TEM is a prime candidate for studying ec-LLS due to its high temporal and spatial resolution.[41-43] Several excellent reviews on this technique are available,[42, 44-47] and only the salient points relevant to this thesis are described here.

LC-TEM is commonly employed to study the electrochemical growth of crystalline nanomaterials. One example by the Zheng group who studied the transition of a platinum

nanoparticle to a nanocube.[48] That work focused on the direct observation of a growing nanocrystal to advance our understand of the factors affect terminal nanocrystal shapes. Through modulation of the surface ligand concentration, that study observed how both surface kinetics and thermodynamics influence the growth rate of varying growth facets of a Pt nanocrystal. Separate work investigated the growth mechanism of bimetallic nanoparticles using LC-TEM.[49] PtNi nanoparticles were studied due to their value in fuel cells, sensors, and as catalysts. The experimental set up involved dissolving equimolar concentrations of both $Pt(acac)_2$ and $Ni(acac)_2$ in oleylamine and oleic acid. Upon electron beam irradiation PtNi nanoparticles were observed to grow through a two-step growth process. A unique growth pathway was observed in which nickel dendrites form and then are immediately consumed by nearby platinum atoms to yield PtNi nanoparticles.

These studies highlight how LC-TEM is enabling for the study of nucleation and growth dynamics of crystalline nanowires in ec-LLS. However, such experiments require appreciation of the experimental details. LC-TEM can be performed with a variety of equipment, including dedicated TEM microscopes fitted with special apparatus. However, a recent development is the emergence of specialized probe tips that allow liquid experiments in otherwise standard TEM instruments. While many liquid cell technologies exist,[50-52] the technology addressed in this thesis is based on chip set which constrain a thin layer of liquid between two electron transparent membranes (Figure 1.5). The chipset is composed of two silicon wafers which serve as structural support with a set of o-rings in the middle to seal the cell against leaks. A dielectric spacer layer is patterned onto the bottom chip in the set which is dictates the initial thickness of the liquid layer. The most significant feature of the liquid cell are of course the electron transparent windows. The most common window type is amorphous SiN_x with a thickness ranging from 30-50 nm. These windows are thin enough to be electron transparent without fracturing inside the vacuum of the microscope column. The window material is made amorphous to avoid any scattering of the electron beam caused by the planes in a crystalline material. When the imaging beam of an electron strikes the aqueous solution of the liquid cell, a myriad of side products are formed as a result of the radical chemistry induced by the electron beam irradiation.[42, 44] Solvated electrons can be generated,[53-54] although they have short lifetimes on the order of microseconds. They are so reactive that they can perform electrochemical reduction reactions of oxidized precursor species in solution.[55-57]

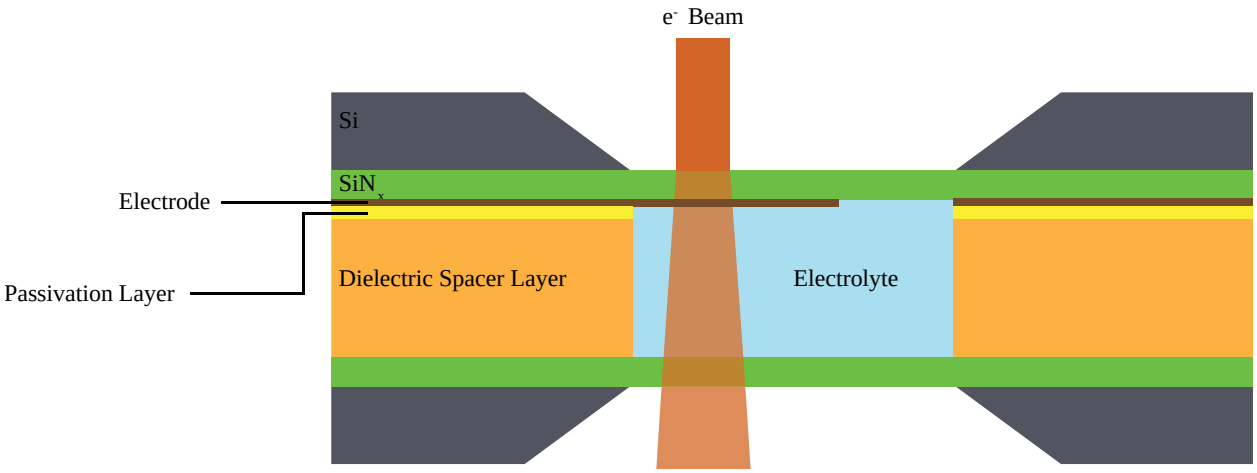

Figure 1.5 Cross sectional schematic of the liquid TEM cell used in this work. Not drawn to scale.

The generation of solvated electrons offers a convenient method for the study nanomaterial growth processes without the use of any external equipment. Understanding the effects of electron beam irradiation on the solution chemistry of the system is of the utmost importance. In water, many reactive species with relatively long lifetimes such as OH^-, H_3O^+, and H_2O_2 reach ~10^{-4} M concentrations within ~10^{-1} s of irradiation.[54]

These species can cause complications by way of altering the pH or otherwise directly chemical reactions with the materials of interest. While heating caused by the primary beam is negligible at higher voltages using TEM, low voltage STEM probing can cause localized heating on the order of 30°-70° C.[58] Ultimately, the degree to which the electron beam influences the solution chemistry will be directly proportional the dose rate of the electron beam. A first order estimate of the electron beam dose rate, ψ, is given below in equation 1.1.[59]

$$\psi = \frac{10^5 SI}{\pi a^2}\left(1 + \frac{t}{\lambda}\right) \qquad (1.1).$$

where the dose rate is in units of Gy s^{-1}, S is the density normalized stopping power (MeV cm^2 g^{-1}) of the solution, I is beam current (C s^{-1}), a is the beam radius (cm), t is the sample thickness (nm), and λ is the mean free path for the electrons (nm). These parameters can then be tuned to adjust the dose rate to conditions which are amenable to the experiment. A separate option to protecting sample from the reactive species generated by irradiation is to employ a radical scavenger.[60] These functional groups rapidly react with specific radicals to remove them from solution. For example, halide ions are effective hydroxyl scavengers and iodo- groups are efficient at quickly reacting with hydrogen radicals. Buffers can also be setup to help resist any changes in pH of the solution.

A second aspect to take into account is the degree of window bulging due to the large pressure differential between the vacuum of the microscope column and the pressure of the solution inside the cell.[61] Window bulging is a function of both window material and geometry and will cause differences in the liquid layer thickness across different positions in the cell. An increase in the liquid thickness could be problematic for two reasons. As shown in equation 1.1, an increase in the thickness, t, will cause an increase in the dose rate which could be detrimental to the materials of interest. Furthermore, a thicker liquid layer will result in a greater degree of chromatic aberration from electron scattering causing a loss of resolution.[62]

Lastly, the position of the studied material also plays a role in the resolution. For LC-TEM, the best resolution will be obtained when the sample is situated at the exit side of the cell and when the sample is on the beam entrance side of the chip.[42] These aspects will ensure that the scanning probe is not broadened before interacting with the sample.

1.3.2 In-situ Electrochemical X-Ray Reflectivity (XRR)

X-ray Reflectivity (XRR) is a powerful technique that has been essential in validating the fundamental nature of the near-surface structure of liquid metals in contact with air and water.[63-66] Unlike molecular liquids (e.g. water, ethanol, acetonitrile), liquid metals were observed to exhibit an ordered structure at the surface which decays monotonically into the bulk (Figure 1.6). This ordering is a result of the abrupt change in electron density at the liquid metal – vacuum/vapor/liquid electrolyte interface. The liquid metal restricts movement of atoms near the surface to screen itself from the low electron density medium at the surface.

In the most general sense, XRR measurements collect the specularly reflected photons from an interface as a function of the incident angle. The combination of shallow angles and X-ray photons renders the intensity of the reflected signal as highly sensitive to the electronic structure of the surface. Therefore, any deviations of the interface from the ideal case, e.g. the presence of an adlayer, can be identified through changes in the measured x-ray intensity. Following collection of the angle-dependent XRR, electron density profiles along the surface normal vector can be generated on the angstrom scale.

XRR curves collected from liquid-metal/liquid-electrolyte interfaces must first be normalized. In order to properly normalize the raw data, the average intensity for the primary beam under similar experimental conditions (e.g. same electrolyte composition, liquid metal electrode, electrochemical cell) must be calculated. The intensity of the primary beam is determined for each relevant XRR curve and the average intensity can be calculated. The pertinent raw data is then normalized by the average primary such that the intensity values below the critical angle are equal to one (total external reflection).

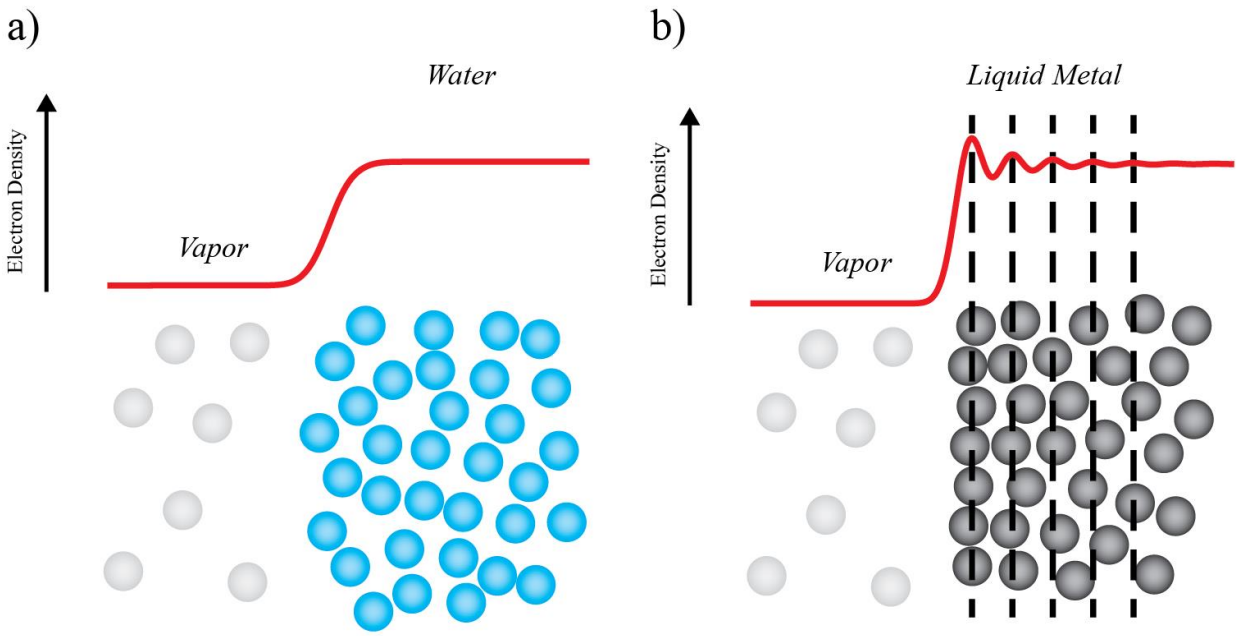

Figure 1.6 a) Schematic illustration of a vapor-water interface and the corresponding electron density profile. b) Schematic illustration of a liquid metal-water interface exhibiting surface ordering of the liquid metal and the corresponding electron density profile.

Following proper normalization, the data must be fit with a specific model to infer the corresponding electron density profile along a vector perpendicular to the surface normal. The distorted crystal model is the most popular model for fitting such data and describes the liquid metal interface as an infinite stack of ordered atomic layers with an ordering that decays monotonically into the bulk where it becomes traditionally liquid-like. Hg has been extensively studied by XRR with this model,[67-70] highlighting surface structure distinct from other liquid metals like gallium or molten indium.[70]

Two modifications are commonly employed to fit XRR curves from liquid mercury interfaces (Figure 1.7). The first approach is known as the "First-Layer model" that includes a term which describes the elector density of the first layer of mercury atoms in the atomic stack (Equation 1.2).[71] The second approach is known as the "Adlayer model" adds a low-density adlayer to the mercury surface to modulate the electron density (Equation 1.3).[72] The work presented in this thesis utilizes both approaches which are described by the following equations:

$$\frac{\langle\rho_e(z)\rangle}{\rho_{e,Me}} = \frac{1}{2}\frac{\rho_{e,H_2O}}{\rho_{e,Me}}\left(1-\mathrm{erf}\left(\frac{z-z_{H_2O}}{\sigma_{H_2O}\sqrt{2}}\right)\right) + \frac{d\rho_{fi}}{\rho_{e,Me}\sigma_i\sqrt{2\pi}}e^{\frac{-\left(z-z_{fi}\right)^2}{2\sigma_i^2}} + \sum_{n=1}^{\infty}\frac{d}{\sigma_n\sqrt{2\pi}}e^{\frac{-(z-nd)^2}{2\sigma_n^2}} \quad (1.2).$$

$$\frac{\langle\rho_e(z)\rangle}{\rho_{e,Me}} = \frac{1}{2}\frac{\rho_{e,H_2O}}{\rho_{e,Me}}\left(1-\mathrm{erf}\left(\frac{z-z_{H_2O}}{\sigma_{H_2O}\sqrt{2}}\right)\right) + \frac{d\rho_{ad}}{\rho_{e,Me}\sigma_{ad}\sqrt{2\pi}}e^{\frac{-\left(z-z_{ad}\right)^2}{2\sigma_{ad}^2}} + \sum_{n=1}^{\infty}\frac{d}{\sigma_n\sqrt{2\pi}}e^{\frac{-(z-nd)^2}{2\sigma_n^2}} \quad (1.3).$$

The first term of each equation describes the electron density of the liquid electrolyte. Here, ρ_{e,H_2O} and $\rho_{e,Me}$ describe the electron density of the electrolyte and metal electrode respectively, where z_{H_2O} & σ_{H_2O} describe the position and width of the electrolyte front. The final term is also identical for each model and describes the electron density of the liquid metal. In this term *d* is the atomic layer spacing after the second metal layer and σ_n is the root mean displacement of the *n*th layer where $\sigma_n = \sqrt{n\sigma_b^2 + \sigma_i}$, where σ_i describes the roughness intrinsic to all layers and σ_b describes the rate by which the roughness increases into the bulk of the mercury. The second term either describes the electron density of the first atomic layer of the mercury electrode or the mercury surface adlayer for the first-layer and adlayer models respectively. For the first-layer model, ρ_{fi} is the amplitude of the first layer, *d* is the atomic layer spacing, z_{fi} is the position of the first layer. For the adlayer model, ρ_{ad} & σ_{ad} are respectively the amplitude and root mean square displacement of the mercury adlayer while z_{ad} is the position of the adlayer.

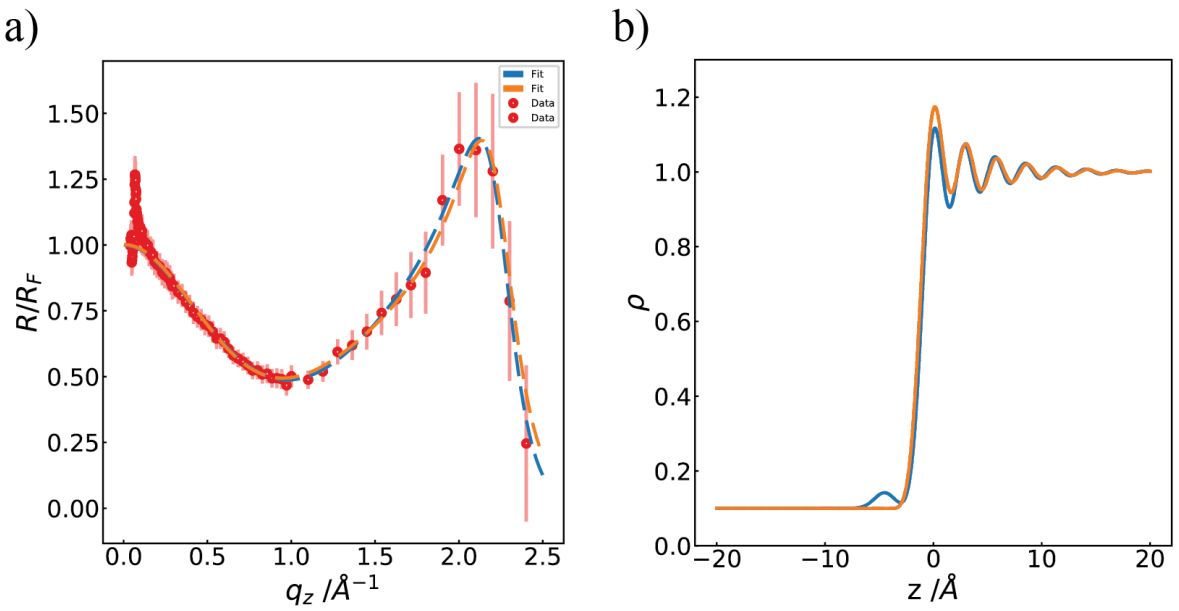

Figure 1.7 Comparison of the 'Hg Adlayer' (Blue) and 'First Layer' (Orange) models. a) X-ray reflectivity form Hg normalized to the Fresnel reflectivity and b) corresponding electron density profiles.

In Figure 1.7b, the "Adlayer" model is represented by the curve in blue. Here, a distinct gaussian representing the Hg adlayer can be seen in the electron density profile centered around q_z = 4 Å^{-1}. The "First Layer" model depicted here in orange lacks this distinct gaussian. Instead, this model features an augmented first layer of the atomic Hg stack as shown in first peak in the oscillation at q_z = 0 Å^{-1}. In both models, the electrolyte and bulk Hg layering regions are treated identically.

XRR is frequently used to study adlayer formation on the surface of liquid metals. One specific example explored how the presence of an adlayer facilitates the growth of 3D crystalline material, i.e. a PbFBr adlayer.[68] At negative applied potentials, Br^- anions readily adsorbed to the surface of the Hg electrode. To balance out the negative charges of this Br^- adlayer, 5-layer unit cell involving Pb^{2+} cations was readily observed through and understood from the collected XRR data.

1.4 Summary of Thesis Contents

The work presented herein focused on the study of crystalline Ge nucleation and growth via the ec-LLS process using two separate *in-situ* techniques. Six key questions were targeted and are addressed to varying levels of success in this work:

1) What conditions are necessary to carry out the study of Ge nanowire growth via ec-LLS inside a liquid TEM cell?
2) Can the level of supersaturation in ec-LLS be directly measured?
3) What is the rate limiting step in ec-LLS?
4) How does the propensity for defects scale with growth rate?
5) Is there evidence for adlayer formation on the surface of the liquid metal working electrode employee in ec-LLS before crystalline Ge nucleation and growth occurs?
6) Does crystalline semiconductor nucleation and growth occur near the ordered surface of the liquid metal or deep into the bulk?

Chapter 2 describes our group's first in-situ TEM study of ec-LLS reactions. Specifically, the electron beam of the TEM was used to induce growth of Ge nanowires from nanodroplets of gallium and indium by ec-LLS. Liquid metal nanodroplets were first synthesized through the reduction of M^{3+} ions via electron beam irradiation, where M is Ga or In. Next, a solution

containing dissolved GeO_2 was injected into the liquid cell. A variety of conditions were explored, including liquid metal nanodroplet surface condition, liquid metal nanodroplet size and density, formal concentration of dissolved GeO2, and electron beam intensity. The cumulative observations from a series of videos recorded during growth events suggested the following points. First, the conditions necessary for initiating nanowire growth at uncontacted liquid metal nanodroplets in a liquid TEM cell indicate the process was governed by solvated electrons generated from secondary electrons scattered by the liquid metal nanodroplets. Second, the surface condition of the liquid metal nanodroplets was quite influential on whether nanowire growth occurred and surface diffusion of Ge adatoms contributed to the rate of crystallization. Third, the Ge nanowire growth rates were limited by the feed rate of Ge to the crystal growth front rather than the rate of crystallization at the liquid metal/solid Ge interface. Fourth, the Ge nanowire growths in the liquid TEM cell occurred far from thermodynamic equilibrium, with supersaturation values of 10^4 prior to nucleation.

Chapter 3 focuses on the study of the surface of the liquid metal working electrode *before* the deposition of solid Ge occurs via ec-LLS. X-Ray Reflectivity (XRR) curves were collected from a liquid Hg pool electrode which was immersed in a solution containing dissolved GeO_2 while being biased at potentials positive of the 4 e^- reduction of GeO_2. A series of experiments were performed in both a pure 100 mM $Na_2B_4O_7$ solution and one containing an additional 50 mM GeO_2 to ascertain both the quality of the Hg surface in an innocent electrolyte as well as the notable changes upon dissolution of GeO_2. The data presented speak to three conclusions. First, the $Na_2B_4O_7$ does not adsorb or cause any surface changes to the liquid Hg electrode. Second, a secondary oscillation indicative of an adlayer is observed at a q_z of 0.9 $Å^{-1}$ while the electrode is biased at the most positive potential tested. Lastly, even after removal of the apparent adlayer, the surface of the liquid metal Hg electrode does not return to its clean state that was observed in the pure $Na_2B_4O_7$ solution. These findings unveil that there are important steps in the ec-LLS process which occur even before the 4 e^- reduction of dissolved GeO_2 to Ge^0.

Chapter 4 continues with a series of *in-situ* XRR experiments now in the more negative regime of ec-LLS where Ge deposition and growth occur. The liquid metal working electrode in this experiment was biased to potentials equal to or more negative than the standard potential for the electroreduction of dissolved GeO_2. The experiments performed here revealed two primary insights regarding ec-LLS. First, the nucleation and growth of crystalline material during ec-LLS in mercury occurs in the surface

of the liquid metal as opposed to the bulk. Second, the surface laying observed in liquid metal mercury is maintained during the ec-LLS crystal growth process.

Chapter 5 summarizes the previous chapters in the thesis in addition to offering insight into unfinished work related to the *in-situ* studies of ec-LLS. Regarding unpublished/incomplete investigations, Chapter 5 outlines the status of each direction at the time of this writing. The status of LC-TEM experiments focused on Ge nanowires growth via ec-LLS under direct potentiostatic control is described. Additionally, data supporting the premise of electrochemical liquid solid solid (ec-LSS) nanowire growth is discussed. Further XRR experiments utilizing liquid metals other than Hg are described. One project investigates the surface structure and composition of a $Hg_{0.3}In_{0.7}$ liquid metal alloy as a function of the applied potential. A separate project explores the surface layering and oxide formation on a gallium bulk pool electrode. Finally, an effort to expand ec-LLS to the synthesis of III-VI semiconductors was attempted, with mixed results.

1.5 References

1. Chan, C. K.; Peng, H.; Liu, G.; McIlwrath, K.; Zhang, X. F.; Huggins, R. A.; Cui, Y., High-performance lithium battery anodes using silicon nanowires. *Nature Nanotechnology* **2008,** *3* (1), 31-35.
2. Garnett, E.; Yang, P., Light Trapping in Silicon Nanowire Solar Cells. *Nano Letters* **2010,** *10* (3), 1082-1087.
3. Razeghi, M.; Rogalski, A., Semiconductor ultraviolet detectors. *Journal of Applied Physics* **1996,** *79* (10), 7433-7473.
4. Razykov, T. M.; Ferekides, C. S.; Morel, D.; Stefanakos, E.; Ullal, H. S.; Upadhyaya, H. M., Solar photovoltaic electricity: Current status and future prospects. *Solar Energy* **2011,** *85* (8), 1580-1608.
5. Zhu, Z.; Song, Y.; Zhang, Z.; Sun, H.; Han, Y.; Li, Y.; Zhang, L.; Xue, Z.; Di, Z.; Wang, S., Vapor-solid-solid grown Ge nanowires at integrated circuit compatible temperature by molecular beam epitaxy. *Journal of Applied Physics* **2017,** *122* (9), 094304.
6. Gu, J.; Collins, S. M.; Carim, A. I.; Hao, X.; Bartlett, B. M.; Maldonado, S., Template-Free Preparation of Crystalline Ge Nanowire Film Electrodes via an Electrochemical Liquid–Liquid–Solid Process in Water at Ambient Pressure and Temperature for Energy Storage. *Nano Letters* **2012,** *12* (9), 4617-4623.
7. Shah, A.; Torres, P.; Tscharner, R.; Wyrsch, N.; Keppner, H., Photovoltaic Technology: The Case for Thin-Film Solar Cells. *Science* **1999,** *285* (5428), 692.
8. Wang, D.; Chang, Y.-L.; Wang, Q.; Cao, J.; Farmer, D. B.; Gordon, R. G.; Dai, H., Surface Chemistry and Electrical Properties of Germanium Nanowires. *Journal of the American Chemical Society* **2004,** *126* (37), 11602-11611.
9. Chan, C. K.; Zhang, X. F.; Cui, Y., High Capacity Li Ion Battery Anodes Using Ge Nanowires. *Nano Letters* **2008,** *8* (1), 307-309.
10. Mishra, U. K.; Singh, J., *Semiconductor device physics and design*. Springer: Dordrecht, The Netherlands, 2008; p xxiv, 559 p.
11. Sze, S. M.; Ng, K. K., *Physics of semiconductor devices*. 3rd ed.; Wiley-Interscience: Hoboken, N.J., 2007; p x, 815 p.
12. Otuonye, U.; Kim, H. W.; Lu, W. D., Ge nanowire photodetector with high photoconductive gain epitaxially integrated on Si substrate. *Applied Physics Letters* **2017,** *110* (17), 173104.
13. Cowley, A. H.; Jones, R. A., Single-Source III/V Precursors: A New Approach to Gallium Arsenide and Related Semiconductors. *Angewandte Chemie International Edition in English* **1989,** *28* (9), 1208-1215.
14. Laine, R. M.; Furgal, J. C.; Doan, P.; Pan, D.; Popova, V.; Zhang, X., Avoiding Carbothermal Reduction: Distillation of Alkoxysilanes from Biogenic, Green, and Sustainable Sources. *Angewandte Chemie International Edition* **2016,** *55* (3), 1065-1069.
15. Ma, L.; Yu, Z.; Ma, W.; Qing, S.; Wu, J., Assessment and Study on the Impact on Environment by Multi-crystalline Silicon Preparation by Metallurgical Route. *Silicon* **2019,** *11* (3), 1383-1391.
16. Tao, C. S.; Jiang, J.; Tao, M., Natural resource limitations to terawatt-scale solar cells. *Solar Energy Materials and Solar Cells* **2011,** *95* (12), 3176-3180.
17. Williams, E. D.; Ayres, R. U.; Heller, M., The 1.7 Kilogram Microchip: Energy and Material Use in the Production of Semiconductor Devices. *Environmental Science & Technology* **2002,** *36* (24), 5504-5510.
18. Demuth, J.; Fahrenkrug, E.; Ma, L.; Shodiya, T.; Deitz, J. I.; Grassman, T. J.; Maldonado, S., Electrochemical Liquid Phase Epitaxy (ec-LPE): A New Methodology for the Synthesis of Crystalline Group IV Semiconductor Epifilms. *Journal of the American Chemical Society* **2017,** *139* (20), 6960-6968.
19. Maldonado, S., The Importance of New "Sand-to-Silicon" Processes for the Rapid Future Increase of Photovoltaics. *ACS Energy Letters* **2020,** *5* (11), 3628-3632.

20. Fahrenkrug, E.; Maldonado, S., Electrochemical Liquid–Liquid–Solid (ec-LLS) Crystal Growth: A Low-Temperature Strategy for Covalent Semiconductor Crystal Growth. *Accounts of Chemical Research* **2015,** *48* (7), 1881-1890.
21. Carim, A. I.; Collins, S. M.; Foley, J. M.; Maldonado, S., Benchtop Electrochemical Liquid–Liquid–Solid Growth of Nanostructured Crystalline Germanium. *Journal of the American Chemical Society* **2011,** *133* (34), 13292-13295.
22. Ma, L.; Lee, S.; DeMuth, J.; Maldonado, S., Direct electrochemical deposition of crystalline silicon nanowires at T ≥ 60 °C. *RSC Advances* **2016,** *6* (82), 78818-78825.
23. Mahenderkar, N. K.; Liu, Y.-C.; Koza, J. A.; Switzer, J. A., Electrodeposited Germanium Nanowires. *ACS Nano* **2014,** *8* (9), 9524-9530.
24. Pavlikov, A. V.; Forsh, P. A.; Kashkarov, P. K.; Gavrilov, S. A.; Dronov, A. A.; Gavrilin, I. M.; Volkov, R. L.; Borgardt, N. I.; Bokova-Sirosh, S. N.; Obraztsova, E. D., Investigation of the Stokes to anti-Stokes ratio for germanium nanowires obtained by electrochemical deposition. *Journal of Raman Spectroscopy* **2020,** *51* (4), 596-601.
25. Yu, Z.; Yuan, L.; Wang, D.; Yuan, M.; Hu, Z.; Li, H.; Meng, X., Size tunable Ga–Ge nanowires for Li-ion battery prepared by in situ alloying in ionic liquid electrodeposition. *Applied Surface Science* **2020,** *508*, 144852.
26. Zein El Abedin, S.; Endres, F., Electrodeposition of Metals and Semiconductors in Air- and Water-Stable Ionic Liquids. *ChemPhysChem* **2006,** *7* (1), 58-61.
27. De Mattei, R. C.; Elwell, D.; Feigelson, R. S., The synthesis of GaAs by molten salt electrolysis. *Journal of Crystal Growth* **1978,** *43* (5), 643-644.
28. Oishi, T.; Watanabe, M.; Koyama, K.; Tanaka, M.; Saegusa, K., Process for Solar Grade Silicon Production by Molten Salt Electrolysis Using Aluminum-Silicon Liquid Alloy. *Journal of The Electrochemical Society* **2011,** *158* (9), E93.
29. Rao, G. M.; Elwell, D.; Feigelson, R. S., Electrowinning of Silicon from K 2SiF6 - Molten Fluoride Systems. *Journal of The Electrochemical Society* **1980,** *127* (9), 1940-1944.
30. Wacaser, B. A.; Dick, K. A.; Johansson, J.; Borgström, M. T.; Deppert, K.; Samuelson, L., Preferential Interface Nucleation: An Expansion of the VLS Growth Mechanism for Nanowires. *Advanced Materials* **2009,** *21* (2), 153-165.
31. Wan, H.; Ruda, H. E., A study of the growth mechanism of CVD-grown ZnO nanowires. *Journal of Materials Science: Materials in Electronics* **2010,** *21* (10), 1014-1019.
32. Heitsch, A. T.; Fanfair, D. D.; Tuan, H.-Y.; Korgel, B. A., Solution−Liquid−Solid (SLS) Growth of Silicon Nanowires. *Journal of the American Chemical Society* **2008,** *130* (16), 5436-5437.
33. DeMuth, J.; Fahrenkrug, E.; Maldonado, S., Controlling Nucleation and Crystal Growth of Ge in a Liquid Metal Solvent. *Crystal Growth & Design* **2016,** *16* (12), 7130-7138.
34. De Yoreo, J. J.; Vekilov, P. G., Principles of Crystal Nucleation and Growth. *Reviews in Mineralogy and Geochemistry* **2003,** *54* (1), 57-93.
35. Givargizov, E. I., FUNDAMENTAL ASPECTS OF VLS GROWTH. In *Vapour Growth and Epitaxy*, Cullen, G. W.; Kaldis, E.; Parker, R. L.; Rooymans, C. J. M., Eds. Elsevier: 1975; pp 20-30.
36. Nichols, P. L.; Sun, M.; Ning, C.-Z., Influence of Supersaturation and Spontaneous Catalyst Formation on the Growth of PbS Wires: Toward a Unified Understanding of Growth Modes. *ACS Nano* **2011,** *5* (11), 8730-8738.
37. Acharya, S.; Ma, L.; Maldonado, S., Critical Factors in the Growth of Hyperdoped Germanium Microwires by Electrochemical Liquid–Liquid–Solid Method. *ACS Applied Nano Materials* **2018,** *1* (10), 5553-5561.
38. DeMuth, J.; Ma, L.; Lancaster, M.; Acharya, S.; Cheek, Q.; Maldonado, S., Eutectic-Bismuth Indium as a Growth Solvent for the Electrochemical Liquid-Liquid-Solid Deposition of Germanium Microwires and Coiled Nanowires. *Crystal Growth & Design* **2018,** *18* (2), 677-685.
39. Fahrenkrug, E.; Gu, J.; Maldonado, S., Electrodeposition of Crystalline GaAs on Liquid Gallium Electrodes in Aqueous Electrolytes. *Journal of the American Chemical Society* **2013,** *135* (1), 330-339.

40. Fahrenkrug, E.; Rafson, J.; Lancaster, M.; Maldonado, S., Concerted Electrodeposition and Alloying of Antimony on Indium Electrodes for Selective Formation of Crystalline Indium Antimonide. *Langmuir* **2017,** *33* (37), 9280-9287.
41. Jungjohann, K. L.; Evans, J. E.; Aguiar, J. A.; Arslan, I.; Browning, N. D., Atomic-Scale Imaging and Spectroscopy for In Situ Liquid Scanning Transmission Electron Microscopy. *Microscopy and Microanalysis* **2012,** *18* (3), 621-627.
42. de Jonge, N.; Ross, F. M., Electron microscopy of specimens in liquid. *Nature Nanotechnology* **2011,** *6* (11), 695-704.
43. Zeng, Z.; Liang, W.-I.; Liao, H.-G.; Xin, H. L.; Chu, Y.-H.; Zheng, H., Visualization of Electrode–Electrolyte Interfaces in LiPF6/EC/DEC Electrolyte for Lithium Ion Batteries via in Situ TEM. *Nano Letters* **2014,** *14* (4), 1745-1750.
44. *Liquid Cell Electron Microscopy*. Cambridge University Press: Cambridge, 2016.
45. Han, C.; Islam, M. T.; Ni, C., In Situ TEM of Electrochemical Incidents: Effects of Biasing and Electron Beam on Electrochemistry. *ACS Omega* **2021,** *6* (10), 6537-6546.
46. Zeng, Z.; Zheng, W.; Zheng, H., Visualization of Colloidal Nanocrystal Formation and Electrode–Electrolyte Interfaces in Liquids Using TEM. *Accounts of Chemical Research* **2017,** *50* (8), 1808-1817.
47. Liao, H.-G.; Zheng, H., Liquid Cell Transmission Electron Microscopy. *Annual Review of Physical Chemistry* **2016,** *67* (1), 719-747.
48. Liao, H.-G.; Zherebetskyy, D.; Xin, H.; Czarnik, C.; Ercius, P.; Elmlund, H.; Pan, M.; Wang, L.-W.; Zheng, H., Facet development during platinum nanocube growth. *Science* **2014,** *345* (6199), 916.
49. Zheng, L.; Zhao, L.; Zhao, S.; Zhang, X.; Bustillo, K. C.; Yao, Y.; Yi, X.; Zhu, M.; Li, W.; Zheng, H., A unique pathway of PtNi nanoparticle formation observed with liquid cell transmission electron microscopy. *Nanoscale* **2020,** *12* (3), 1414-1418.
50. Kelly, D. J.; Zhou, M.; Clark, N.; Hamer, M. J.; Lewis, E. A.; Rakowski, A. M.; Haigh, S. J.; Gorbachev, R. V., Nanometer Resolution Elemental Mapping in Graphene-Based TEM Liquid Cells. *Nano Letters* **2018,** *18* (2), 1168-1174.
51. Park, J.; Park, H.; Ercius, P.; Pegoraro, A. F.; Xu, C.; Kim, J. W.; Han, S. H.; Weitz, D. A., Direct Observation of Wet Biological Samples by Graphene Liquid Cell Transmission Electron Microscopy. *Nano Letters* **2015,** *15* (7), 4737-4744.
52. Wu, F.; Yao, N., Advances in sealed liquid cells for in-situ TEM electrochemial investigation of lithium-ion battery. *Nano Energy* **2015,** *11*, 196-210.
53. Ambrožič, B.; Prašnikar, A.; Hodnik, N.; Kostevšek, N.; Likozar, B.; Rožman, K. Ž.; Šturm, S., Controlling the radical-induced redox chemistry inside a liquid-cell TEM. *Chemical Science* **2019,** *10* (38), 8735-8743.
54. Schneider, N. M.; Norton, M. M.; Mendel, B. J.; Grogan, J. M.; Ross, F. M.; Bau, H. H., Electron–Water Interactions and Implications for Liquid Cell Electron Microscopy. *The Journal of Physical Chemistry C* **2014,** *118* (38), 22373-22382.
55. Noh, K. W.; Liu, Y.; Sun, L.; Dillon, S. J., Challenges associated with in-situ TEM in environmental systems: The case of silver in aqueous solutions. *Ultramicroscopy* **2012,** *116*, 34-38.
56. Park, J. H.; Schneider, N. M.; Grogan, J. M.; Reuter, M. C.; Bau, H. H.; Kodambaka, S.; Ross, F. M., Control of Electron Beam-Induced Au Nanocrystal Growth Kinetics through Solution Chemistry. *Nano Letters* **2015,** *15* (8), 5314-5320.
57. Rojas, J. V.; Castano, C. H., Radiolytic synthesis of iridium nanoparticles onto carbon nanotubes. *Journal of Nanoparticle Research* **2014,** *16* (8), 2567.
58. Grogan, J. M.; Schneider, N. M.; Ross, F. M.; Bau, H. H., Bubble and Pattern Formation in Liquid Induced by an Electron Beam. *Nano Letters* **2014,** *14* (1), 359-364.
59. Schneider, N. M., Electron Beam Effects in Liquid Cell TEM and STEM. In *Liquid Cell Electron Microscopy*, Ross, F. M., Ed. Cambridge University Press: Cambridge, 2016; pp 140-163.
60. Woehl, T. J.; Abellan, P., Defining the radiation chemistry during liquid cell electron microscopy to enable visualization of nanomaterial growth and degradation dynamics. *Journal of Microscopy* **2017,** *265* (2), 135-147.

61. Jensen, E.; Mølhave, K., Encapsulated Liquid Cells for Transmission Electron Microscopy. In *Liquid Cell Electron Microscopy*, Ross, F. M., Ed. Cambridge University Press: Cambridge, 2016; pp 35-55.
62. Klein, K. L.; Anderson, I. M.; De Jonge, N., Transmission electron microscopy with a liquid flow cell. *Journal of Microscopy* **2011,** *242* (2), 117-123.
63. Regan, M. J.; Kawamoto, E. H.; Lee, S.; Pershan, P. S.; Maskil, N.; Deutsch, M.; Magnussen, O. M.; Ocko, B. M.; Berman, L. E., Surface Layering in Liquid Gallium: An X-Ray Reflectivity Study. *Physical Review Letters* **1995,** *75* (13), 2498-2501.
64. Tostmann, H.; DiMasi, E.; Pershan, P. S.; Ocko, B. M.; Shpyrko, O. G.; Deutsch, M., Surface structure of liquid metals and the effect of capillary waves: X-ray studies on liquid indium. *Physical Review B* **1999,** *59* (2), 783-791.
65. Festersen, S.; Hrkac, S. B.; Koops, C. T.; Runge, B.; Dane, T.; Murphy, B. M.; Magnussen, O. M., X-ray reflectivity from curved liquid interfaces. *Journal of Synchrotron Radiation* **2018,** *25* (2), 432-438.
66. Magnussen, O. M.; Ocko, B. M.; Regan, M. J.; Penanen, K.; Pershan, P. S.; Deutsch, M., X-Ray Reflectivity Measurements of Surface Layering in Liquid Mercury. *Physical Review Letters* **1995,** *74* (22), 4444-4447.
67. Duval, J. F. L.; Bera, S.; Michot, L. J.; Daillant, J.; Belloni, L.; Konovalov, O.; Pontoni, D., X-Ray Reflectivity at Polarized Liquid-Hg--Aqueous-Electrolyte Interface: Challenging Macroscopic Approaches for Ion-Specificity Issues. *Physical Review Letters* **2012,** *108* (20), 206102.
68. Elsen, A.; Festersen, S.; Runge, B.; Koops, C. T.; Ocko, B. M.; Deutsch, M.; Seeck, O. H.; Murphy, B. M.; Magnussen, O. M., In situ X-ray studies of adlayer-induced crystal nucleation at the liquid–liquid interface. *Proceedings of the National Academy of Sciences* **2013,** *110* (17), 6663.
69. Elsen, A.; Murphy, B. M.; Ocko, B. M.; Tamam, L.; Deutsch, M.; Kuzmenko, I.; Magnussen, O. M., Surface Layering at the Mercury-Electrolyte Interface. *Physical Review Letters* **2010,** *104* (10), 105501.
70. Runge, B.; Festersen, S.; Koops, C. T.; Elsen, A.; Deutsch, M.; Ocko, B. M.; Seeck, O. H.; Murphy, B. M.; Magnussen, O. M., Temperature- and potential-dependent structure of the mercury-electrolyte interface. *Physical Review B* **2016,** *93* (16), 165408.
71. Calderín, L.; González, L. E.; González, D. J., Ab initio molecular dynamics study of the free surface of liquid Hg. *Physical Review B* **2013,** *87* (1), 014201.
72. D'Evelyn, M. P.; Rice, S. A., A study of the liquid–vapor interface of mercury: Computer simulation results. *The Journal of Chemical Physics* **1983,** *78* (8), 5081-5095.

CHAPTER 2

In-Situ Transmission Electron Microscopy (TEM) Measurements of Ge Nanowire Synthesis with Liquid Metal Nanodroplets in Water

Adapted with permission from Cheek, Q.*; Fahrenkrug, E.;* Hlynchuk, S.; Alsem, D. H.; Salmon, N. J.; and Maldonado, S. "In-Situ Transmission Electron Microscopy (TEM) Measurements of Ge Nanowire Synthesis with Liquid Metal Nanodroplets in Water" ACS Nano, 2020, 14(3), 2869-2879. Copyright 2021 American Chemical Society.

2.1 Introduction

Group IV semiconductor nanowires are attractive materials for current and emerging energy conversion, sensing, and electronic applications.[1-5] Irrespective of the target technology, the crystallographic and compositional attributes of Ge and Si nanowires are critical to their function and are determined during synthesis. Accordingly, a detailed understanding of the synthetic methods used to grow group IV semiconductor nanowires is key to realizing desired functionality.

One nascent and potentially enabling synthesis method for crystalline Ge and Si nanowires is the electrochemical liquid-liquid-solid (ec-LLS) process.[6-8] In effect, this technique marries conventional electrodeposition with melt crystal growth by replacing the solid electrode with a liquid metal electrode. The crux of this technique is that the liquid metal serves as both a source of electrons and as a growth solvent for inorganic crystals, with the advantage that it can be performed at lower growth temperatures (T < 100 °C) and ambient atmosphere.[9] Colloquially, ec-LLS is generally akin to performing vapor-liquid-solid (VLS)[10] nanowire growth in a beaker and using electrochemistry rather than heat to drive the process (Scheme 2.1). To date, understanding of the ec-LLS process has come by way of indirect studies, *e.g.* exhaustive analyses of as-grown materials[5, 11-13] or an indirect, ensemble spectroscopic measure of growth during an ec-LLS process.[14] Detailed and direct insight on ec-LLS processes is presently lacking.

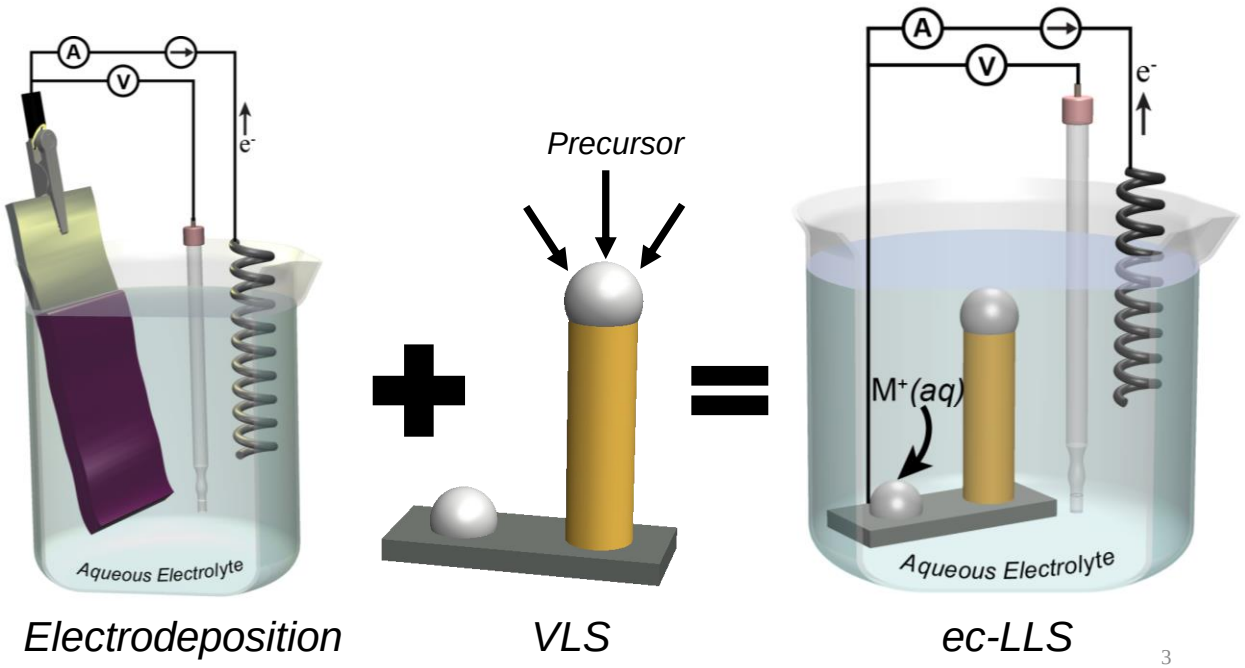

Scheme 2.1. Thematic and simplified description of the growth of crystalline semiconductor nanowires by the electrochemical liquid-liquid-solid (ec-LLS) strategy, which combines the set-up and simplicity of conventional electrodeposition with the crystal growth metallurgy of vapor-liquid-solid (VLS) nanowire growth but without high temperatures or gaseous reactants. Notably, this depiction does not imply any specific mechanistic information regarding ec-LLS or VLS.

Recent advancements in analytical transmission electron microscopy (TEM) afford the possibility of studying nanomaterial growth processes with high fidelity. Specifically, with liquid TEM holders and fast-frame-rate digital detectors, it is possible to directly visualize discrete nucleation and nascent crystal growth events in solution with high spatial and temporal resolution.[15-21] In principle, an *in-situ* TEM study of ec-LLS only requires housing a liquid metal volume(s) on a current collector within the viewing window of the liquid holder and then applying a potential/current to the liquid metal through the current collector. The metallurgical reactions between liquid metals and the majority of solid metal electrode materials substantially complicate this experimental design. However, in the course of performing such experiments, our lab observed a potentially simplifying phenomenon. Under certain experimental conditions, unsupported liquid metal nanodroplets could facilitate reduction of dissolved GeO_2 and subsequent crystalline Ge nanowire growth simply by irradiation of the electron beam of the TEM (Scheme 2.2). This observation suggests that it may be possible to study ec-LLS events simply, *i.e.* without a physical electrical contact or the use of an external current/potential source (*e.g.* a potentiostat). In the context of ec-LLS growths of semiconductor nanowires, such measurements could prove valuable to answer several outstanding questions including: (*1*) is the growth rate of nanowires limited by chemical or electrochemical factors, (*2*) what are conditions necessary for nucleation and crystal growth, and (*3*) can the presence of crystallographic defects be minimized?

Herein, this report describes the phenomenon of unsupported liquid metal nanodroplets supporting covalent semiconductor nanowire growth in solution when irradiated by an electron beam. This study explores its utility as a streamlined approach for microscopic studies of semiconductor nanowire growth mediated by liquid metals. Specifically, liquid metal Ga and In nanodroplets are described here as potential platforms to initiate and study Ge nanowire ec-LLS in aqueous solution by the electrochemical reduction of dissolved GeO_2. At this pH, the overall redox process can be described as '$HGeO_3^- + 2H_2O + 4e^- \rightarrow Ge + 5OH^-$' since $HGeO_3^-$ is the primary form of dissolved GeO_2.[22] Ga and In are important liquid metals because they are common constituents in most low-melting point metal alloys.[23-24] To date, these metals have been used extensively in ec-LLS studies since they afford the possibility of low temperature semiconductor nanowire syntheses.[12, 25] This study tests three related hypotheses regarding these liquid metals. First, the use of the electron beam in liquid TEM experiments to induce nanowire growths specifically in the presence of liquid metals is general. Second, the nanowire growth rates are

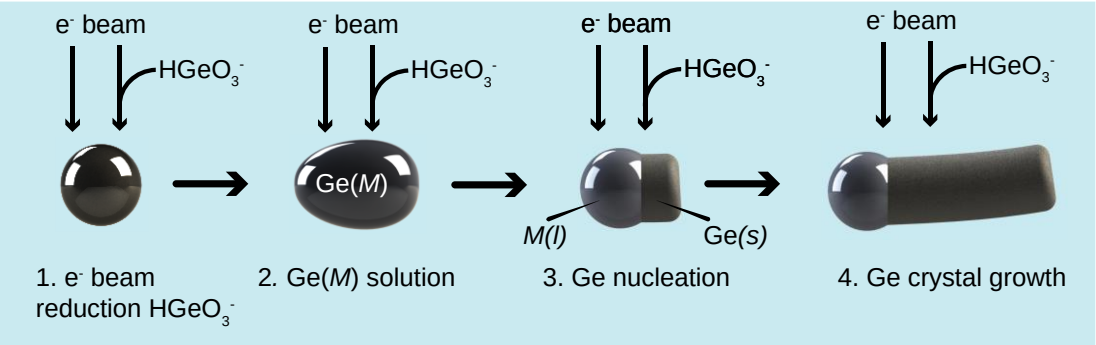

Scheme 2.2. Schematic depiction of (*1*) an e^- beam causing the reduction of dissolved GeO_2 in solution to Ge^0 followed by (*2*) dissolution into a liquid metal nanodroplet, then (*3*) crystal nucleation, and finally (*4*) Ge nanowire growth.

sensitive to the supply of electrons and affect the occurrence of crystallographic defects. Third, these nanowire growths occur under conditions far from equilibrium and have consequences on the resultant crystallinity. A series of micrographs and observations from *in-situ* videos are presented below.

2.2 Experimental

Materials Germanium(IV) oxide (99.999%, Alfa Aesar), indium (III) bromide (99.99%, Acros Organics), indium (III) chloride (99.99%, Acros Organics), gallium (III) nitrate (99.9998%, Acros Organics), disodium citrate hydrate (>99%, Fischer Scientific), potassium nitrate (99+%, Acros Organics), gallium tris(dimethylamide) dimer ($Ga_2(NMe_2)_6$ (99.9 % ampouled under argon, Alfa Aesar), sodium borohydride (98%, Spectrum), di-*n*-octylamine (≥ 97.0%, Sigma-Aldrich), 1-octadecene (≥ 95.0%, Sigma-Aldrich), sodium tetraborate (>99.5% Sigma-Aldrich), and oleic acid (90% technical grade, Sigma-Aldrich) were used as received. ($Ga_2(NMe_2)_6$ was stored in the glovebox prior to use. $InCl_3$, $InBr_3$, and $Ga(NO_3)_3$ were stored in a desiccator prior to use. Water with a resistivity >18.2 MΩ·cm (Nanopure Barnstead Water Purification) was used throughout.

Electron Microscope All TEM experiments were performed in a JEOL 2010F field emission analytical microscope operated at an acceleration voltage of 200 kV in parallel beam (TEM) mode. Images were collected without insertion of condenser or intermediate lens apertures. However, an objective aperture was used to enhance contrast during imaging. Still images and videos were collected with either a Gatan 794 Multiscan camera at 3 frames per second with a pixel resolution of 1024 x 1024 or a Gatan *One View* camera at 4k (25 frames per second) or at 2k (100 frames per second) pixel resolution.

Liquid Cell TEM Apparatus Experiments were conducted with a commercial liquid TEM sample holder and microfabricated Si chips from Hummingbird Scientific (Lacey, WA). The general configuration relies on a thin nanofluidic channel formed by compressing and sealing two microfabricated Si chip sets (~50 nm SiN_x window, spacer thickness of 250 nm, cell volume = 7.69×10^{-6} cm^3, window area = 1.95×10^{-4} cm^2) into the tip of a custom TEM sample holder. Prior to use, each Si chip sets were plasma etched with Ar(g) for 2 min to clean and render hydrophilic interfaces. Following assembly of the liquid cell, the holder was inserted into a secondary evacuated cell held at 8×10^{-6} torr for 15 minutes to ensure mechanical stability of the liquid cell prior to insertion into the TEM. Prior to each experiment, solution was flowed into the chipset

through plastic tubing *via* a programmable syringe pump at a constant flow rate. During imaging, this flow rate was held constant at 5 μL min^{-1}. Following each experiment, the lines to the liquid TEM cell were rinsed with pure H_2O at a rate of 15 μL min^{-1} for 20 min to avoid cross contamination between experiments.

Ex-Situ Gallium Nanodroplet Synthesis Gallium nanodroplets that were prepared outside of the TEM were synthesized by a hot injection method from dried reagents using a synthetic procedure under an inert atmosphere previously reported for synthesis of ~60 nm particles.[26] Briefly, 1-octadecene (7 mL) was added to a three neck round bottom flask equipped with a condenser, and then stirred magnetically under argon. The solution was heated to 280 °C. A solution of 25 mg gallium tris(dimethylamide) in di-*n*-octylamine (3.39 mL) and 1-octadecene (2.61 mL) was injected into the hot reaction flask. The solution color changed from yellow to dark grey within 60 s. The reaction flask was removed from the heating mantle and cooled to room temperature with a computer fan and an ice bath. Chloroform (10mL), oleic acid (1 mL), and ethanol (20 mL) where added to clean the contents of the round bottom flask. Centrifugation was performed at 6000 rpm for 10 min and then repeated a total of three times for Ga nanoparticle isolation. For storage purposes, the nanoparticles were dispersed in an ethanol solution. For dry TEM imaging, the colloidal solution was drop-cast directly on a TEM grid. For liquid cell experiments, a solvent exchange process was carried out. First, 5 mL of the ethanol solution was centrifuged for 10 min at 6000 rpm. The ethanol was exchanged with water and re-suspended. This process was repeated twice. On the third time, an aqueous solution of 50 mM GeO_2 and 10 mM $Na_2B_4O_7$ was used to exchange the pure water.

Ex-Situ Indium Nanodroplet Synthesis Indium nanodroplets were prepared by a one-pot synthesis method that was previously reported for allowing for the synthesis of In spheres with a diameter ranging from 10-100 nm.[27] 15 mL diethylene glycol solvent was added to a three neck round bottom flask containing 1.6 mg $InCl_3$ and 2.1 mg disodium citrate hydrate. The flask was then purged with Ar(*g*) for 30 min followed by heating to 100 °C. 2.7 mg $NaBH_4$ was then dissolved in 1.0 mL water. After the solution remained at 100 °C for 10 min, the $NaBH_4$ solution was injected into the round bottom flask resulting in an immediate color change. These nanodroplets were then separated and prepared for analysis in the same manner described above.

In-situ Synthesis of Liquid Metal Nanodroplets Metal nanodroplets were also synthesized directly inside the liquid TEM holder cell through reduction of a dissolved metal salt by the imaging electron beam. Generally, these solutions contained 10 mM metal salt ($InBr_3$ or $Ga(NO_3)_3$) 10 mM disodium citrate hydrate, and 100 mM KNO_3 and were injected into the liquid cell at a rate of 5 μL min^{-1} for 5 min to flush the cell entirely with this solution. The holder was then inserted into the TEM for imaging. Under high intensity imaging condition, metal nuclei were routinely observed. In the absence any added citrate in solution, the metal nanodroplets were unstable after formation, regularly dissolving away after prolonged beam exposure.

In-situ Ge Nanowire ec-LLS A solution containing 50 mM GeO_2 and 10 mM sodium tetraborate was then injected at a rate of 5 μL min^{-1} for 15 min to flush three dead volumes. Even after flushing the cell for 15 min, a large number of liquid metal nanodroplets remained on or near the window of the cell. During these experiments, the condenser lens current was adjusted so that the beam size was approximately equal to the field of view in each movie, *i.e.* the center to the corner of the field of view was approximately equal to the radius of the beam. An objective aperture was used to enhance contrast and a selected-area aperture for diffraction, but otherwise no apertures were use

Data Analysis All image analysis was performed using FIJI (Ver 1.52p). Two methods were employed for tracking the growth rates of nanowires in these studies. If there was no sample drift present in the data frames, the length of the wire was tracked by placing a tick at the front of the liquid metal cap for each frame. Then, the position of each tick was measured in FIJI allowing for the distance between each tick to be calculated and summed to retrieve the length of the nanowire at each point in time. If significant drift was present, then the nanowires lengths were measured manually for each frame using the segmented line tool in FIJI. These nanowires lengths were then plotted vs time allowing for a growth rate to be determined from the slope of the line of best fit. The time zero points in most of the movies collected for data analysis represent the first instant after the position of the beam was set and the beam was unblanked to initiate imaging. However, in some occasions, the beam was unblanked, nanowire events were observed, and then the beam was re-positioned to better view additional events. Accordingly, in these movies the time stamps are referenced to an arbitrary start time. In order to determine the supersaturation of Ge in the liquid metal nanodroplets, the diameter of the nanodroplets were measured using the line tool

in FIJI at each point in time. Assuming each nanodroplet was a perfect sphere, the volume of the nanodroplet was calculated based on the diameter measurement at each point in time. Changes in volume were interpreted as changes in liquid metal composition by dissolution of Ge into the liquid metal.[28]

2.3 Results & Discussion

Liquid Character of Metal Nanoparticles The liquid TEM holder used in this work had no separate heating/temperature control. Accordingly, it was not clear *apriori* whether the metal particles studied here would be molten or solid. Two general observations were noted to ascertain liquid, rather than solid, character of the nanoparticles that are the focus of this work. If the metal particles coalesced rapidly, liquid character and/or if the particles yielded no definitive electron beam diffraction patterns, liquid metal character was inferred.

Bulk Ga has a relatively low melting point (T_m = 29.8 °C).[29] For Ga, fast coalescence of particles was routinely observed but only in solution (Figures 2.1a,b). In vacuum, Ga particles (both with ligands and those with a native oxide[26]) could be imaged in close proximity without any evidence of coalescence, even after focusing the electron beam to the highest possible density for prolonged periods. Presumably, the ligand and/or oxide shell prevented intermixing between two Ga droplets. In solution, Ga particles (even those on the micron scale) rapidly fused if they were being imaged while in close proximity with each other (Figure 2.1c). The short timescales of fusion provided compelling evidence of liquid character. The coalescence also implied that the local environment of the Ga droplets was strongly reducing, thereby removing/mitigating the native surface oxide. An alternative hypothesis for the fusion events could be that the electron beam generated vacancies/defects in the surface oxides *via* a knock-on displacement[30] from the incident electron beam (*i.e.* physical damage due to radiation exposure). Although this scenario could not be ruled out, the likelihood that this wouldn't occur in the dry state but would in the liquid environment seems low. Further, the reductive removal of the surface oxide is consistent with the further phenomenon reported below while a knock-on mechanism is not. Finally, irrespective of how the surface oxide is ultimately removed by the electron beam, the rapid fusion of the droplets appears consistent with molten rather than solid metal character.

Separately, the melting point of bulk In is well above room temperature (T_m = 156.6 ºC),[31] but T_m for In nanoparticles can be greatly suppressed. Values as low as T_m = 25 ºC have been documented for In nanoparticles with radii (r) = 20 nm.[32] In nanoparticles on this size scale (Figure 2.1d) consistently did not exhibit any electron diffraction patterns when probed by selected area electron diffraction measurements (Figure 2.1e). For reference In nanoparticles larger than this critical threshold regularly exhibited diffraction patterns consistent with solid, crystalline In in the liquid TEM holder. For In nanoparticles with $r \leq 20$ nm, rapid coalescence of separate volumes into one was routinely observed. Figure 2.1f summarizes one such event, occurring within approximately 3 s. Similar events were observed to proceed in as little as 0.2 s. For reference, coalescence of similarly-sized solid metal nanoparticles generally takes place over the course of tens of seconds.[33-35]

General Observations of Ge Nanowire Growth via Electrochemical Reduction of Dissolved GeO_2 by the Electron Beam Liquid metal nanodroplets facilitated nanowire growth when they were exposed to certain imaging conditions in a medium that contained dissolved GeO_2 (as a precursor for Ge) and sodium tetraborate (to set the pH, to increase the solubility of GeO_2 in water, and to mirror the electrolyte of conventional ec-LLS[6, 9, 11, 14]). Energy dispersive X-ray spectra obtained on the nanowires confirmed they were composed of Ge. When nanowire growth was observed, it generally occurred soon after first exposure to the electron beam. Just prior to the emergence of an obvious nanowire crystal, the apparent radius of the liquid nanodroplets increased (*vide supra*). During these experiments an objective aperture was used to enhance contrast and to allow for sufficient beam current to reduce oxidized Ge in solution.

Five parameters were noted as particularly influential regarding whether a nanowire growth event occurred. First, precipitation/ nucleation/crystal growth of Ge^0 did not occur in the absence of liquid metal nanodroplets. Prolonged imaging of solutions containing only dissolved GeO_2 and sodium tetraborate but without metal nanoparticles never yielded any spontaneous reduction of GeO_2. That is, the incident imaging beam was insufficient under any attainable imaging condition to drive zero-valent Ge formation. This point stands in contrast to simple metal salt reduction, which was both observed in this work and has been documented extensively by several labs.[17, 36-37] Second, the presence of surface ligands on the liquid metal nanodroplets was important. Liquid metal nanodroplets without any capping ligands were prone to rapid dissolution upon imaging

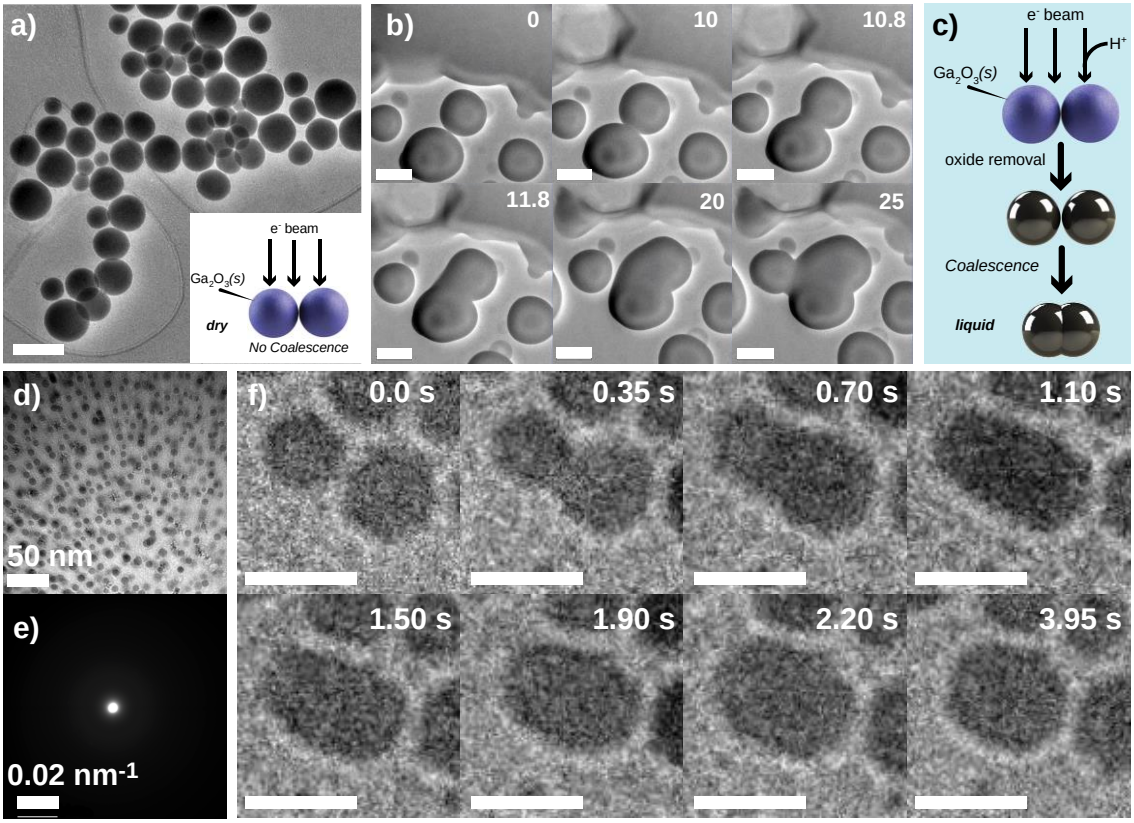

Figure 2.1. a) Transmission electron micrograph under "dry" conditions of Ga nanodroplets coated with a native oxide. Scale bar: 1 μm. Inset: Schematic illustration of how the native oxide of Ga droplets prevents coalescence. b) Frame grabs from an *in-situ* transmission electron microscopy video of Ga droplets immersed in an aqueous sodium tetraborate solution where the native oxide is unstable and coalescence occurs. Scale bar: 1 μm. c) Schematic depiction illustrating the removal of the native oxide on Ga nanodroplets under reducing conditions in solution. d) Transmission electron micrograph of liquid In nanoparticles with radii ≤ 10 nm. e) Selected area electron diffraction collected from the same In nanoparticles in (d). f) Frame grabs from an *in-situ* transmission electron microscopy video showing the coalescence between two In nanodroplets. Scale bar: 15 nm.

(*vide infra*). However, when an excess ligand concentration was used during synthesis of the liquid metal nanodroplet that saturated the surface adsorbed ligands, the liquid metal nanoparticles were indefinitely stable but never supported nanowire growth. Ge nanowires were only grown from liquid metal nanodroplets that possessed an intermediate ligand coverage. Third, we observed that Ge nanowire growth was not possible at all formal concentrations of dissolved GeO_2. For formal GeO_2 concentrations < 5 mM, no Ge nanowire growth events were ever observed. Prolonged imaging of liquid metal nanodroplets (> 60 s) in these solutions under any imaging condition only resulted in the nucleation of (presumably) an H_2(g) bubble. However, above this threshold formal concentration of dissolved GeO_2, Ge nanowire growth was routinely possible. The upper limit on the formal concentration of GeO_2 was limited to 100 mM, as GeO_2 precipitates and clogs the lines above this value, even if the bulk solutions were sufficiently metastable for conventional Ge ec-LLS on the benchtop. Fourth, a threshold for the electron beam current density was required to induce and drive nanowire growth at liquid metal nanodroplets. The electron beam density was adjusted in one of two ways. Either the absolute current of the electron beam was manually varied and/or the beam diameter was adjusted by controlling the condenser lens current. An approximate estimate of the threshold electron beam current density was 8 nA μm^{-2} **(**800 mA cm^{-2}). This current corresponded to a dose rate of ~ 4 x 10^9 Gy s^{-1}. Fifth, the areal density of liquid metal nanodroplets was strongly influential on whether ec-LLS was observed. Isolated ($\leq$ 1 per μm^{-2}) liquid metal nanodroplets never yielded Ge nanowires. Lastly, Ge nanowires were also observed in regions of the liquid TEM cell that were not directly imaged but were just proximal (within a few hundred nm) to irradiated areas.

Ge Nanowire Growth with Ga Nanodroplets Using the conditions amenable for electron-beam-induced nanowire growth, the growths of multiple Ge nanowires facilitated by Ga nanodroplets were observed. Figure 2.2a shows frames from a representative video showing the initial stages of a Ge nanowire growth from a Ga nanodroplet, with a corresponding plot of the volume change vs time (Figure 2.2b) that occurred prior to the emergence of a Ge nanowire. The estimated concentration of Ge in the Ga nanodroplet inferred from the volume change (assuming ideal behavior for the liquid Ga-Ge solution) for four different events was 63 ± 14 at.%. This value corresponds to a supersaturation of Ge in Ga reaching ~10^4, assuming the equilibrium solubility of Ge in Ga is 0.0045 at. % at T = 25 °C.[38] For reference, the individual supersaturation values in at.% from four Ge nanowire growths are superimposed on the Ge-Ga phase diagram[39] in Figure

2.2c. These data show that these ec-LLS Ge nanowire growths occurred at a temperature well below the thermodynamic melting temperature of the Ge-liquid metal mixture, as indicated on the phase diagram. Figure 2.2d shows four separate plots of Ge nanowire lengths vs time for four separate ec-LLS events measured in four separate cells, *i.e.* not at the same time. A monotonic trend was observed in all cases, indicating a steady-state nanowire growth. Using the slope of the best-fit line for each growth as the average growth rate, the observed growth rates ranged from 2.4 ± 0.1 to 18 ± 6 nm s^{-1}. Across these four measurements, it was not possible to directly ascribe the differences in growth rates solely to one variable, as differences in liquid solution thicknesses, electron beam stability, and type of detection camera varied between experiments performed on different imaging sessions. Nevertheless, these growth rates were consistent with a prior report of nanowire growth featuring solute trapping.[40] Based on the growth rates and diameters of these nanowires, the average faradaic current densities attained during these nanowire growths (assuming an overall $4e^-$ redox process and the nanodroplet operates as a hemispherical ultramicroelectrode) ranged from 3.4 ± 0.1 to 25.5 ± 0.9 mA cm^{-2}.

Ge Nanowire Growth with In Nanodroplets In nanodroplets proved similarly capable of sustaining Ge nanowire. Anecdotally, for the same experimental conditions, initiating and viewing nanowire nucleation and growth with In nanodroplets proved significantly more facile than with Ga nanodroplets. Figure 2.3a shows frames from a representative movie of nanowire growth occurring at several In nanodroplets within the field of view. The time stamps in this figure and all other frames are relative, as the area was irradiated by the electron beam momentarily while area was being selected for imaging. Figure 2.3b highlights the growth of a single Ge nanowire over less than 3 seconds. This movie encapsulates several relevant points. First, capturing cleanly the initial nucleation for each nanowire was not always possible. In this movie, the Ge nanowire had already grown as a partial coil, as is evident in the first frame. Second, the growth direction of individual nanowires often changed. Third, even at high magnification, the image resolution was limited by scattering from water, obscuring lattice fringes.

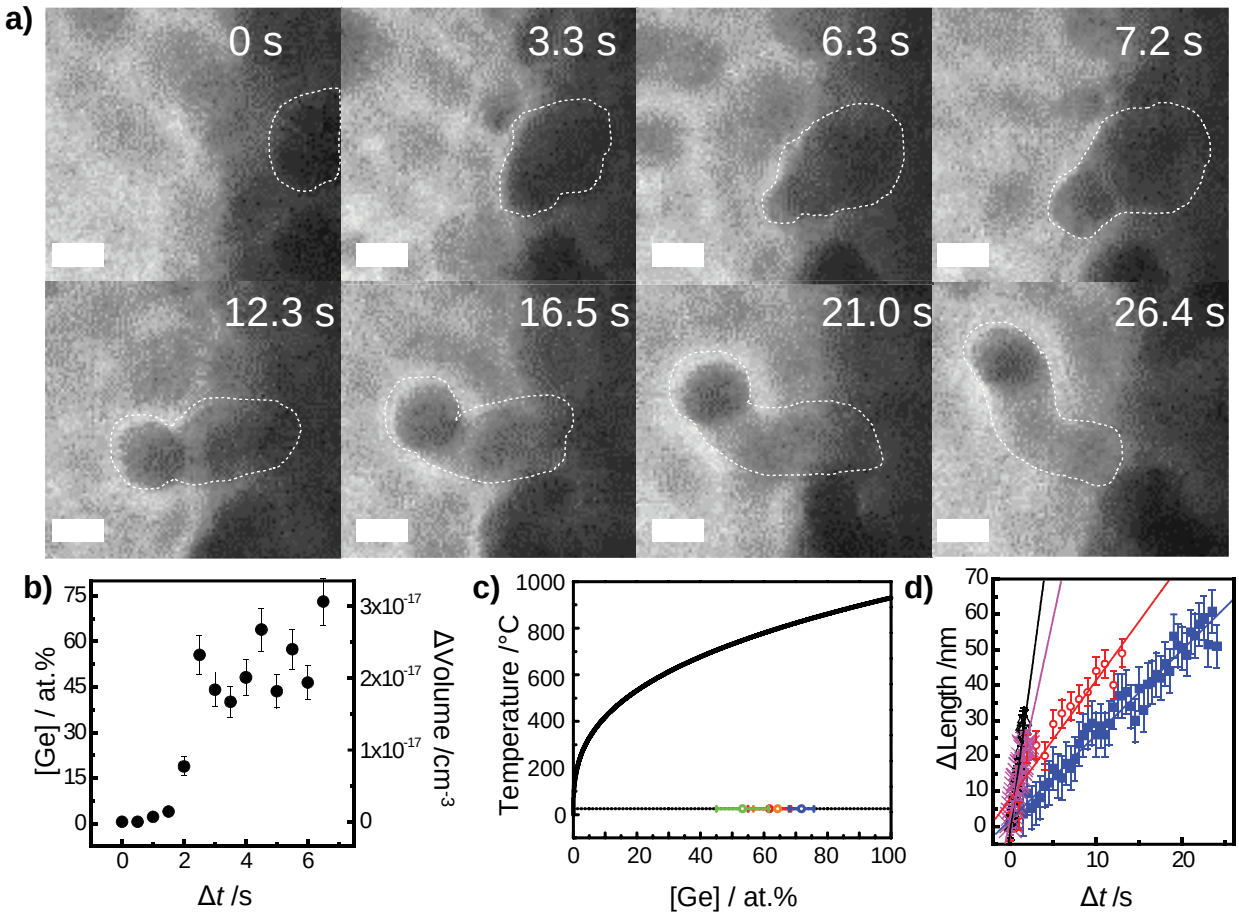

Figure 2.2. a) Frame grabs from an *in-situ* transmission electron microscopy video of a Ge ec-LLS event with a Ga nanodroplet immersed in an aqueous solution containing dissolved 0.05 M GeO_2. Scale bar: 50 nm b) A plot showing the volume change of the Ga nanodroplet as a function of time before Ge nucleation occurred. c) The phase diagram for the Ga-Ge system is shown with the inclusion of data from 4 different Ge nanowire growth events. The colored data points correspond to the inferred Ge concentration in the Ga nanodroplets at the time just before nucleation. d) A plot of Ge nanowire length vs time for four separate Ge nanowire growth events. The steady-state growth rates were estimated from the linear-least squares fitting of the data (red lines).

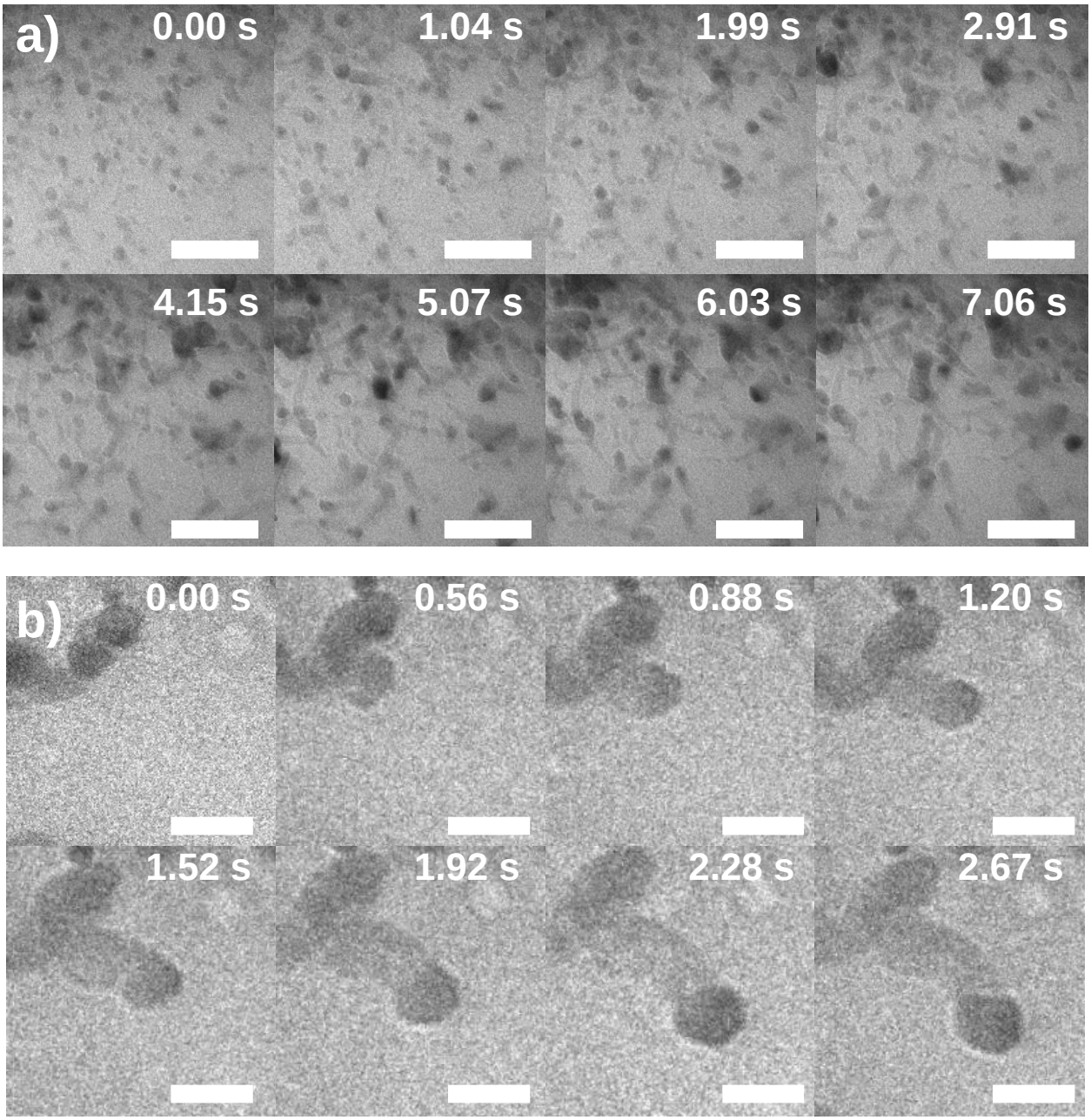

Figure 2.3. a) Frame grabs from an *in-situ* transmission electron microscopy video of parallel Ge nanowire growth events at In nanodroplets immersed in aqueous solution with a formal GeO_2 concentration of 0.05 M. Scale bar: 20 nm b) Frame grabs from an *in-situ* transmission electron microscopy video of a single Ge nanowire growth event in an aqueous solution with a formal GeO_2 concentration of 0.05 M. Scale bar: 75 nm.

Figure 2.4a highlights the short time period for a set of adjoining In nanodroplets prior to nucleation and growth of Ge nanowires. In these images, the volumes of the In nanodroplet increases quickly without obvious Ge nucleation. Due to the limited resolution of imaging in liquids and the crowding in these images, the unambiguous observation of volume swelling prior to the start of every Ge nanowire growth was not possible. Still, Figure 2.4b shows the relative volume changes over time up to the point of nucleation for 5 different nanowires. Assuming these volume changes corresponded to concentrations of Ge in the liquid metal nanodroplets at the time nucleation, these data implicated an average Ge concentration in liquid In of 80 ± 13 at.%. For reference, the equilibrium solubility of Ge in In is 0.00075 at. % at T = 25 °C.[38] However, the specific supersaturation value of Ge in In is ambiguous, as the Ge-In solubility value rigorously holds only for dissolved Ge in bulk, solid In. Still, these observations generally imply a similarly large, ~ 10^4 supersaturation of Ge in In.

Figure 2.5 shows representative Ge nanowire length vs time plots, again highlighting monotonic growths with respect to time. Since the propensity for Ge nanowire growth with In nanodroplets was high, it was possible to collect these data simultaneously, *i.e.* under the same imaging conditions. Accordingly, Figure 2.5b shows a plot of the observed growth rates as a function of the nanodroplet radius. A clear trend was observed, with the apparent growth rate decreasing as the nanodroplet radius increased. Based on the growth rates and radii of the nanodroplets, an average faradaic current density for these wire growths was estimated, ranging between 12 - 23 mA cm^{-2}. For reference, the mass-transport-limited current for hemispherical ultramicroelectrodes in this size range (= $2nFD[GeO_2]\pi^{-1}r^{-1}$; where n is the number of electrons involved, F is Faraday's constant, $[GeO_2]$ is the concentration of reducible dissolved GeO_2, and D is the diffusivity of redox species) in a quiescent solution would be >10,000 mA cm^{-2}.

Figure 2.6 highlights two additional interesting phenomena. First, the growth rate tracked directly with the electron beam intensity. Frames from a video of an experiment where the Ge nanowire growth process was modulated by adjusting the electron beam intensity are shown in Figure 2.6a. In these panels, the electron beam intensity was increased by a factor of 3.5 at t = 2.25 s by adjusting the condenser lens current to change the diameter of the electron beam while the nanowire growth was continuously imaged. The corresponding growth rate plot is shown in Figure 2.6b. When the electron beam intensity was increased, the apparent growth rate accelerated by a

factor of 6. Second, the number of changes in nanowire growth direction rose after the growth rate increased. To ascertain explicitly whether there was a correlation, a series of Ge nanowire growth events (N = 30) were analyzed in detail. Figure 2.6c shows that the propensity for growth direction changes (normalized by final nanowire length) generally tracked with faster nanowire growth rates. To be clear, only 'lateral' growth direction changes were observable by this mode of imaging. Nevertheless, although the correlation was not strictly monotonic, nanowires grown at faster rates generally were much less straight.

Global Interpretation of the Cumulative Data The data in this work supports several important points. First, the observation of a spontaneous reduction of dissolved GeO_2 at liquid metal nanodroplets in a liquid TEM cell is in fact an electrochemical process without an external supply source like a potentiostat. Accordingly, these events can properly be described as ec-LLS. Second, the conditions necessary for initiating ec-LLS at uncontacted liquid metal nanodroplets in a liquid TEM cell highlight necessary factors for Ge ec-LLS to occur. Third, the nanowire growth rates reported here are in line with previous reports and suggest that crystal growth is limited by the feed rate of Ge into the liquid metal rather than the rate of crystallization. Fourth, nanowire growth in ec-LLS occurs far from thermodynamic equilibrium, impacting nanowire morphology and crystallographic quality.

Stimulated ec-LLS by the Incident Electron Beam One possible interpretation of the observed Ge nanowire growths is that the phenomena were more akin to a chemical, solution-liquid-solid[41-42] process that was thermally driven by the electron beam rather than electrochemical in nature. This interpretation is negated in the following ways. First, the temperature change in aqueous solutions induced by the incident electron beam in liquid TEM experiments has been proven to be small,[36] on the order of ~4 °C. Ge nanowire growth is not possible just by heating (to much larger temperatures approaching the boiling point of water) in solutions containing dissolved GeO_2, supporting electrolyte, and liquid metals is well established.[5-6, 9, 12-13, 25] Second, any heating of the solution by the electron beam would not strongly depend either on the density of nanodroplets in solution or the concentration of dissolved GeO_2. However, both aspects were observed to definitively influence the propensity for nanowire growth.

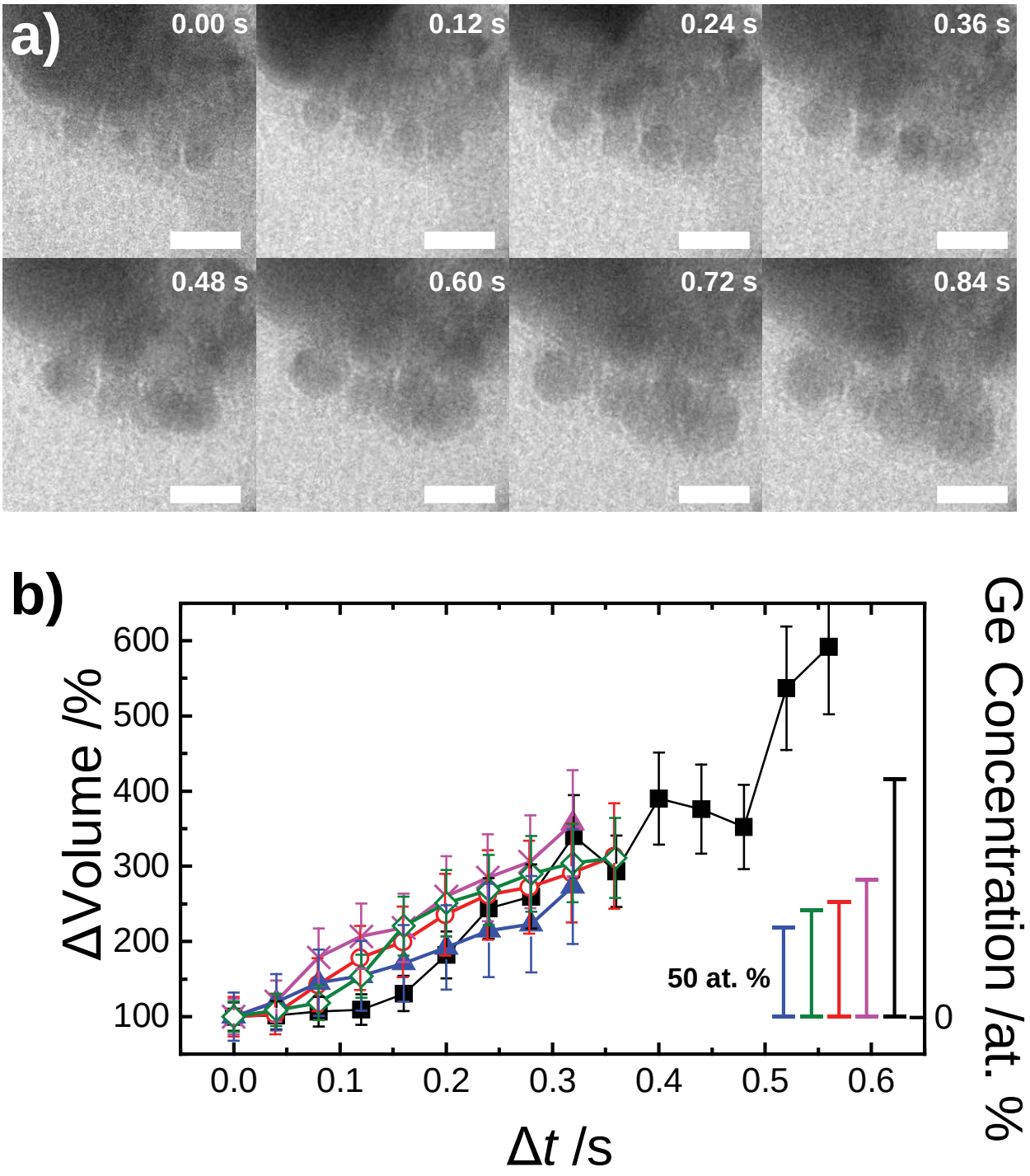

Figure 2.4. a) Frame grabs from an *in-situ* transmission electron microscopy video depicting the volume change demonstrated by four In nanodroplets due to the incorporation of Ge from the beam-induced reduction of dissolved GeO_2. Scale bar: 20 nm b) A plot illustrating the volume change in 5 separate In nanodroplets over the time prior to Ge nucleation. The right axes scale is different for each nanodroplet since the radius varied across this set of 5.

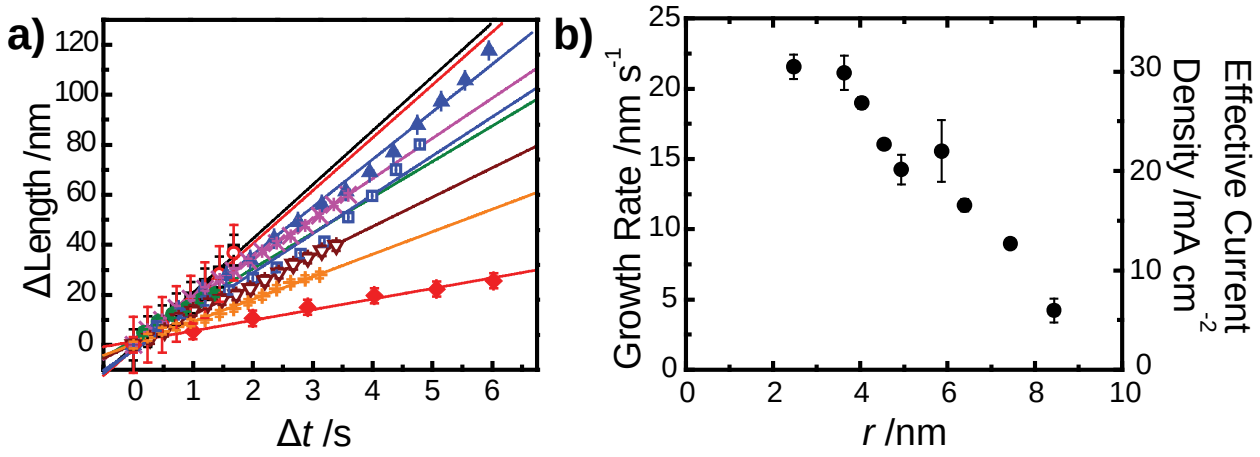

Figure 2.5. (a) A plot of Ge nanowire length vs time for 9 different Ge nanowire growth events at different In nanodroplets imaged under the same conditions. The steady-state growth rates were estimated from the linear-least squares fitting of the data (color-coated solid lines). b) A plot of the estimated nanowire growth rate in (a) as a function of the In nanodroplet radius.

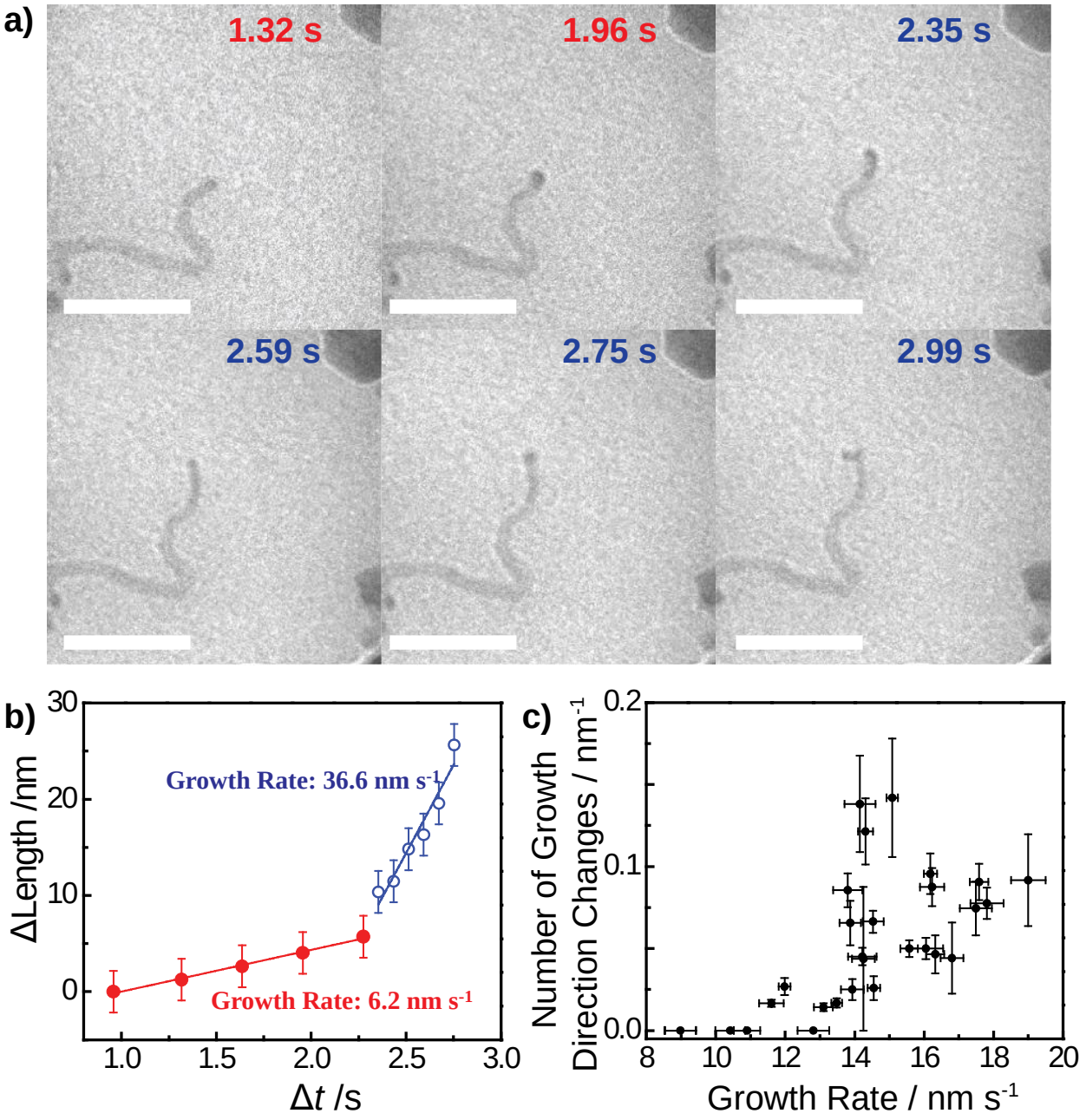

Figure 2.6. a) Frame grabs from an *in-situ* transmission electron microscopy video illustrating the growth of an individual Ge nanowire as a function of the electron beam intensity. The top three frames were recorded during a "broad" beam condition, while the bottom three frames were collected during a "focused" beam condition. Scale bar: 50 nm. b) A plot of the nanowire length vs time for the nanowire in (a). The red solid circles correspond to measurements under the "broad" beam condition. The open blue circles correspond to measurements under the "focused" beam condition. c) A plot of the number of observable growth direction changes for Ge nanowires as a function of the observed steady-state growth rate.

Although there are similarities to two separate types of phenomena, the data shown here are unlike anything ever reported in the *in-situ* liquid TEM literature. Certainly the precedent for the electron beam in liquid TEM experiments to induce electrochemical reduction of species dissolved in solution is well established.[37, 43-47] In fact, this premise was explicitly used here to generate liquid Ga and In nanodroplets directly in the liquid holder cell. However, this work makes clear that direct irradiation (*i.e.* imaging) of the GeO_2 solution is insufficient to nucleate any solids, implicating that it is not possible to generate stable Ge nuclei in water solely by radiolytic species or solvated electrons generated by the electron beam passing through water and the SiN windows. Rather, the presence of a liquid metal nanodroplet is a necessary criterion to locate and facilitate Ge nucleation and crystal growth. In this regard, the work presented here stands apart from electron-beam induced metal electrodeposition works[16, 37, 44] and instead has parallels to *in-situ* TEM semiconductor nanowire growths by the vapor-liquid-solid process.[48-50] The volume swelling of the liquid metal prior to observing nanowire growth further supports this interpretation, which is fully in line with the current understanding of nanowire growths catalyzed by liquid metal nandroplets.[25, 28, 51]

Questions remain exactly how the electron beam instigates the electrochemical reduction of dissolved GeO_2. One hypothesis is that the liquid metal nanodroplets are charged by the incident electron beam, effectively shifting their potential to more negative values where eventually the reduction of dissolved GeO_2 is thermodynamically spontaneous. This interpretation has two unresolvable complications. First, it implies that the principle of charge neutrality in solution is violated, as no corresponding oxidation reaction would be required. Second, it suggests that imaging any metal electrode by an incident electron beam would always shift unabated its potential to progressively large negative potentials. This scenario has not been observed previously. In fact, we previously noted any shifts of an electrode's potential induced by the electron beam were small, time-independent, and depended heavily on the specific experimental design.[52]

A second hypothesis is that the solvated electrons generated by the primary electrons of the incident electron beam are the reductants that react with dissolved GeO_2. This contention suggests that the density of available reductants (solvated electrons) would then be solely dependent on the intensity of the electron beam in the solution, implying the growth of Ge

nanowires would occur even at a single, isolated liquid metal nanodroplet. The observations presented above are counter to this premise.

A third hypothesis more in line with the cumulative observations is that the reductants are solvated electrons generated by *secondary electrons* scattered primarily from liquid metal nanodroplets. All materials irradiated by the electron beam (*i.e.* windows, solution, nanodroplets) release secondary electrons through scattering events with the primary beam.[46, 53] These secondary electrons have an extremely short range (~5-10 nm)[54-55] but are capable of generating solvated electrons that can reduce species in solution.[43, 45, 56] The inferred faradaic current for GeO_2 reduction is roughly 2.5% of the incident primary electron beam density, a value roughly in agreement for the steady-state yield of secondary electron processes.[56] A higher areal density of irradiated objects (*e.g.* cluster of liquid metal nanodroplets) would correspondingly lead to a higher steady-state concentration of solvated electrons from secondary electrons. Conversely, when irradiated objects are not concentrated or totally isolated, the amount of secondary electrons available to generate solvated electrons to drive reduction of GeO_2 would be correspondingly small. These aspects are in line with the observation that Ge nanowire growth events were much more probable with higher densities of liquid metal nanodroplets. Further, this hypothesis could also help explain (in part) why the probability of observing Ge nanowire growths was anecdotally higher with In rather than Ga nanodroplets. The coefficient for secondary electron emission, δ, is generally larger for elements with larger atomic number.[57] For Ga and In specifically, the δ value is ~35% greater for In than for Ga.[57] Based on these points, we posit that the Ge nanowire growths shown here were dictated largely or exclusively by solvated electrons generated from secondary electron scattering.

To be clear, the designation of 'ec-LLS' for the nanowire growth events shown here should not be confused with any colloquial meaning of the term 'electrochemistry.' By no means was an external power supply or potentiostat used to drive the reduction of dissolved GeO_2 that necessarily occurred here. Further, we do not discount the occurrence of radiolytic reactions in the solution, as are known to occur in liquid TEM experiments.[56] Rather, we simply feel the data are clear that the chemical phenomena involved in Ge nanowire formation are unambiguously induced by and tied to the electrostatic influence of the incident electron beam. Accordingly, the designation of these data as 'electrochemical' reflects this point. The connection to 'ec-LLS' is also clear since

the nanowire growths are necessarily dependent on the presence of liquid metal nanodroplets. Hence, we feel the results shown here provide significant insight on ec-LLS processes outside of the TEM.

Surface Condition of Liquid Metal Nanodroplets for Ge Nanowire Growth Three notable observations indicated the surface of the liquid metal nanodroplets is a more important factor than previously considered. The total absence of an observable volume change in the liquid metal nanodroplets in dilute (< 5 mM) solutions of dissolved GeO_2 implied the flux of Ge^0 into the liquid metal nanodroplets was effectively zero. This point suggests that the formal concentration in solution did not directly relate to the rate of reduction (as would be expected for the reduction of a diffusion limited species in solution). Prior electrochemical studies of Ge ec-LLS on Hg microdroplets support a complicated mechanism for the reduction of GeO_2 where adsorbed species may be involved.[58] If a rate-determining intermediate is surface-bound and at too low of a surface coverage to result in the formation and dissolution of Ge^0 into the liquid metal, then Ge nanowire growth will not occur. The role of at least one surface-bound species in the electrochemical process is further in line with separate observation that Ge nanowire growth was never observed when the liquid metals were exposed to saturating levels of citrate ligands. Previous studies on ec-LLS presumed the surface of the liquid metal just needed to be oxide-free to crystal growth.[12, 25]

A third, separate observation that speaks to the role of surface conditions is the decrease of the growth rate as the nanodroplet radius increases. The general characteristic for VLS-based nano/microwire growths is that nanowire growth rates typically *increase* with *increasing* metal droplet radii up to a saturating growth rate for the specific reaction conditions.[59] An inverse correlation where nanowires grow *slower* at larger nanodroplet sizes has been observed experimentally[60-61] and predicted theoretically[62-65] but generally only applies under certain conditions. Specifically, when the incorporation of solute (Ge) into the volume of the\ liquid metal is slow enough that another process (*e.g.* surface diffusion) can augment the delivery of solute to the liquid metal/solid crystallite interface, then an inverse growth rate-radius correlation will be operative. For VLS growths in molecular beam epitaxy systems, adatom diffusion from the substrate and nanowire side to the crystal growth front at the liquid metal/nanowire interface.[66] In the results presented here, neither of these possibilities is viable since Ge is electrocatalytically inactive for GeO_2 reduction. Instead, we argue the possibility that an adlayer of Ge^0 remains at the

liquid metal/liquid electrolyte interface that could diffuse on the surface of the liquid metal nanodroplet without having to dissolve within the bulk liquid metal volume. If these species reach the liquid metal/nanowire interface, they ought to be able to participate in crystallization. Scheme 2.3 summarizes this point.

Crystal Growth Rates in Ge Nanowire ec-LLS In principle, the electron beam intensity afforded the possibility of controlling nanowire growths in the same manner that an applied current does in a traditional electrodeposition experiment. The requirements for imaging and the propensity for generating H_2 bubbles set the lower and upper bounds on the usable electron beam intensity. Still, over the limited available range, the fact that the constant growth rates could be modulated directly by the electron beam intensity at effective current densities well below the mass transport limit indicates that the rate of nanowire growth was likely kinetically-limited by the electrochemical reduction reactions of dissolved GeO_2. If the kinetics of electroreduction were sufficiently fast that mass-transport of dissolved GeO_2 by radial diffusion to the liquid metal interface was instead controlling, the nanowire growth rates would have been much faster, insensitive to the electron beam intensity, and instead directly dependent on the concentration of dissolved GeO_2. Those aspects were not observed here. Ge nanowire growth rates limited by the kinetics of the electroreduction reaction also necessarily mean that the rate of crystallization inside the liquid metal nanodroplets was faster. Accordingly, the crystal growth rates for the events detailed here must be $> 10^{-8}$ m s^{-1}.

The reason why Ge crystallization rates can be large in ec-LLS with Ga & In is not immediately clear but the data point to one likely possibility. For both Ga and In, ec-LLS occurred under extremely high supersaturations of Ge in the liquid metals on the order of 10^4, representing extremely large driving forces for crystallization. For reference, typical supersaturation values in VLS range from $10^0 – 10^1$.[67] It should be noted that one aspect which as not considered was the influence on Ostwald ripening on metal nanodroplet volume change. If ripening did occur, then the measured supersaturation values would be lower than those reported here as the volume change would not solely be due to the dissolution of Ge^0 into the bulk. Nevertheless, this work is in agreement with previous *ex-situ* studies performed by our group which reported exceedingly high supersaturation values of 10^2 higher than the equilibrium concentration.[14] in that work the supersaturation values were more than an order of magnitude lower.

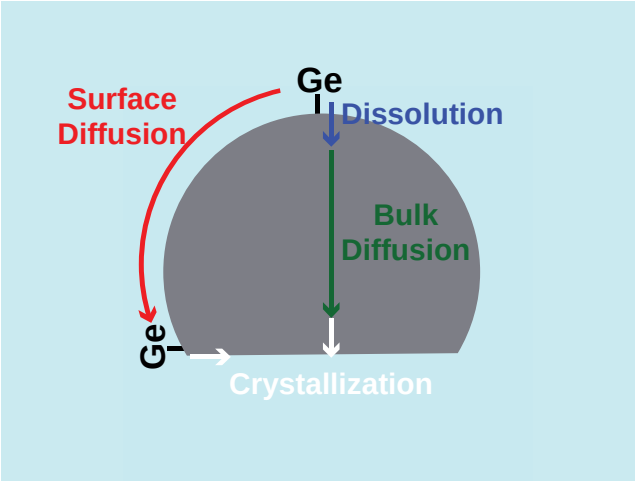

Scheme 2.3. Schematic depiction of Ge^0 transport both through the liquid metal bulk (as solute) and across the surface (as adsorbate) to the crystal growth front.

The reason why such large Ge supersaturations were attained is less obvious, as it implies that a sizeable activation barrier for nucleation exists in these systems. A similar inference of a large activation for Ge nucleation in Ga was noted previously in Ge microwire ec-LLS,[14] although it is not clear whether the difference arises from the sensitivities of the employed methods, the lack of an underlying solid substrate as compared to the traditional electrochemical experiments, or from the difference in liquid metal sizes. Nevertheless, the fact that large supersaturation values were observed in two distinct liquid metals suggest this activation barrier may be a general feature of low-temperature Ge crystal growth. Future studies with other liquid metal nanodroplets (*e.g.* Hg, In-Bi) would be informative on this point.

A consequence of fast crystal growth rates is the greater likelihood of crystallographic imperfections.[68] The data here support this point. It is not clear what specific crystallographic defect type(s) were responsible for the growth direction changes (*e.g.* substitutional defects like liquid metal inclusions & lattice-substitutions or twin dislocations). Nevertheless, the data strongly suggest that one pathway to straighter nanowires with fewer crystallographic defects is to slow down the nanowire growth. In principle, this can be achieved by adjusting applied potentials/ currents (in conventional ec-LLS) or the flux of irradiation (as shown here) but not necessarily by lowering the concentration of GeO_2 in the electrolyte.

2.4 Conclusion

The work presented here introduces and outlines a *via*ble methodology for studying crystalline nanomaterial growth by ec-LLS. This approach affords insight on the elementary processes involved in this hybrid electrochemical/metallurgical materials synthetic method. Doing so has highlighted that ec-LLS occurs under conditions where the rate of heterogeneous reduction of dissolved GeO_2 limits nanowire growth rather than the rate of crystallization. The measured supersaturations are surprisingly large, indicating a high activation barrier for nucleation that seems to be similar for two dissimilar liquid metals. Additionally, the data shown here suggest further studies to characterize the nature of the liquid metal/electrolyte interface in more detail are warranted. In a larger sense, these data also suggest it might be possible to perform similar 'wireless' ec-LLS nanowire growths by a bulk radiolysis technique that also generates solvated electrons.[69-70] In this way, it may be possible to further extend ec-LLS towards conditions that more closely mirror solution-liquid-solid (SLS) nanowire syntheses[42] but with simpler, oxidized

reagents that can be reduced electrochemically. Additionally, the prevalence of surface- rather than bulk-diffusion processes as controlling the observed nanowire growth suggests the possibility of using larger solid particles. That is, if electrochemical crystalline Ge growth can be supported via the diffusion of surface adatoms (i.e, little to no diffusion through the bulk is required), it may be possible for solid metal caps to support a new electrochemical liquid Solid Solid (ec-LSS) process. This idea is discussed further in chapter 5 of this thesis.

2.5 References

1. Chan, C. K.; Peng, H.; Liu, G.; McIlwrath, K.; Zhang, X. F.; Huggins, R. A.; Cui, Y., High-performance lithium battery anodes using silicon nanowires. *Nat. Nanotechnol.* **2007,** *3*, 31.
2. Garnett, E.; Yang, P., Light Trapping in Silicon Nanowire Solar Cells. *Nano Lett.* **2010,** *10* (3), 1082-1087.
3. Wang, D.; Chang, Y.-L.; Wang, Q.; Cao, J.; Farmer, D. B.; Gordon, R. G.; Dai, H., Surface Chemistry and Electrical Properties of Germanium Nanowires. *J. Am. Chem. Soc.* **2004,** *126* (37), 11602-11611.
4. Zhu, Z.; Song, Y.; Zhang, Z.; Sun, H.; Han, Y.; Li, Y.; Zhang, L.; Xue, Z.; Di, Z.; Wang, S., Vapor-solid-solid grown Ge nanowires at integrated circuit compatible temperature by molecular beam epitaxy. *J. Appl. Phys.* **2017,** *122* (9), 094304.
5. Gu, J.; Collins, S. M.; Carim, A. I.; Hao, X.; Bartlett, B. M.; Maldonado, S., Template-Free Preparation of Crystalline Ge Nanowire Film Electrodes *via* an Electrochemical Liquid–Liquid–Solid Process in Water at Ambient Pressure and Temperature for Energy Storage. *Nano Lett.* **2012,** *12* (9), 4617-4623.
6. Carim, A. I.; Collins, S. M.; Foley, J. M.; Maldonado, S., Benchtop Electrochemical Liquid–Liquid–Solid Growth of Nanostructured Crystalline Germanium. *Journal of the American Chemical Society* **2011,** *133* (34), 13292-13295.
7. Ma, L.; Lee, S.; DeMuth, J.; Maldonado, S., Direct electrochemical deposition of crystalline silicon nanowires at T ≥ 60 °C. *RSC Advances* **2016,** *6* (82), 78818-78825.
8. Mahenderkar, N. K.; Liu, Y.-C.; Koza, J. A.; Switzer, J. A., Electrodeposited Germanium Nanowires. *ACS Nano* **2014,** *8* (9), 9524-9530.
9. Fahrenkrug, E.; Gu, J.; Jeon, S.; Veneman, P. A.; Goldman, R. S.; Maldonado, S., Room-Temperature Epitaxial Electrodeposition of Single-Crystalline Germanium Nanowires at the Wafer Scale from an Aqueous Solution. *Nano Lett.* **2014,** *14* (2), 847-852.
10. Seifner, M. S.; Sistani, M.; Porrati, F.; Di Prima, G.; Pertl, P.; Huth, M.; Lugstein, A.; Barth, S., Direct Synthesis of Hyperdoped Germanium Nanowires. *ACS Nano* **2018,** *12* (2), 1236-1241.
11. Acharya, S.; Lancaster, M.; Maldonado, S., Semiconductor Ultramicroelectrodes: Platforms for Studying Charge-Transfer Processes at Semiconductor/Liquid Interfaces. *Analytical Chemistry* **2018,** *90* (20), 12261-12269.
12. DeMuth, J.; Ma, L.; Lancaster, M.; Acharya, S.; Cheek, Q.; Maldonado, S., Eutectic-Bismuth Indium as a Growth Solvent for the Electrochemical Liquid-Liquid-Solid Deposition of Germanium Microwires and Coiled Nanowires. *Crystal Growth & Design* **2018,** *18* (2), 677-685.
13. Fahrenkrug, E.; Biehl, J.; Maldonado, S., Electrochemical Liquid–Liquid–Solid Crystal Growth of Germanium Microwires on Hard and Soft Conductive Substrates at Low Temperature in Aqueous Solution. *Chemistry of Materials* **2015,** *27* (9), 3389-3396.
14. DeMuth, J.; Fahrenkrug, E.; Maldonado, S., Controlling Nucleation and Crystal Growth of Ge in a Liquid Metal Solvent. *Crystal Growth & Design* **2016,** *16* (12), 7130-7138.
15. de Jonge, N.; Ross, F. M., Electron microscopy of specimens in liquid. *Nat. Nanotechnol.* **2011,** *6*, 695.
16. Liao, H.-G.; Cui, L.; Whitelam, S.; Zheng, H., Real-Time Imaging of Pt₃Fe Nanorod Growth in Solution. *Science* **2012,** *336* (6084), 1011.
17. Zeng, Z.; Zheng, W.; Zheng, H., Visualization of Colloidal Nanocrystal Formation and Electrode–Electrolyte Interfaces in Liquids Using TEM. *Acc. Chem. Res.* **2017,** *50* (8), 1808-1817.
18. Zeng, Z.; Liang, W.-I.; Liao, H.-G.; Xin, H. L.; Chu, Y.-H.; Zheng, H., Visualization of Electrode–Electrolyte Interfaces in LiPF6/EC/DEC Electrolyte for Lithium Ion Batteries *via In-Situ* TEM. *Nano Lett.* **2014,** *14* (4), 1745-1750.
19. Evans, J. E.; Jungjohann, K. L.; Browning, N. D.; Arslan, I., Controlled Growth of Nanoparticles from Solution with *In Situ* Liquid Transmission Electron Microscopy. *Nano Lett.* **2011,** *11* (7), 2809-2813.

20. Gu, M.; Parent, L. R.; Mehdi, B. L.; Unocic, R. R.; McDowell, M. T.; Sacci, R. L.; Xu, W.; Connell, J. G.; Xu, P.; Abellan, P.; Chen, X.; Zhang, Y.; Perea, D. E.; Evans, J. E.; Lauhon, L. J.; Zhang, J.-G.; Liu, J.; Browning, N. D.; Cui, Y.; Arslan, I.; Wang, C.-M., Demonstration of an Electrochemical Liquid Cell for Operando Transmission Electron Microscopy Observation of the Lithiation/Delithiation Behavior of Si Nanowire Battery Anodes. *Nano Lett.* **2013,** *13* (12), 6106-6112.
21. Jungjohann, K. L.; Evans, J. E.; Aguiar, J. A.; Arslan, I.; Browning, N. D., Atomic-Scale Imaging and Spectroscopy for *In Situ* Liquid Scanning Transmission Electron Microscopy. *Microsc. Microanal.* **2012,** *18* (3), 621-627.
22. Liang, X.; Kim, Y.-G.; Gebergziabiher, D. K.; Stickney, J. L., Aqueous Electrodeposition of Ge Monolayers. *Langmuir* **2010,** *26* (4), 2877-2884.
23. Dickey, M. D.; Chiechi, R. C.; Larsen, R. J.; Weiss, E. A.; Weitz, D. A.; Whitesides, G. M., Eutectic Gallium-Indium (EGaIn): A Liquid Metal Alloy for the Formation of Stable Structures in Microchannels at Room Temperature. *Adv. Funct. Mater.* **2008,** *18* (7), 1097-1104.
24. Kattner, U. R., Phase Diagrams for Lead-Free Solder Alloys. *JOM* **2002,** *54*, 45-51.
25. Fahrenkrug, E.; Maldonado, S., Electrochemical Liquid–Liquid–Solid (ec-LLS) Crystal Growth: A Low-Temperature Strategy for Covalent Semiconductor Crystal Growth. *Accounts of Chemical Research* **2015,** *48* (7), 1881-1890.
26. Yarema, M.; Wörle, M.; Rossell, M. D.; Erni, R.; Caputo, R.; Protesescu, L.; Kravchyk, K. V.; Dirin, D. N.; Lienau, K.; von Rohr, F.; Schilling, A.; Nachtegaal, M.; Kovalenko, M. V., Monodisperse Colloidal Gallium Nanoparticles: Synthesis, Low Temperature Crystallization, Surface Plasmon Resonance and Li-Ion Storage. *J. Am. Chem. Soc.* **2014,** *136* (35), 12422-12430.
27. Kind, C.; Feldmann, C., One-Pot Synthesis of In0 Nanoparticles with Tuned Particle Size and High Oxidation Stability. *Chem. Mater.* **2011,** *23* (22), 4982-4987.
28. Wu, Y.; Yang, P., Direct Observation of Vapor−Liquid−Solid Nanowire Growth. *J. Am. Chem. Soc.* **2001,** *123* (13), 3165-3166.
29. Olesinski, R. W.; Kanani, N.; Abbaschian, G. J., The Ga−Si (Gallium-Silicon) system. *Bulletin of Alloy Phase Diagrams* **1985,** *6* (4), 362-364.
30. Gu, H.; Li, G.; Liu, C.; Yuan, F.; Han, F.; Zhang, L.; Wu, S., Considerable knock-on displacement of metal atoms under a low energy electron beam. *Scientific Reports* **2017,** *7* (1), 184.
31. Anderson, T. J.; Ansara, I., The Ga-In (Gallium-Indium) System. *J. Phase Equilib.* **1991,** *12* (1), 64-72.
32. Zhang, J.; Zheng, Y.; Zhao, D.; Yang, S.; Yang, L.; Liu, Z.; Zhang, R.; Wang, S.; Zhang, D.; Chen, L., Ellipsometric Study on Size-Dependent Melting Point of Nanometer-Sized Indium Particles. *The Journal of Physical Chemistry C* **2016,** *120* (19), 10686-10690.
33. Jin, B.; Sushko, M. L.; Liu, Z.; Jin, C.; Tang, R., *In Situ* Liquid Cell TEM Reveals Bridge-Induced Contact and Fusion of Au Nanocrystals in Aqueous Solution. *Nano Lett.* **2018,** *18* (10), 6551-6556.
34. Niu, K.-Y.; Liao, H.-G.; Zheng, H., Visualization of the Coalescence of Bismuth Nanoparticles. *Microsc. Microanal.* **2014,** *20* (2), 416-424.
35. Woehl, T. J.; Park, C.; Evans, J. E.; Arslan, I.; Ristenpart, W. D.; Browning, N. D., Direct Observation of Aggregative Nanoparticle Growth: Kinetic Modeling of the Size Distribution and Growth Rate. *Nano Lett.* **2014,** *14* (1), 373-378.
36. Grogan, J. M.; Schneider, N. M.; Ross, F. M.; Bau, H. H., Bubble and Pattern Formation in Liquid Induced by an Electron Beam. *Nano Lett.* **2014,** *14* (1), 359-364.
37. Zheng, H.; Smith, R. K.; Jun, Y.-w.; Kisielowski, C.; Dahmen, U.; Alivisatos, A. P., Observation of Single Colloidal Platinum Nanocrystal Growth Trajectories. *Science* **2009,** *324* (5932), 1309.
38. Keck, P. H.; Broder, J., The Solubility of Silicon and Germanium in Gallium and Indium. *Physical Review* **1953,** *90* (4), 521-522.
39. Olesinski, R. W.; Abbaschian, G. J., The Ga−Ge (Gallium-Germanium) system. *Bulletin of Alloy Phase Diagrams* **1985,** *6* (3), 258-262.

40. Chen, W.; Yu, L.; Misra, S.; Fan, Z.; Pareige, P.; Patriarche, G.; Bouchoule, S.; Cabarrocas, P. R. i., Incorporation and redistribution of impurities into silicon nanowires during metal-particle-assisted growth. *Nature Communications* **2014,** *5* (1), 4134.
41. Heitsch, A. T.; Fanfair, D. D.; Tuan, H.-Y.; Korgel, B. A., Solution−Liquid−Solid (SLS) Growth of Silicon Nanowires. *J. Am. Chem. Soc.* **2008,** *130* (16), 5436-5437.
42. Wang, F.; Dong, A.; Buhro, W. E., Solution–Liquid–Solid Synthesis, Properties, and Applications of One-Dimensional Colloidal Semiconductor Nanorods and Nanowires. *Chem. Rev. (Washington, DC, U. S.)* **2016,** *116* (18), 10888-10933.
43. Noh, K. W.; Liu, Y.; Sun, L.; Dillon, S. J., Challenges associated with in-situ TEM in environmental systems: The case of silver in aqueous solutions. *Ultramicroscopy* **2012,** *116*, 34-38.
44. Park, J. H.; Schneider, N. M.; Grogan, J. M.; Reuter, M. C.; Bau, H. H.; Kodambaka, S.; Ross, F. M., Control of Electron Beam-Induced Au Nanocrystal Growth Kinetics through Solution Chemistry. *Nano Lett.* **2015,** *15* (8), 5314-5320.
45. Woehl, T. J.; Evans, J. E.; Arslan, I.; Ristenpart, W. D.; Browning, N. D., Direct *In Situ* Determination of the Mechanisms Controlling Nanoparticle Nucleation and Growth. *ACS Nano* **2012,** *6* (10), 8599-8610.
46. Bresin, M.; Chamberlain, A.; Donev, E. U.; Samantaray, C. B.; Schardien, G. S.; Hastings, J. T., Electron-Beam-Induced Deposition of Bimetallic Nanostructures from Bulk Liquids. *Angew. Chem.* **2013,** *125* (31), 8162-8165.
47. Woehl, T. J.; Abellan, P., Defining the radiation chemistry during liquid cell electron microscopy to enable visualization of nanomaterial growth and degradation dynamics. *J. Microsc.* **2017,** *265* (2), 135-147.
48. Kallesøe, C.; Wen, C.-Y.; Booth, T. J.; Hansen, O.; Bøggild, P.; Ross, F. M.; Mølhave, K., *In Situ* TEM Creation and Electrical Characterization of Nanowire Devices. *Nano Lett.* **2012,** *12* (6), 2965-2970.
49. Kallesøe, C.; Wen, C.-Y.; Mølhave, K.; Bøggild, P.; Ross, F. M., Measurement of Local Si-Nanowire Growth Kinetics Using *In Situ* Transmission Electron Microscopy of Heated Cantilevers. *Small* **2010,** *6* (18), 2058-2064.
50. Kodambaka, S.; Hannon, J. B.; Tromp, R. M.; Ross, F. M., Control of Si Nanowire Growth by Oxygen. *Nano Lett.* **2006,** *6* (6), 1292-1296.
51. Chockla, A. M.; Korgel, B. A., Seeded germanium nanowire synthesis in solution. *J. Mater. Chem.* **2009,** *19* (7), 996-1001.
52. Fahrenkrug, E.; Alsem, D. H.; Salmon, N.; Maldonado, S., Electrochemical Measurements in *In Situ* TEM Experiments. *J. Electrochem. Soc.* **2017,** *164* (6), H358-H364.
53. *Liquid Cell Electron Microscopy*. Cambridge University Press: Cambridge, 2016.
54. Francis, Z.; Incerti, S.; Karamitros, M.; Tran, H. N.; Villagrasa, C., Stopping power and ranges of electrons, protons and alpha particles in liquid water using the Geant4-DNA package. *Nuclear Instruments and Methods in Physics Research Section B: Beam Interactions with Materials and Atoms* **2011,** *269* (20), 2307-2311.
55. Meesungnoen, J.; Jay-Gerin, J.-P.; Filali, A.; Mankhetkorn, S., Low-Energy Electron Penetration Range in Liquid Water. *Radiat. Res.* **2002,** *158*, 657-60.
56. Gupta, T.; Schneider, N. M.; Park, J. H.; Steingart, D.; Ross, F. M., Spatially dependent dose rate in liquid cell transmission electron microscopy. *Nanoscale* **2018,** *10* (16), 7702-7710.
57. Newbury, D. E.; Joy, D. C.; Goldstein, J. I.; Ritchie, N. W. M.; Scott, J. H. J.; Michael, J. R.; SpringerLink (Online service). Scanning Electron Microscopy and X-Ray Microanalysis. 4th ed.; Springer: New York, 2017. https://link.springer.com/10.1007/978-1-4939-6676-9.
58. Zhang, T.; Fahrenkrug, E.; Maldonado, S., Electrochemical Liquid-Liquid-Solid Deposition of Ge at Hg Microdroplet Ultramicroelectrodes. *Journal of The Electrochemical Society* **2016,** *163* (9), D500-D505.
59. Kashchiev, D., Dependence of the Growth Rate of Nanowires on the Nanowire Diameter. *Cryst. Growth Des.* **2006,** *6* (5), 1154-1156.

60. Weyher, J., Some notes on the growth kinetics and morphology of VLS silicon crystals grown with platinum and gold as liquid-forming agents. *J. Cryst. Growth* **1978,** *43* (2), 235-244.
61. Nebol'sin, V. A.; Shchetinin, A. A.; Dolgachev, A. A.; Korneeva, V. V., Effect of the Nature of the Metal Solvent on the Vapor-Liquid-Solid Growth Rate of Silicon Whiskers. *Inorganic Materials* **2005,** *41* (12), 1256-1259.
62. Shakthivel, D.; Raghavan, S., Vapor-liquid-solid growth of Si nanowires: A kinetic analysis. *J. Appl. Phys.* **2012,** *112* (2), 024317.
63. Dubrovskii, V. G.; Sibirev, N., General form of the dependences of nanowire growth rate on the nanowire radius. *J. Cryst. Growth* **2007,** *304*, 504–513.
64. Li, N.; Li, W.; Liu, L.; Tan, T. Y., A nucleation-growth model of nanowires produced by the vapor-liquid-solid process. *J. Appl. Phys.* **2013,** *114* (6), 064302.
65. Schmidt, V., Diameter dependence of the growth velocity of silicon nanowires synthesized *via* the vapor-liquid-solid mechanism. *Phys. Rev. B* **2007,** *75*.
66. Schubert, L.; Werner, P.; Zakharov, N. D.; Gerth, G.; Kolb, F. M.; Long, L.; Gösele, U.; Tan, T. Y., Silicon nanowhiskers grown on 〈111〉 Si substrates by molecular-beam epitaxy. *Appl. Phys. Lett.* **2004,** *84* (24), 4968-4970.
67. Givargizov, E. I., FUNDAMENTAL ASPECTS OF VLS GROWTH. In *Vapour Growth and Epitaxy*, Cullen, G. W.; Kaldis, E.; Parker, R. L.; Rooymans, C. J. M., Eds. Elsevier: 1975; pp 20-30.
68. Rudolph, P., Fundamentals of Defects in Crystals. *AIP Conf. Proc.* **2007,** *916* (1), 69-92.
69. Belloni, J., Nucleation, growth and properties of nanoclusters studied by radiation chemistry: Application to catalysis. *Catal. Today* **2006,** *113* (3), 141-156.
70. Rojas, J. V.; Castano, C. H., Radiolytic synthesis of iridium nanoparticles onto carbon nanotubes. *Journal of Nanoparticle Research* **2014,** *16* (8), 2567.

CHAPTER 3

X-Ray Reflectivity of Hg Electrode/Electrolyte Interface in Electrochemical Liquid-Liquid-Solid Processes to Study Adlayer Formation in Aqueous Borate Electrolytes Containing Dissolved GeO2

3.1 Introduction

Electrodeposition of inorganic solids at liquid electrolyte/liquid metal interfaces is a promising strategy for synthesizing important crystalline inorganic materials at unusually low temperatures and otherwise 'green' conditions. A chief advantage in the electrochemical liquid-liquid-solid (ec-LLS)[1] process is low temperature crystal growth is possible. However, progress in identifying all the relevant atomic structure at a liquid electrolyte/liquid metal interfaces is nascent. The ability to advance ec-LLS for purposes such as realizing low-cost photovoltaics requires further elaboration of the relevant factors in ec-LLS.[2-5]

In ec-LLS, solutes are introduced into liquid metals by electroreduction of precursors at the liquid metal/liquid electrolyte interface.[6-11] Despite the importance of the interface, relatively little is known about its structure and composition. X-ray reflectivity methods represent a powerful set of techniques to probe such interfaces.[12-15] Information about the electron density profile along the surface normal (and consequently the composition and structure of the interface) can be obtained.[14, 16-18] The wealth of existing data regarding X-ray reflectivity measurements specifically on Hg suggest that studying ec-LLS systems that employ Hg as the liquid metal electrode are a good starting point.

This report represents the first stage of using X-ray reflectivity to interrogate an ec-LLS system. Specifically, we focus on a Hg pool electrode immersed in a solution containing dissolved GeO_2, a potent electrolyte for Ge crystal growth.[2-3, 5, 9] This study focuses on measurements that address three questions in this system prior to Ge electrodeposition. First, how does the nature of the Hg/electrolyte interface used to perform Ge ec-LLS compare to other aqueous electrolytes?

Second, are there any persistent species at the liquid Hg/electrolyte interface? Third, does the Hg surface condition and near-surface atomic structure change at potentials relevant to the electroreduction of GeO_2 into Ge crystallites?

3.2 Experimental

Materials Germanium(IV) oxide (99.999%, ChemPur), sodium tetraborate (99.998%, ChemPur), and mercury (99.999+%, ChemPur) were used as received. Water with a resistivity >18.2 MΩ·cm (Nanopure Barnstead Water Purification) was used throughout.

X-Ray Reflectivity Measurement XRR measurements of the liquid metal/liquid electrolyte interfaces were performed using the Liquid Interface Scattering Apparatus (LISA) diffractometer[19] and synchrotron source (λ = 4.959 nm) in beamline P08 in PETRA III at DESY in Hamburg, Germany. A beam energy of 25 keV and a GaAs Lambda detector (1536 x 512 array of pixels with a pixel height of 55 μm corresponding to a resolution of 3.3 x 10^{-4} $Å^{-1}$ in both the horizontal q_x and vertical q_z directions) with horizontal and vertical acceptances of 0.08° and 0.04°, respectively, were used for all measurements. Beam attenuators were used to ensure that the count intensity was ≤ 10^5 counts per pixel. Raw data from the GaAs Lambda detector was first treated by a flat-field correction algorithm to account for variable pixel responsivity (i.e. fixed-pattern noise).[20] Detector images were normalized using a flat field image provided by the detector manufacture prepared for the specific beam energy. The background intensity from X-ray scattering from bulk Hg and the electrolyte was determined by setting a 0.08° horizontal offset to the detector followed by subtraction of the 0.08° horizontal and 0.04° vertical acceptance from the specular intensity.

A custom designed electrochemical X-ray scattering cell described previously[21] with PEEK windows and a 2.5 cm radius for the Hg pool was used (Figure 3.1). Electrolyte solutions were purged with $N_2(g)$ for at least 30 minutes prior to injection into the cell. Upon assembly, the Hg electrode was held at a constant potential with respect to a saturated calomel electrode (SCE) for at least 15 minutes before each reflectivity measurement to ensure a stable interface. All potentials are reported here with respect to this same reference. A digital, computer controlled Ametek Modulab potentiostat was used throughout. For every XRR measurement, at least two repetitions were collected. To eliminate the possibility of cumulative, systematic bias, XRR data acquired at constant potential were randomized with respect to the value of the applied potential.

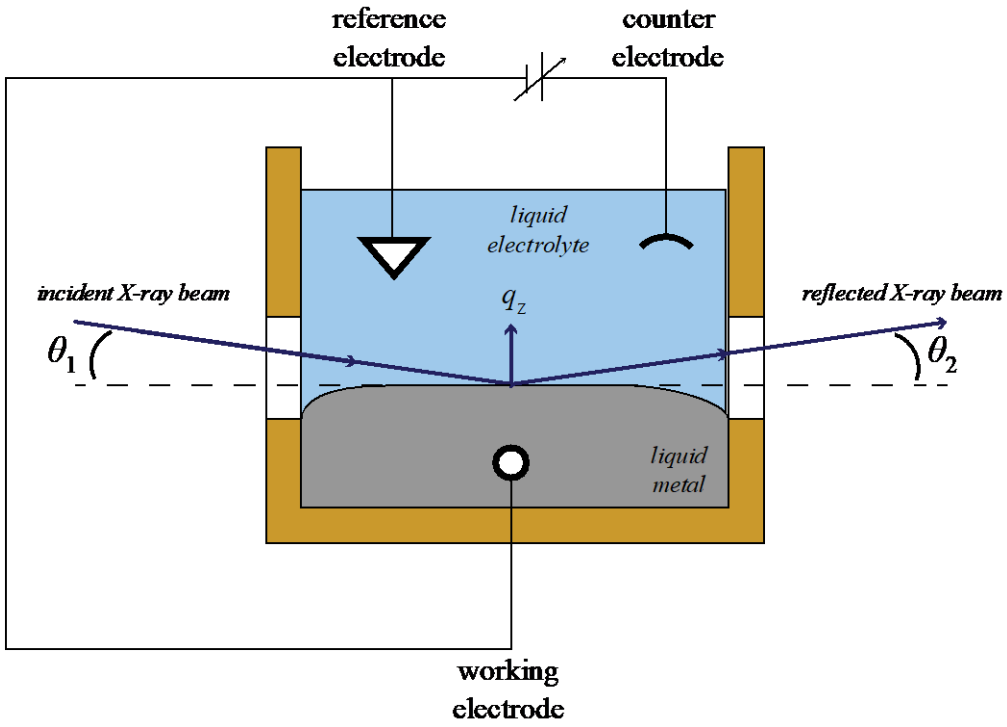

Figure 3.1. Schematic illustration of the electrochemical cell and the X-ray beam path used for in-situ X-ray reflectivity and grazing incidence X-ray diffraction measurements.

X-Ray Reflectivity Data Analysis The background-subtracted detector signal was first normalized by the direct beam intensity and then plotted versus the surface-normal scattering vector, q_z. The resulting experimental X-ray reflectivity (R) was normalized by the Fresnel reflectivity (R_F) of a perfectly sharp interface between Hg and the aqueous electrolyte. The normalized data (R/R_F) were fit with two related approaches of the 'distorted crystal model'[14, 22] that yielded similar quality fits and implied equivalent structures of the electrode/interface; the 'First Layer'[23] model and the 'adlayer' model.[24]. The text here focuses exclusively on fitting using the 'adlayer' model.[24] Equation 3.1 was used for solutions containing 0.1 M $Na_2B_4O_7$ and equation 3.2 was used for solutions containing 0.1 M $Na_2B_4O_7$ + 0.05 M GeO_2.

$$\frac{\langle\rho_e(z)\rangle}{\rho_{e,Hg}} = F_{Hg}(z) \otimes \left[\frac{\rho_{ad}}{\rho_{e,Hg}} \frac{1}{\sigma_{ad}\sqrt{2\pi}} e^{\frac{-(z-z_{ad})^2}{2\sigma_{ad}^2}} + \sum_{n=1}^{\infty} \frac{d}{\sqrt{\sigma_i^2 + n\sigma_b^2}\sqrt{2\pi}} e^{\frac{-(z-nd)^2}{2(\sigma_i^2+n\sigma_b^2)}} \right] + \frac{1}{2}\frac{\rho_{e,H_2O}}{\rho_{e,Hg}} \left(1 - \mathrm{erf}\left(\frac{z - z_{H_2O}}{\sigma_{H_2O}\sqrt{2}} \right) \right) \tag{3.1}$$

$$\frac{\langle\rho_e(z)\rangle}{\rho_{e,Hg}} = F_{Hg}(z) \otimes \left[\sum_{n=1}^{\infty} \frac{d}{\sqrt{\sigma_i^2 + n\sigma_b^2}\sqrt{2\pi}} e^{\frac{-(z-nd)^2}{2(\sigma_i^2+n\sigma_b^2)}} \right] + \sum_{j=1}^{N} \left(\begin{array}{l} F_{Ge}(z) \otimes \frac{\theta_{Ge,j}}{\rho_{e,Hg}} \frac{1}{\sigma_{Ge,j}\sqrt{2\pi}} e^{\frac{-(z-z_{Ge,j})^2}{2\sigma_{Ge,j}}} \\ + F_O(z) \otimes \frac{\theta_{O,j}}{\rho_{e,Hg}} \frac{1}{\sigma_{O,j}\sqrt{2\pi}} e^{\frac{-(z-z_{O,j})^2}{2\sigma_{O,j}}} \end{array} \right) + \frac{1}{2}\frac{\rho_{e,H_2O}}{\rho_{e,Hg}} \left(1 - \mathrm{erf}\left(\frac{z - z_{H_2O}}{\sigma_{H_2O}\sqrt{2}} \right) \right) \tag{3.2}$$

where ρ_{ad}, σ_{ad}, and z_{ad} are respectively the amplitude, root mean square displacement, and position of the low density Hg adlayer, d is the spacing between the atomic layers, σ_i is the intrinsic roughness of each layer in the liquid metal and σ_b describes the increase in roughness as n increases,

θ_M, σ_M, and z_M are respectively the fractional surface coverage, root mean square displacement, and position of the gaussian term corresponding to element *M*, z_{H_2O} & σ_{H_2O} describe the position and width of the electrolyte front. Finally, $F_M(z)$ is the Fourier transform of the form factor for the respective element *M*.[25]

Both forms of the distorted crystal model were applied to the experimental XRR in a sequential process through a custom python script. The first round of fitting was focused on global optimization, using pre-defined upper and lower bounds for each fitting parameter. Subsequent fitting rounds were performed on refining the value of each parameter individually. Final fits were determined when the corresponding χ^2 value fell below a threshold value of 0.1.

3.3 Results

Figure 3.2 presents the voltammetric behavior of Hg immersed in either aqueous 0.1 M $Na_2B_4O_7$ or aqueous 0.1 M $Na_2B_4O_7$ with 0.05 M dissolved GeO_2. In this potential range, Hg is neither electrochemically oxidized nor does it readily support H^+ reduction, as shown by the dashed line in Figure 3.2a. Repeated scanning of Hg in the blank electrolyte over this potential range effected no change in voltammetric response. Although the potential range in Figure 3.2 was not sufficiently negative to support the $4e^-$ reduction of dissolved GeO_2, addition of dissolved GeO_2 to the $Na_2B_4O_7$ electrolyte effected a clear change in the voltammetric response (Figure 3.2a, solid line). A notable increase in oxidative current at potentials more positive than -0.2 V was noted specifically in the presence of dissolved GeO_2. Similarly, there was a notable increase in reductive current in this potential range upon sweeping the potential to more negative values. The excess reductive current faded upon repeated cycling provided that the applied potential was not made more positive than -0.2 V (Figure 3.2b).

To ascertain whether the voltammetry changes reflected a transient or persistent change in the physicochemical properties of the Hg surface, X-ray reflectivity measurements of the electrode/electrolyte interface were obtained under potential control. Figure 3.3 shows absolute and normalized X-ray reflectivity data collected at several potentials when Hg was immersed in 0.1 M $Na_2B_4O_7$. In both Figure 3.3a and 3.3b, the data are overlaid with both the calculated Fresnel reflectivity for the water/Hg interface and with the best-fit 'first layer' distorted crystal model. From each fit, corresponding electron density profiles were generated (Figure 3.3c).

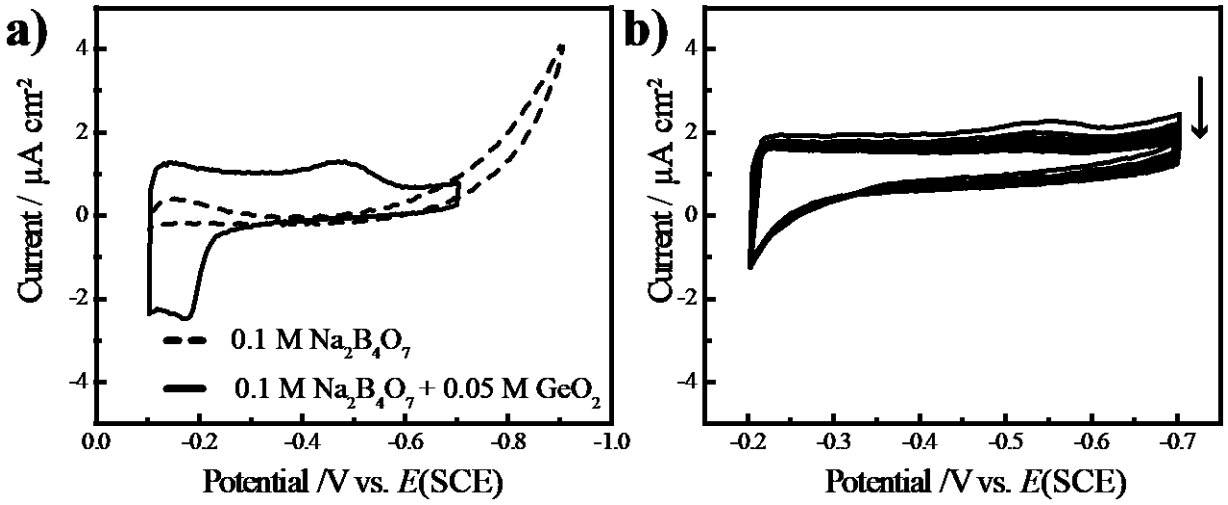

Figure 3.2. a) Voltammetric responses for a mercury electrode immersed in (dashed line) a 0.1 M $Na_2B_4O_7$(*aq*) and in (solid line) a 0.1 M $Na_2B_4O_7$(*aq*) and 0.05 M GeO_2 (red). Scan rate: 0.02 V s^{-1} b) Multiple voltammetric responses for a mercury electrode immersed in a 0.1 M $Na_2B_4O_7$(aq) and 0.05 M GeO_2 solution. The arrow notates a loss of current passed on subsequent scans. Scan rate: 0.02 V s^{-1}

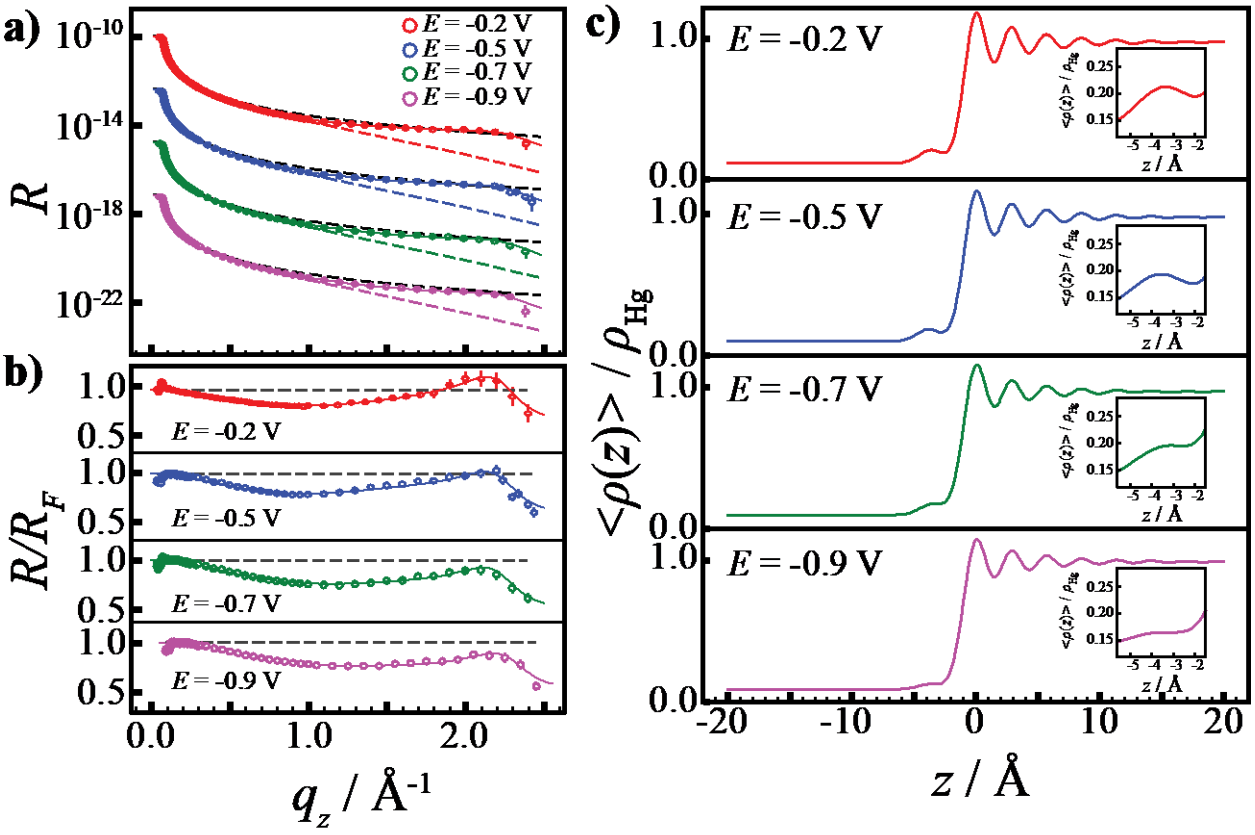

Figure 3.3. Plot of a) the absolute X-ray reflectivity vs. momentum transfer perpendicular to the surface and b) the same X-ray reflectivity normalized to the Fresnel reflectivity (bottom) for a Hg electrode immersed in deaerated 0.1 M $Na_2B_4O_7$ at four different potentials: E = -0.2 V (red symbols), -0.5 V (blue symbols), -0.7 V (green symbols), -0.9 V (pink symbols). Solid lines denote the corresponding best fit of the data while the dashed lines correspond to the reflectivity of an interface with a monotonic electron density profile with a roughness of 1.00 Å. c) Electron density profiles corresponding to the fitted data shown in b). Insets: Cropped plot of the corresponding electron density profile from q_z = -2 to -5 Å^{-1} for clarity of the low density Hg adlayer. Insets: Cropped plot of the corresponding electron density profile from q_z = -2 to -5 Å^{-1} for clarity of the low density Hg adlayer.

Several general features were noted in these data. First, in every XRR profile, a discernable layering peak centered at q_z = 2.22 Å^{-1} was noted. The position and intensity of this peak was consistent with atomic layering within the near surface region of Hg.[17, 26-27] Second, these XRR data could be fit solely with parameters related to the pure electrolyte and that of liquid Hg, suggesting a clean and abrupt water/Hg interface. This point is clear in the electron density profiles for all applied potentials in Figure 3.3c. Third, the fitted parameters were all in good agreement with the values of these parameters reported previously for Hg immersed in 0.01 M NaF(*aq*) (Table 3.1, Figure 3.4), a system notable for representing a pristine water/Hg interface. Figure 3.4 specifically illustrates the similarity in the XRR profiles for Hg in these two electrolytes at a comparable applied potential. Despite differing in ion identity and ionic strength, the raw data and the respective fits are statistically indistinguishable. Fourth, the intensity of the surface layering peak in Figures 3.3a,b (and the corresponding intensity of the layering visible in the electron density profiles in Figure 3.3c) decreased with more negative applied potentials, again in accord with the NaF(*aq*)/Hg system.[17, 27]

X-ray reflectivity profiles collected in electrolytes that included dissolved GeO_2 at a formal concentration of 0.05 M showed both obvious and subtle differences. Figure 3.5 shows corrected and normalized X-ray reflectivity data collected at the same potentials as in Figure 3.3 but when the electrolyte also contained dissolved GeO_2. The X-ray reflectivity data collected at E = -0.2 V exhibited a noticeably distinct profile. An additional peak centered at q_z = 0.85 Å^{-1} was evident, less intense than the surface layering peak at larger q_z values. The shape of this surface layering peak was also different. The prominence of the peak at q_z = 0.85 Å^{-1} depended somewhat on the duration the potential was held at or more positive than -0.2 V but was consistently observed at this and more positive potentials. The best fit of these XRR data were consistent with a decidedly different electron density profile (Figure 3.5c, red line). Rather than featuring an abrupt electrolyte/Hg interface, the data were best fit with a layer of intermediate electron density sandwiched between the electrolyte and the bulk Hg.

To confirm this feature was a result of the electrochemical potential, dynamic XRR measurements were recorded during the course of a voltammetric experiment. Figure 3.6 shows a cyclic voltammetric sweep initiated at E = -0.7 V, switched at E = -0.2 V, and returned to E = -0.7 V.

Table 3.1. XRR Fitting Parameters for Hg Adlayer - Distorted Crystal Model

Electrolyte	Potential	$\rho(H_2O)/\rho(Hg)$	$z(H_2O)$ /Å	$\sigma(H_2O)$ /Å	σ_i /Å	σ_b /Å	d /Å	ρ(Hg Adlayer)/ρ(Hg)	σ(Hg Adlayer) /Å	z(Hg Adlayer) /Å
0.01 M NaF										
	-0.2 V	0.10	-1.00	0.95	0.95 ± 0.01	0.48 ± 0.01	2.75	0.21 ± 0.01	0.95	-3.64 ± 0.23
0.1 M $Na_2B_4O_7$										
	-0.2 V	0.10	-1.00	0.95	0.95 ± 0.01	0.49 ± 0.01	2.75	0.22 ± 0.01	0.95	-3.69 ± 0.21
	-0.5 V	0.10	-1.00	0.97	0.97 ± 0.01	0.49 ± 0.01	2.75	0.20 ± 0.01	0.97	-3.73 ± 0.24
	-0.7 V	0.10	-1.00	1.00	1.00 ± 0.01	0.50 ± 0.01	2.75	0.19 ± 0.01	1.00	-3.51 ± 0.20
	-0.9 V	0.10	-1.00	1.01	1.01 ± 0.01	0.49 ± 0.01	2.75	0.10 ± 0.01	1.01	-3.74 ± 0.19

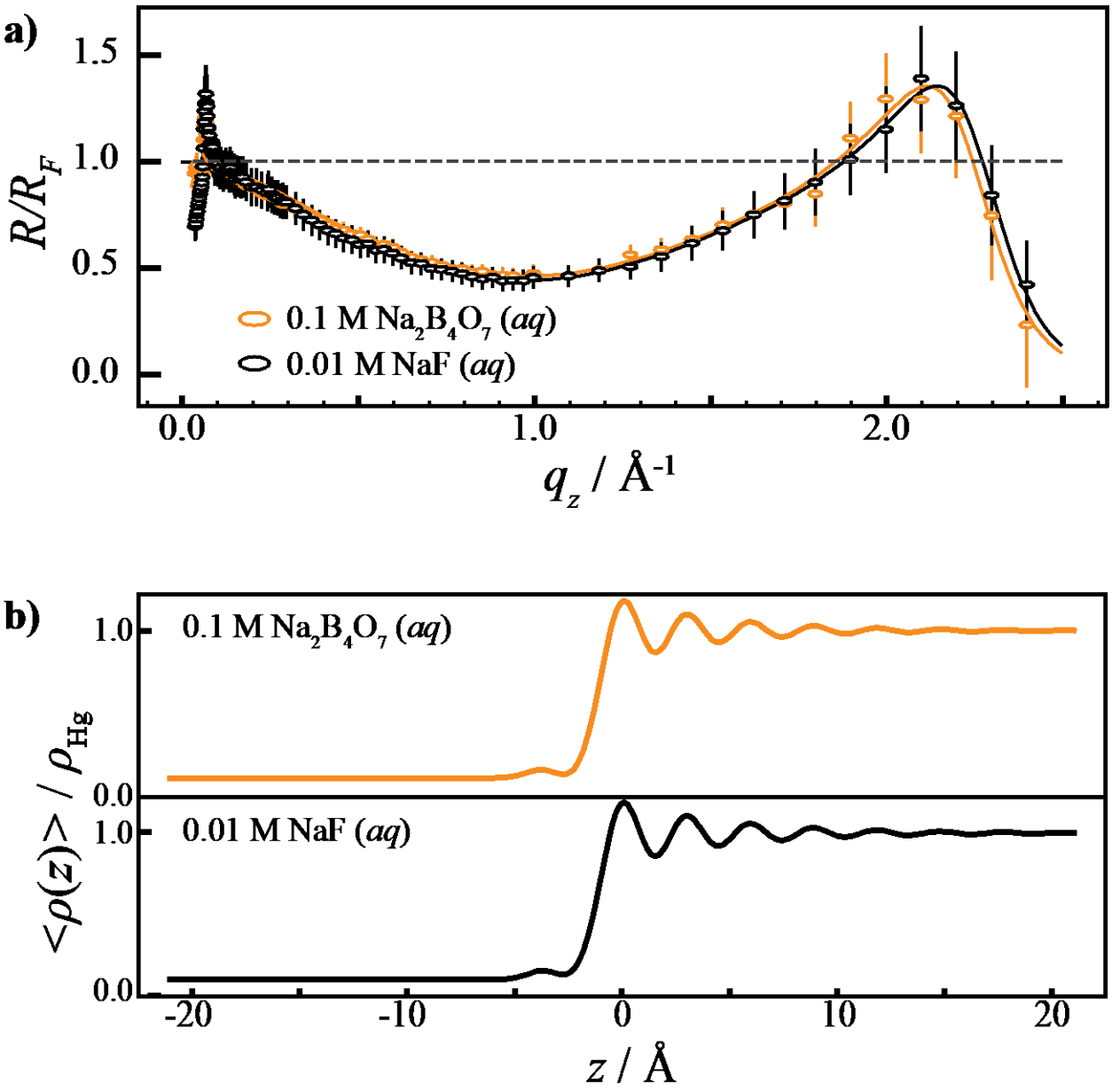

Figure 3.4. a) Plot of the X-ray reflectivity normalized to the Fresnel reflectivity vs. momentum transfer perpendicular to the surface for a Hg electrode immersed in deaerated 0.1 M $Na_2B_4O_7$ (orange) or 0.01 M NaF (black). Data for NaF are adapted from Reference 17. b) Electron density profiles corresponding to the fitted data shown in a).

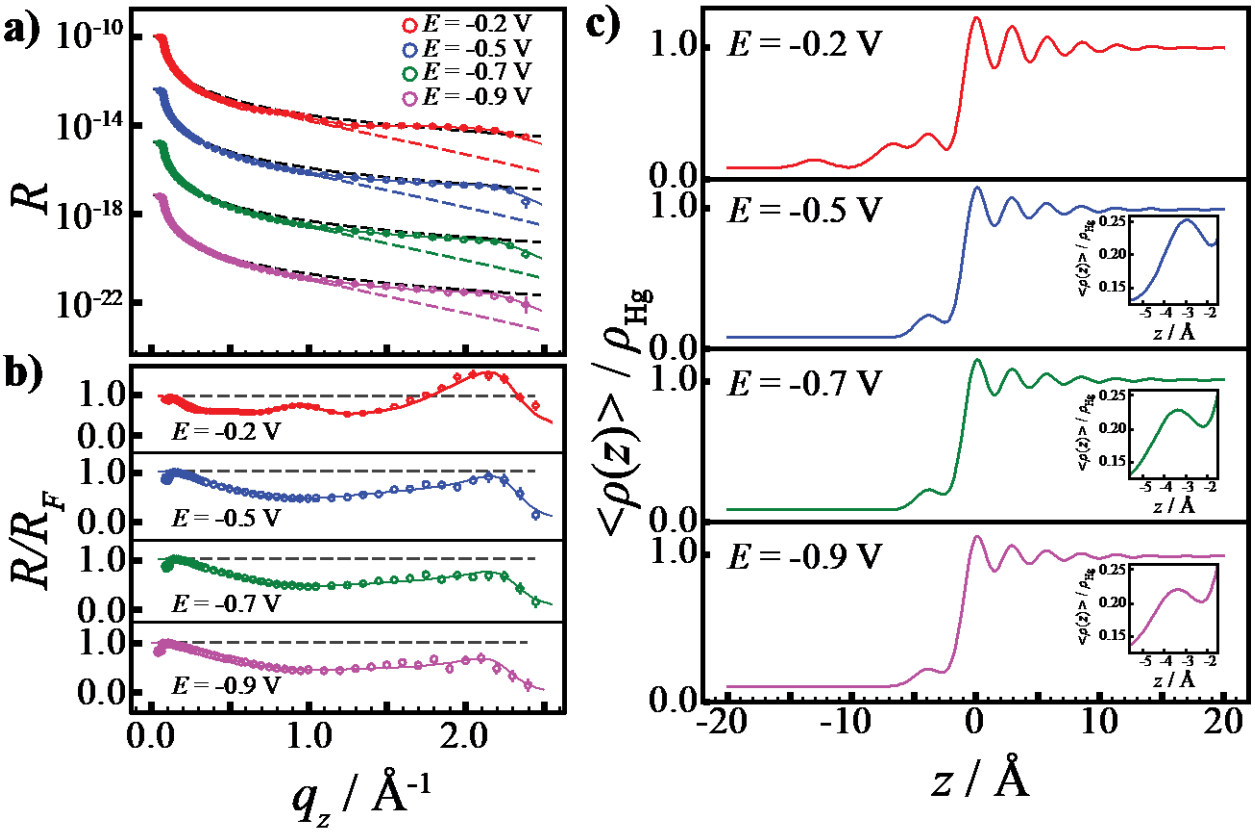

Figure 3.5. a) Plot of a) the absolute X-ray reflectivity vs. momentum transfer perpendicular to the surface and b) the same X-ray reflectivity normalized to the Fresnel reflectivity (bottom) for a Hg electrode immersed in deaerated electrolyte containing 0.1 M $Na_2B_4O_7$ and a formal concentration of 0.05 M GeO_2 at four different potentials: E = -0.2 V (red symbols), -0.5 V (blue symbols), -0.7 V (green symbols), and -0.9 V (pink symbols). Curves are offset for clarity. Solid lines denote the corresponding best fit of the data while the dashed lines correspond to the reflectivity of an interface with a monotonic electron density profile with a roughness of 1.00 Å. c) Electron density profiles corresponding to the fitted data shown in b). Insets: Cropped plot of the corresponding electron density profile from q_z = -2 to -5 Å^{-1} for clarity of the low density Hg adlayer.

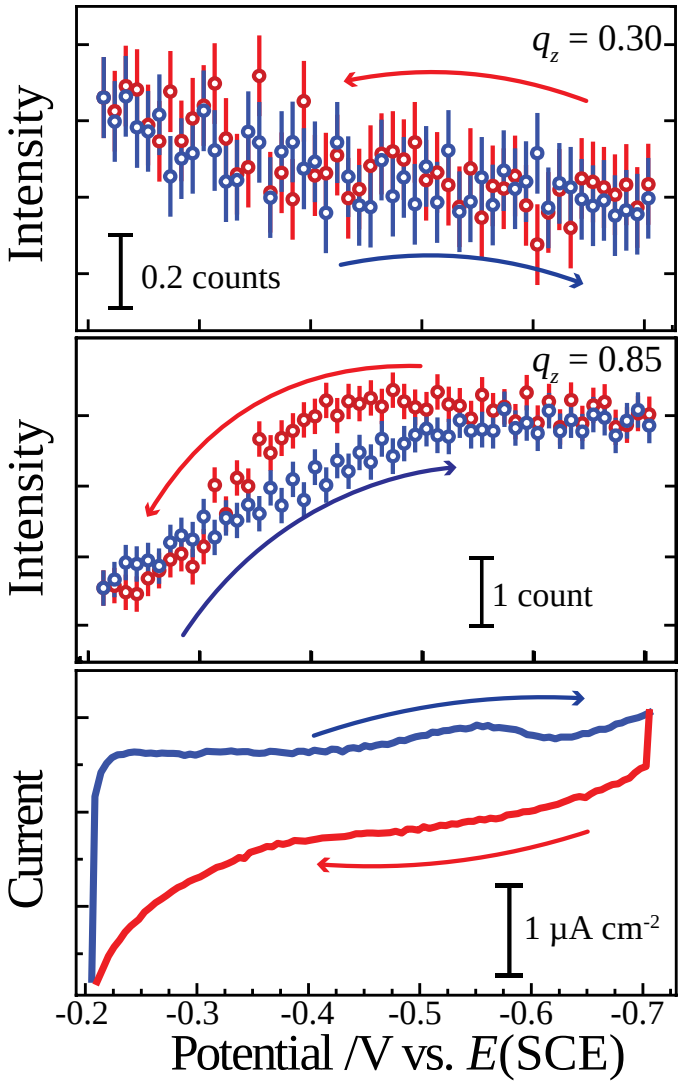

Figure 3.6. Plots depicting the reflected X-ray intensity (top, middle) recorded concurrently with c) current during a voltammetric scan at 0.05 V s^{-1} for a Hg electrode immersed in 0.1 M $Na_2B_4O_7$ and 0.05 M GeO_2. The X-ray reflectivity at q_z = (top) 0.3 Å^{-1} and (middle) 0.85 Å^{-1} are shown with arrows denoting the sweep direction.

XRR data recorded at the peak ($q_z = 0.85$ Å^{-1}) showed attenuation at potentials more positive than -0.5 V. Curiously, the X-ray reflectivity increased immediately upon changing the sweep direction, reaching the initial value once the potential was made more negative than -0.5 V. In this way, the XRR was not correlated strongly with the broad cathodic wave seen in the voltammetry. To eliminate experimental artifacts (e.g. potential-dependent surface roughness) that could contribute to the changes observed at $q_z = 0.85$ Å^{-1}, data were also recorded at an angle far from the peak ($q_z = 0.3$ Å^{-1}). These data showed minimal change with potential, indicating the changes in the data recorded for $q_z = 0.85$ Å^{-1} were not due to collection artifacts.

The best fit for the XRR curves collected at -0.2 V with dissolved GeO_2 occurred when several gaussians were employed to model a crystalline GeO_2 adlayer directly attached to the Hg surface followed by a sparse anion layer resting atop the crystalline GeO_2. Two facts supported the interpretation of the crystalline adlayer structure as Rutile GeO_2. First, the separation distance of the Gaussian peaks shown in Table 3.2 & Figure 3.7 was consistent with the atomic spacing for rutile GeO_2. Second, additional X-ray diffraction measurements were also collected at -0.2 V that suggested Rutile GeO_2. In these data, a single Bragg peak was consistently observed at $q_z = 2.02$ Å^{-1}, consistent with the [110] planes in rutile GeO_2.

At potentials more negative than -0.2 V, the XRR data recorded for Hg immersed in electrolyte containing dissolved GeO_2 were not consistent with a crystalline adlayer at the interface. Instead, these XRR data could generally be fit with parameters that suggested an interfacial electron density profile similar to those shown in Figure 3.3c. Still, closer inspection of the data showed subtle differences that were persistent at all potentials more negative than -0.2 V. Figure 3.7 shows overlays of the normalized XRR data with and without the presence of dissolved GeO_2 in the electrolyte at two applied potentials. There was a noticeable decrease in the normalized intensity of the specular beam in the q_z range of 0.3 to 1.3 Å^{-1} for data recorded in the electrolyte containing dissolved GeO_2 (Figure 3.8). The layering peak at larger q_z values was similarly attenuated. The reflectivity curves collected under these conditions are best fit through the addition of gaussians with the form factors corresponding to Ge and O, indicative of the presence of an adsorbed species on the surface.

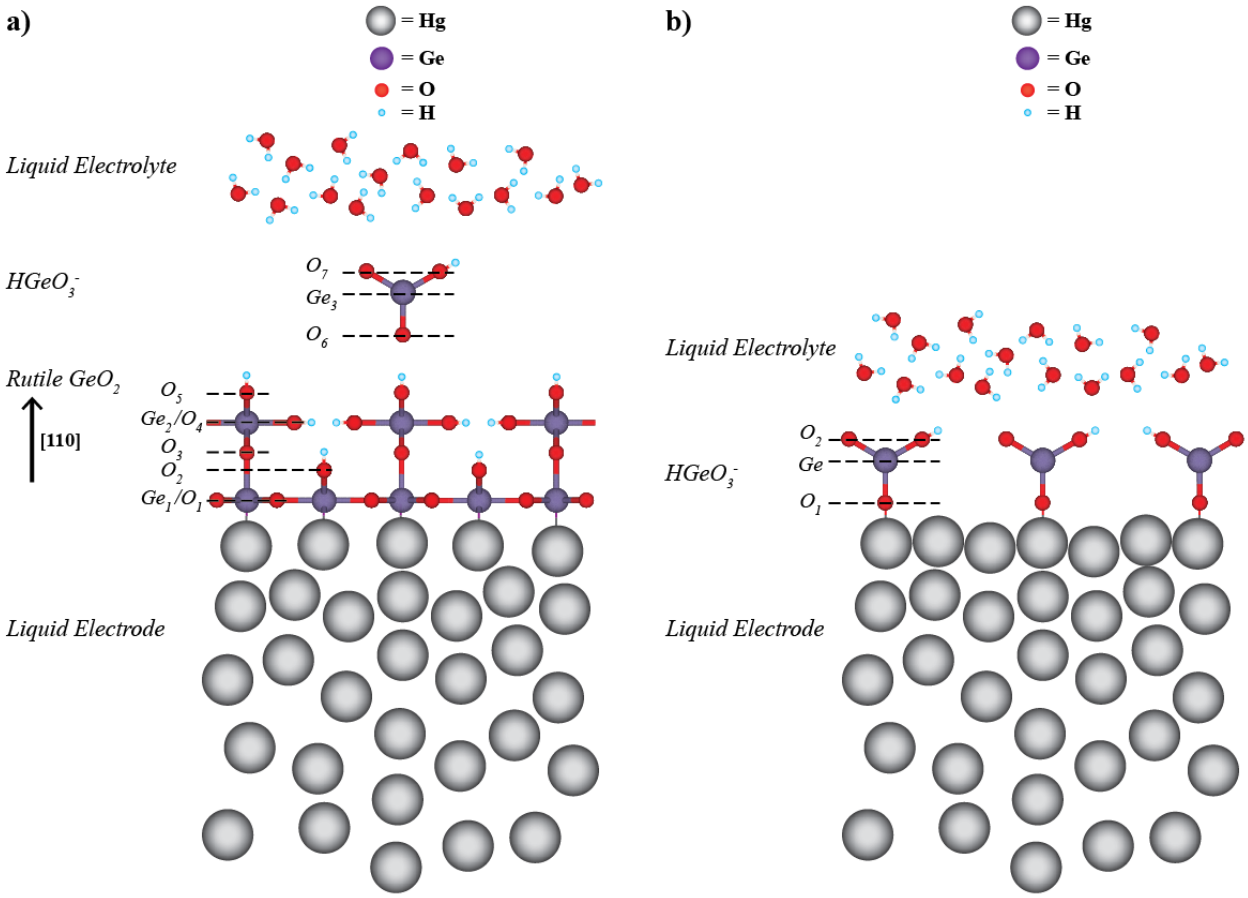

Figure 3.7. Proposed structures of adlayer at a) positive and b) negative potentials. Labels on adlayer structures indicate the labels used for the relevant layer parameters in tables 3.2 and 3.3.

Table 3.2. XRR Fitting Parameters for Hg Biased at -0.2 V in 0.1 M $Na_2B_4O_7$ + 0.05 M GeO_2

Layer	σ_i /Å	σ_b /Å	d /Å	θ	z /Å	σ /Å
Hg	1.02 ± 0.01	0.50 ± 0.01	2.75	--	--	--
H_2O	--	--	--	--	-11.96 ± 0.17	1.02 ± 0.01
Ge_1	--	--	--	0.71 ± 0.03	-3.56	1.02 ± 0.01
Ge_2	--	--	--	0.45 ± 0.02	-6.61	1.02 ± 0.01
Ge_3	--	--	--	0.15 ± 0.02	-13.00	1.02 ± 0.01
O_1	--	--	--	0.71 ± 0.03	-2.39	1.02 ± 0.01
O_2	--	--	--	0.71 ± 0.03	-3.56	1.02 ± 0.01
O_3	--	--	--	0.45 ± 0.02	-4.73	1.02 ± 0.01
O_4	--	--	--	0.45 ± 0.02	-5.46	1.02 ± 0.01
O_5	--	--	--	0.45 ± 0.02	-6.61	1.02 ± 0.01
O_6	--	--	--	0.15 ± 0.02	-11.67	1.02 ± 0.01
O_7	--	--	--	0.15 ± 0.02	-13.68	1.02 ± 0.01

*ρ (H_2O) was fixed to 0.1

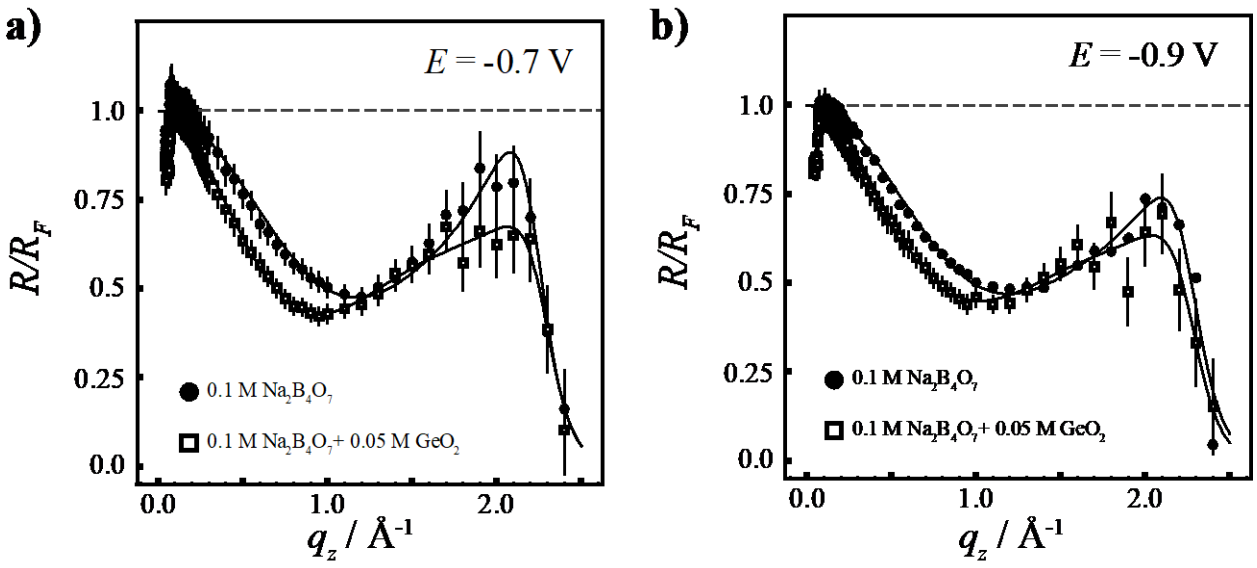

Figure 3.8. Comparison of the normalized X-ray reflectivity vs. momentum transfer perpendicular to the surface profiles for Hg electrodes immersed in either 0.1 M $Na_2B_4O_7$ (solid circles) or 0.1 M $Na_2B_4O_7$ and 0.05 M GeO_2 (hollow squares) at a) -0.70 V and b) -0.90 V.

The change in σ_i following the addition of GeO_2 provides further evidence for the presence of an adsorbate layer between -0.5 V to -0.9 V. The presence of an anion adsorbate layer would result in a lowering of the surface tension of the liquid Hg.[26] A decrease in surface tension elicits an increase in capillary wave roughness which is observed by an increase in σ_i as shown in Table 3.3. Multiple grazing incident X-ray diffraction measurements performed under these conditions consistently showed no diffraction signatures at this interface, arguing against any adlayer with crystalline order.

3.4 Discussion

The data collectively speak to the following points. First, the data suggest that the interface between Hg and borate electrolyte is devoid of any significant level of adsorbates and is otherwise similar to the Hg/NaF(*aq*) interface at all investigated potentials. Second, when Hg is immersed in borate electrolytes that also contain GeO_2, the voltammetric responses and XRR data are consistent with an ordered adlayer forming at potentials more positive than -0.2 V and being removed from the interface at potentials more negative than -0.2 V. Third, when Hg is biased sufficiently negative to remove the putative adlayer in the borate electrolyte with dissolved GeO_2, a persistent, disordered adsorbate remains. These points are discussed individually and their cumulative impact on understanding the Hg/electrolyte just prior to initiation of Ge ec-LLS are discussed below.

Hg/Borate Interface The facts that Hg immersed in a 0.1 M $Na_2B_4O_7$ solution exhibited XRR profiles comparable to XRR data for Hg immersed in NaF(aq) and that these features showed a similar potential dependence strongly suggests that this liquid metal/electrolyte interface is similarly ideal.[17, 27] That is, this electrolyte does not complicate the structure of the Hg electrode at the interface or in the near-surface region. This point is fortuitous but could not be assumed *a priori*. There are ample examples of complex adsorption behavior of borates on solid electrodes.[28] Apparently, the data argue that similar phenomena are not operative with liquid Hg. In this capacity, this electrolyte system is a good reference point to understand the physicochemical properties of the Hg interface when the electrodeposition precursor GeO_2 is added to the electrolyte.

Table 3.3. XRR Fitting Parameters for Unmodified Distorted Crystal Model with Ge and O Gaussians

Electrolyte	Potential	ρ (H_2O)/ρ (Hg)	z (H_2O) /Å	σ (H_2O) /Å	σ_i /Å	σ_b /Å	d /Å
0.1 M $Na_2B_4O_7$ + 0.05 M GeO_2							
	-0.5 V	0.10	-1.93 ± 0.11	-1.00 ± 0.01	1.00 ± 0.01	0.50 ± 0.01	2.75
	-0.7 V	0.10	-1.71 ± 0.09	-1.02 ± 0.01	1.02 ± 0.01	0.50 ± 0.01	2.75
	-0.9 V	0.10	-1.37 ± 0.06	-1.03 ± 0.01	1.03 ± 0.01	0.50 ± 0.01	2.75

Table 3.3. (Cont.) XRR Fitting Parameters for Unmodified Distorted Crystal Model with Ge and O Gaussians

Electrolyte	Potential	θ (Ge)	z (Ge) /Å	σ (Ge) /Å	θ (O_1)	z (O_1) /Å	σ(O_1) /Å	θ (O_2)
0.1 M $Na_2B_4O_7$ + 0.05 M GeO_2								
	-0.5 V	0.40 ± 0.02	-3.75	1.00 ± 0.01	0.40 ± 0.02	-4.43	1.00 ± 0.01	0.40 ± 0.02
	-0.7 V	0.35 ± 0.02	-3.75	1.02 ± 0.01	0.35 ± 0.02	-4.43	1.02 ± 0.01	0.35 ± 0.02
	-0.9 V	0.30 ± 0.02	-3.75	1.03 ± 0.01	0.30 ± 0.02	-4.43	1.03 ± 0.01	0.30 ± 0.02

Presence and Identity of Adlayer on Hg at Positive Potentials with dissolved GeO_2 Upon dissolution of 0.5 M GeO_2 into the electrolyte solution, the XRR data cumulatively indicated the Hg interface was changed and that dissolved GeO_2 had some affinity for Hg. However, the potential-dependence of the changes in the XRR appear to implicate the formation of multiple types of adlayers (Figure 3.7). At more positive potentials, the formation of a sparse $HGeO_3^-$ adlayer atop a second adlayer consistent with crystalline rutile GeO_2 is observed. The formation of this crystalline adlayer is not a result of an oxidation process of the electrolyte or Hg, since neither is oxidizable in the investigated potential range. However, the dynamic XRR suggest that the accumulation of GeO_2 at positive potentials is tied to the potential of the electrode. We posit that GeO_2 adsorption is facilitated by the Hg surface charge (Figure 3.7a, Table 3.2). Similarly, solid GeO_2 can be removed by biasing Hg towards more negative potentials without a coupled redox process per se. Whether the adlayer at positive potentials is a pure phase or a mixture of GeO_2 phases is not settled. However, the data are clear that this type of adlayer is not present at more negative potentials where Ge electrodeposition occurs.

Residual Surface Species on Hg at Negative Potentials Even after the removal of the GeO_2 adlayer at more negative potentials, the physical nature of the Hg/electrolyte interface was clearly not equivalent to the Hg/electrolyte interface in the absence of GeO_2. One possibility is that some residual species remains adsorbed on the Hg surface at more negative potentials. This hypothesis is supported by the electron density profile generated from the fits. Specifically, the data could be well fit using one gaussian corresponding to a Ge atom and two gaussians corresponding to O atoms with spacing that is consistent with the $HGeO_3^-$ anion (Figure 3.7b, Table 3.3). This is also in good agreement with the solution chemistry. In particular, at the pH of the electrolyte (pH = 9.13 for 0.1 M $Na_2B_4O_7$),[29] the primary species in solution is $HGeO_3^-$.[30]

The presence of an ionic adlayer is interesting since it is well established on Au electrodes that partially reduced GeO_x surface layers can be observed by scanning probe methods.[31] Separately, we previously observed on polycrystalline Au by surface-enhanced Raman measurements an undefined but persistent phonon mode at 200 cm^{-1} when Au electrodes were biased more negative than -0.6 V.[32] This phonon was neither definitively associated with GeO_2 and it disappeared concomitantly with the appearance of Ge-H modes near 1900 cm^{-1} at potentials more negative than -0.9 V.

Thus, one interpretation of the data here is that an adlayer of ionic $HGeO_3^-$ species is present on the surface Hg in the potential range of -0.5 to -0.9 V vs. SCE. It is unclear whether reduction of this layer would result in zero-valent Ge that then rapidly dissolves into Ge or instead form a layer of partially/fully hydrogenated Ge adatoms that facilitate electroreduction of dissolved GeO_2. In this scenario, the operative surface chemistry that would be involved in the nascent stages of Ge ec-LLS in this electrolyte would not be that of pure Hg but instead of Hg and this adlayer.

Impact on Ge ec-LLS Mechanism with Hg Electrodes The presence of an ionic, Ge-containing surface layer introduces new questions to the understanding of how Ge e-LLS proceeds. One possibility is that the adlayer represents the means by which Ge is introduced into the liquid metal during electrodeposition. That is, electroreduction to Ge^0 may occur predominantly or exclusively through the adlayer, with dissolved $HGeO_3^-$ having to first adsorb on sites left vacant by Ge^0 dissolution into bulk Hg (Figure 3.9a). Such a possibility may help explain why Ge ec-LLS is difficult to perform in very dilute electrolytes, where we have noted little to no accumulation of solid Ge crystals. Similarly, an adlayer that is first reduced to Ge-H_n surface groups on Hg could electrocatalyze the electroreduction of dissolved $HGeO_3^-$. The participation of a hydride donor may accelerate electroreduction of $HGeO_3^-$ (Figure 3.9b).[33] These two possibilities are not mutually exclusive. In fact, both scenarios are consistent with the general premise that the presence of an adlayer necessarily influences/facilitates the rate of dissolution of Ge into Hg. More work is needed to explore these possibilities and will be the focus of a separate forthcoming work.

3.5 Conclusion

The work presented ere describes a methodology for studying liquid metal electrode interfaces during the ec-LLS process. The data show that the electrolyte-liquid metal interface is permanently changed upon immersion into electrolyte containing dissolved GeO_2. This insight is impossible to verify by electrochemical data alone but is readily elucidated from the collected XRR profiles. The work here illustrates that at least two different types of adlayers form, a solid oxide at more positive potentials and a disordered ionic adlayer at more negative potentials that is consistent with $HGeO_3^-$. It is presently unclear how this facet affects or is necessary for ec-LLS. Understanding this point will be helpful in optimizing the mechanistic steps in ec-LLS to produce target crystalline materials. Thus, these observations incentivize further *in-situ* studies of the ec-

LLS process to elucidate the mechanism by which crystallites first nucleate and then grow. Subsequent work will focus on these stages of the ec-LLS process at liquid metal/electrolyte interfaces.

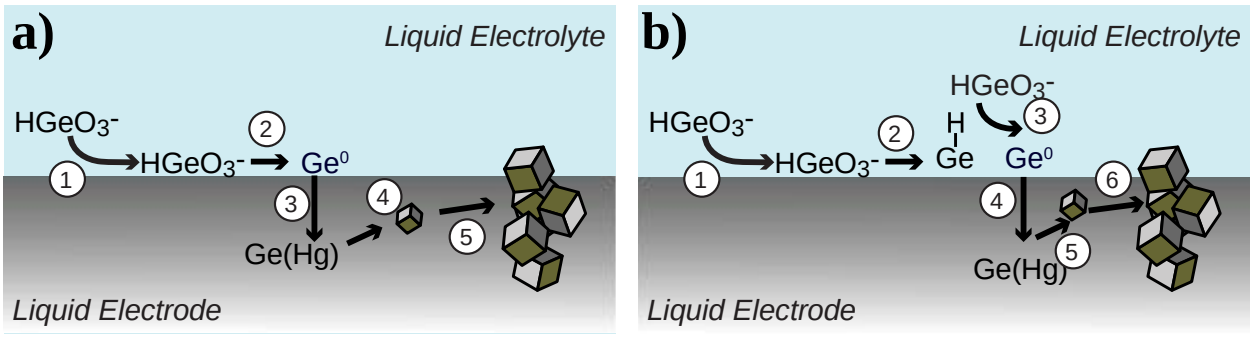

Figure 3.9. Schematic depiction of possible consequences of adsorbates on the initial steps of ec-LLS. a) Adsorption of dissolved $HGeO_3^-$ to the Hg surface before reduction to Ge^0 and dissolution into the bulk liquid metal and b) reduction of adsorbed $HGeO_3^-$ to Ge-H_n which proceeds to electrocatalyze the electroreduction of $HGeO_3^-$ to Ge^0.

3.6 References

1. Fahrenkrug, E.; Maldonado, S., Electrochemical Liquid–Liquid–Solid (ec-LLS) Crystal Growth: A Low-Temperature Strategy for Covalent Semiconductor Crystal Growth. *Accounts of Chemical Research* **2015,** *48* (7), 1881-1890.
2. Acharya, S.; Ma, L.; Maldonado, S., Critical Factors in the Growth of Hyperdoped Germanium Microwires by Electrochemical Liquid–Liquid–Solid Method. *ACS Applied Nano Materials* **2018,** *1* (10), 5553-5561.
3. DeMuth, J.; Fahrenkrug, E.; Maldonado, S., Controlling Nucleation and Crystal Growth of Ge in a Liquid Metal Solvent. *Crystal Growth & Design* **2016,** *16* (12), 7130-7138.
4. DeMuth, J.; Ma, L.; Fahrenkrug, E.; Maldonado, S., Electrochemical Liquid-Liquid-Solid Deposition of Crystalline Gallium Antimonide. *Electrochimica Acta* **2016,** *197*, 353-361.
5. DeMuth, J.; Ma, L.; Lancaster, M.; Acharya, S.; Cheek, Q.; Maldonado, S., Eutectic-Bismuth Indium as a Growth Solvent for the Electrochemical Liquid-Liquid-Solid Deposition of Germanium Microwires and Coiled Nanowires. *Crystal Growth & Design* **2018,** *18* (2), 677-685.
6. Benbow, E. M.; Dalal, N. S.; Latturner, S. E., Crystal growth and magnetic behavior of R6T13−xAlxMy phases (R=La, Nd; T=Mn, Fe; M=main group) grown from lanthanide-rich eutectic fluxes. *Journal of Solid State Chemistry* **2009,** *182* (11), 3055-3062.
7. He, H.; Tyson, C.; Saito, M.; Bobev, S., Synthesis and structural characterization of the ternary Zintl phases AE3Al2Pn4 and AE3Ga2Pn4 (AE=Ca, Sr, Ba, Eu; Pn=P, As). *Journal of Solid State Chemistry* **2012,** *188*, 59-65.
8. Stojanovic, M.; Latturner, S. E., Growth of new ternary intermetallic phases from Ca/Zn eutectic flux. *Journal of Solid State Chemistry* **2007,** *180* (3), 907-914.
9. Carim, A. I.; Collins, S. M.; Foley, J. M.; Maldonado, S., Benchtop Electrochemical Liquid–Liquid–Solid Growth of Nanostructured Crystalline Germanium. *Journal of the American Chemical Society* **2011,** *133* (34), 13292-13295.
10. Kanatzidis, M. G.; Pöttgen, R.; Jeitschko, W., The Metal Flux: A Preparative Tool for the Exploration of Intermetallic Compounds. *Angewandte Chemie International Edition* **2005,** *44* (43), 6996-7023.
11. Sebastian, C. P.; Malliakas, C. D.; Chondroudi, M.; Schellenberg, I.; Rayaprol, S.; Hoffmann, R.-D.; Pöttgen, R.; Kanatzidis, M. G., Indium Flux-Growth of Eu2AuGe3: A New Germanide with an AlB2 Superstructure. *Inorganic Chemistry* **2010,** *49* (20), 9574-9580.
12. Festersen, S.; Hrkac, S. B.; Koops, C. T.; Runge, B.; Dane, T.; Murphy, B. M.; Magnussen, O. M., X-ray reflectivity from curved liquid interfaces. *Journal of Synchrotron Radiation* **2018,** *25* (2), 432-438.
13. Tostmann, H.; DiMasi, E.; Pershan, P. S.; Ocko, B. M.; Shpyrko, O. G.; Deutsch, M., Surface structure of liquid metals and the effect of capillary waves: X-ray studies on liquid indium. *Physical Review B* **1999,** *59* (2), 783-791.
14. Magnussen, O. M.; Ocko, B. M.; Regan, M. J.; Penanen, K.; Pershan, P. S.; Deutsch, M., X-Ray Reflectivity Measurements of Surface Layering in Liquid Mercury. *Physical Review Letters* **1995,** *74* (22), 4444-4447.
15. Regan, M. J.; Kawamoto, E. H.; Lee, S.; Pershan, P. S.; Maskil, N.; Deutsch, M.; Magnussen, O. M.; Ocko, B. M.; Berman, L. E., Surface Layering in Liquid Gallium: An X-Ray Reflectivity Study. *Physical Review Letters* **1995,** *75* (13), 2498-2501.
16. Duval, J. F. L.; Bera, S.; Michot, L. J.; Daillant, J.; Belloni, L.; Konovalov, O.; Pontoni, D., X-Ray Reflectivity at Polarized Liquid-Hg--Aqueous-Electrolyte Interface: Challenging

Macroscopic Approaches for Ion-Specificity Issues. *Physical Review Letters* **2012,** *108* (20), 206102.
17. Elsen, A.; Murphy, B. M.; Ocko, B. M.; Tamam, L.; Deutsch, M.; Kuzmenko, I.; Magnussen, O. M., Surface Layering at the Mercury-Electrolyte Interface. *Physical Review Letters* **2010,** *104* (10), 105501.
18. Pershan, P. S.; Schlossman, M., *Liquid surfaces and interfaces: synchrotron x-ray methods*. Cambridge University Press: 2012.
19. Murphy, B. M.; Greve, M.; Runge, B.; Koops, C. T.; Elsen, A.; Stettner, J.; Seeck, O. H.; Magnussen, O. M., A novel X-ray diffractometer for studies of liquid-liquid interfaces. *Journal of Synchrotron Radiation* **2014,** *21* (1), 45-56.
20. James Anthony, S.; John, M. B.; Karen, K. L. In *Flat-field correction technique for digital detectors*, Proc.SPIE, 1998.
21. Murphy, B. M.; Festersen, S.; Magnussen, O. M., The Atomic scale structure of liquid metal–electrolyte interfaces. *Nanoscale* **2016,** *8* (29), 13859-13866.
22. Pershan, P. S.; Schlossman, M., *Liquid Surfaces and Interfacs: Synchrotron X-ray Methods*. Cambridge University Press: Cambridge, 2012.
23. Calderín, L.; González, L. E.; González, D. J., Ab initio molecular dynamics study of the free surface of liquid Hg. *Physical Review B* **2013,** *87* (1), 014201.
24. D'Evelyn, M. P.; Rice, S. A., A study of the liquid–vapor interface of mercury: Computer simulation results. *The Journal of Chemical Physics* **1983,** *78* (8), 5081-5095.
25. Chantler, C. T., Theoretical Form Factor, Attenuation, and Scattering Tabulation for Z=1–92 from E=1–10 eV to E=0.4–1.0 MeV. *Journal of Physical and Chemical Reference Data* **1995,** *24* (1), 71-643.
26. Elsen, A.; Festersen, S.; Runge, B.; Koops, C. T.; Ocko, B. M.; Deutsch, M.; Seeck, O. H.; Murphy, B. M.; Magnussen, O. M., In situ X-ray studies of adlayer-induced crystal nucleation at the liquid–liquid interface. *Proceedings of the National Academy of Sciences* **2013,** *110* (17), 6663.
27. Runge, B.; Festersen, S.; Koops, C. T.; Elsen, A.; Deutsch, M.; Ocko, B. M.; Seeck, O. H.; Murphy, B. M.; Magnussen, O. M., Temperature- and potential-dependent structure of the mercury-electrolyte interface. *Physical Review B* **2016,** *93* (16), 165408.
28. Stevenson, K. J.; Gao, X.; W. Hatchett, D.; White, H. S., Voltammetric measurement of anion adsorption on Ag(111). *Journal of Electroanalytical Chemistry* **1998,** *447* (1), 43-51.
29. Isac-García, J.; Dobado, J. A.; Calvo-Flores, F. G.; Martínez-García, H., Chapter 13 - Green Chemistry Experiments. In *Experimental Organic Chemistry*, Isac-García, J.; Dobado, J. A.; Calvo-Flores, F. G.; Martínez-García, H., Eds. Academic Press: 2016; pp 417-484.
30. Pourbaix, M., *Atlas of electrochemical equilibria in aqueous solutions*. 2d English ed.; National Association of Corrosion Engineers: Houston, Tex., 1974; p 644 p.
31. Liang, X.; Kim, Y.-G.; Gebergziabiher, D. K.; Stickney, J. L., Aqueous Electrodeposition of Ge Monolayers. *Langmuir* **2010,** *26* (4), 2877-2884.
32. Carim, A. I.; Gu, J.; Maldonado, S., Overlayer Surface-Enhanced Raman Spectroscopy for Studying the Electrodeposition and Interfacial Chemistry of Ultrathin Ge on a Nanostructured Support. *ACS Nano* **2011,** *5* (3), 1818-1830.
33. Carolan, D.; Doyle, H., Size Controlled Synthesis of Germanium Nanocrystals: Effect of Ge Precursor and Hydride Reducing Agent. *Journal of Nanomaterials* **2015,** *2015*, 506056.

CHAPTER 4

X-Ray Reflectivity Studies of Crystalline Ge Electrodeposition via ec-LLS

4.1 Introduction

A relatively new method for the synthesis of inorganic covalent semiconductor material is the electrochemical liquid-liquid-solid (ec-LLS) growth process.[1-3] The ec-LLS process has strong parallels to other semiconductor crystal growth strategies such as solution-liquid-solid (SLS) and vapor-liquid-solid (VLS). Similar to SLS and VLS, liquid metal serves as a growth solvent for the semiconductor solute. However, since ec-LLS is an electrochemical technique, the driving force for introducing the solute into the liquid metal is the application of charge/current to reduce the oxidized semiconductor precursor. Accordingly, the reaction rate for presenting the solute to the liquid metal is sensitive to more than just temperature and pressure. Namely, carefully chosen applied currents/potentials in ec-LLS allows for the growth of crystalline semiconductor material under mild operating condition ($T < 100^{o}$ C and $P = 1$ atm).[3-7] Furthermore, the passage of current is measurable with great accuracy even in small magnitudes,[8-10] allowing for correlations to easily be made between the formation of growing material and the measured current.

Our lab has investigated several facets of the ec-LLS process including liquid metal identity, liquid metal thickness, liquid metal pattern geometry, electrolyte composition, temperature, and the applied potential.[2-6, 11] However, one quality of liquid metals that has not been directly assessed for its relevance in ec-LLS is the surface structure of the liquid metal. Unlike "conventional" liquids (e.g. water) which exhibit no long-range molecular order, liquid metals have periodic atomic structure at interfaces with substantively different materials (e.g. air and water).[12-16] The atomic ordering at the interface of a liquid metal is a result of the abrupt termination of columbic interactions between metal atoms throughout the bulk. The energetic difference in the local coordination environment of the outermost liquid metal atoms relative to that of the underlying

bulk metal atoms is substantial but can be lowered if the surface atoms stratify. Such ordering necessarily lowers the entropy of the liquid metal but this penalty is more than offset by decreased in energy between the layered top-most atoms and the underlying 'bulk' atoms. This atomic layering can persist into the bulk liquid metal at distances of ~5-7 atomic radii from the interface.

As discussed in Chapter 3, X-Ray Reflectivity (XRR) is a powerful, surface-sensitive technique that is suited for probing interfaces on the atomic scale.[17-19] With respect to atomic layering in liquid metals, XRR was the first method to unambiguously establish this curious phenomenon.[13] Previously, we established that there is evidence that persistent $HGeO_3^-$ adsorbates are present at Hg electrodes prior to initiating ec-LLS.

The work presented here continues the XRR analysis of Ge ec-LLS at a Hg electrode in aqueous electrolyte, with an emphasis now explicitly on the electrochemical reduction steps. Two key questions regarding ec-LLS are of interest here.

1) Where does crystal growth and nucleation occur in the initial stages of ec-LLS?

2) Does the surface laying of Hg have any influence over the crystal growth process in ec-LLS?

4.2 Experimental

Materials Ge(IV) oxide (99.999%, ChemPur), sodium tetraborate (99.998%, ChemPur), and Hg (99.999+%, ChemPur) were used as received. Water with a resistivity >18.2 MΩ·cm (Nanopure Barnstead Water Purification) was used throughout.

X-Ray Reflectivity Measurements The XRR experiments reported herein were conducted with a synchrotron source (λ = 0.4959 Å) at beamline P08 in PETRA III at DESY in Hamburg, Germany. To properly probe the liquid metal-liquid electrolyte interface without tilting the liquid sample, the Liquid Interface Scattering Apparatus (LISA) diffractometer was employed.[20] All measurements were conducted with a beam energy of 25 keV and with a GaAs Lambda detector (1536 x 512 array of pixels with a pixel height of 55 μm corresponding to a resolution of 3.3×10^{-4} $Å^{-1}$ in both the horizontal q_x and vertical q_z directions). Vertical and horizontal detector acceptances of 0.04° and 0.08° respectively were used throughout. The background intensity

caused by diffuse scattering was determined by setting a 0.08° horizontal offset to the detector followed by subtraction of the 0.08° horizontal and 0.04° vertical acceptance from the specular intensity. A flat-field correction was used to treat the raw data from the GaAs Lambda detector to properly account for any various in the pixel sensitivity.[21] A custom in-situ electrochemical XRR cell was utilized to house the liquid metal Hg pool and liquid electrolyte for these studies.[22] Before use, all electrolyte solutions were purged for a minimum of 30 minutes using $N_2(g)$ prior to introduction to the cell. A digital, computer controlled Ametek Modulab potentiostat and a $Hg/HgSO_4$ were used throughout.

X-Ray Reflectivity Data Analysis

In contrast to the work performed in Chapter 3 of this thesis, this work utilizes the 'first-layer' variant of the distorted crystal model[19, 23] to understand the experimental data. The principle difference between the 'first-layer' and 'Hg adlayer' models is that the 'first-layer' model modulates the first layer of the Hg surface layering whereas the 'Hg adlayer' model employs a low density Hg adlayer to the surface of the electrode. The 'first layer' model was chosen for the data analysis here to better ascertain any changes that occur in the first layer of the Hg surface, such as increases or decreases in electron density, during the nucleation and growth of crystalline Ge. Although the 'Hg Adlayer' model can accurately fit the data, it does not provide relevant information regarding the electron density in the first layer of the liquid metal where the crystal growth steps likely occur. Additionally, it is unlikely that an Hg adlayer would be present while Ge actively grows and emerges from the Hg surface.

The first-layer model is described by equation 4.1,

$$\frac{\langle\rho_e(z)\rangle}{\rho_{e,Me}} = \frac{1}{2}\frac{\rho_{e,Ge/H_2O}}{\rho_{e,Me}}\left(1-\operatorname{erf}\left(\frac{z-z_{H_2O}}{\sigma_{H_2O}\sqrt{2}}\right)\right)+\frac{d\rho_{fi}}{\rho_{e,Me}\sigma_i\sqrt{2\pi}}e^{\frac{-\left(z-z_{fi}\right)^2}{2\sigma_i^2}}+\sum_{n=1}^{\infty}\frac{d}{\sigma_n\sqrt{2\pi}}e^{\frac{-(z-nd)^2}{2\sigma_n^2}} \qquad (4.1)$$

where z_{H_2O} & σ_{H_2O} describe the position and width of the electrolyte front, ρ_{fi} is the amplitude of the first layer, d is the atomic layer spacing, z_{fi} is the position of the first layer, and σ_n is the root mean displacement of the nth layer. This term increases at depths progressively further from the interface. Finally, $\rho_{Ge/H2O}$ is the electron density of the electrodeposited Ge. In this work and as justified below, we treat the electrodeposit as a porous film of Ge where electrolyte can permeate through the entire volume all the way to the Hg interface. As detailed below, the composition of

this porous layer was determined considering the absolute intensity of XRR data at low q_z values. All background subtraction, normalization, and general fitting procedures were carried out in an identical manner to those described in Chapter 3. Here, element-specific form factors for the Ge/H_2O porous film were not used because this model does not correspond to a defined adlayer. Instead, the assumed microporous Ge film has an undefined composition which we were not attempting to detail. Therefore, a general electron density, $\rho_{Ge/H2O}$, of the composite microporous film was sufficient to describe the observed x-ray scattering.

4.3 Results

Figure 4.1 shows fitted reflectivity curves using the 'first-layer' model for a Hg electrode immersed in electrolyte containing dissolved GeO_2 biased at -1.5 V vs. $Hg/HgSO_4$. At this potential, the reduction of GeO_2 occurs, but at a rate which is too slow for any accumulation of reduced material to be observable. These curves could be described as a liquid Hg – liquid electrolyte interface with an adlayer present between the two layers. This adlayer was best described with a single Ge gaussian. It should be noted that the intensity of this gaussian is slightly higher than the gaussian used to fit the data collected at -0.9 V vs. SCE (-1.3 V vs. $Hg/HgSO_4$) in chapter 3 under otherwise identical conditions. Specifically, the gaussian used to fit the data presented here at -1.5 V exhibited an electron density increase of 0.01 with respect to the data collected at -1.3 V. Furthermore, a large increase in the intensity of the adlayer gaussian was observed compared to the XRR data collected at an equivalent potential without dissolved GeO_2. In this case, an increase of approximately 0.1 was observed following the addition of dissolved GeO_2 which provides further evidence for the formation of an adsorbate layer on the liquid Hg electrode. Electron density values reported here are unitless as they are with respect to the bulk electron density of liquid Hg (i.e. an increase of 0.1 is equivalent to 10% of the bulk electron density of Hg).

To study the growth of thick Ge films from the Hg electrode, two series of experiments were conducted which employed potentials more negative than -1.5 V. The first set of experiments focused on biasing the electrode to a sufficiently negative potential to allow for the electrodeposition of Ge for a set amount of time.

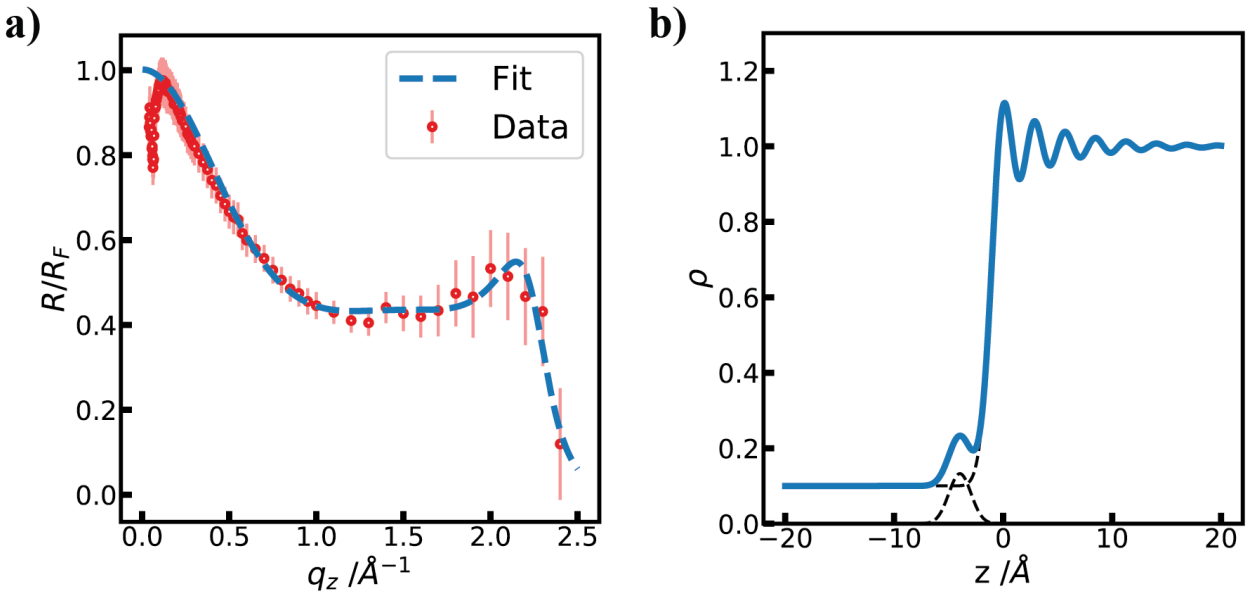

Figure 4.1 a) Fit X-ray reflectivity curve normalized to the Fresnel reflectivity for a Hg electrode immersed in deaerated electrolyte containing 0.1 M $Na_2B_4O_7$ and a formal concentration of 0.05 M GeO_2 while biased at -1.5 V vs. $Hg/HgSO_4$. b) Electron density profiles corresponding to the fitted data shown in a). To convert from $Hg/HgSO_4$ to SCE, the reference electrode used in Chapter 3 of this thesis, apply a shift of 0.396 V to potential values reported in this chapter.

Following this growth step, the potential was stepped back to and held at a more positive potential where the Hg electrode surface would be stable (i.e. neither Ge electrodeposition or Hg oxidation occurred). This tactic allowed for measurement of XRR with a static surface condition. The second set of experiments comprised measurement of XRR during the process of electrodeposition. The XRR data from the two types of experiments facilitate comparison and assessment of that result during the course of Ge crystal growth.

A proper understanding of the Ge film morphology and thickness are imperative to accurately model the interface in these studies. Figure 4.2 shows two scanning electron micrographs of a crystalline Ge film grown from a Hg working electrode under conditions identical to those investigated in this study. These micrographs reveal that the deposited Ge result in a porous structure made of a "forest" of dense Ge nanofilaments. Furthermore, Table 4.1 shows the estimated thickness of four Ge electrodepositions performed in this study. The estimated thickness reported here was calculated based on the charge passed assuming 100% Faradaic efficiency and no porosity of the Ge films. Even at the shortest deposition times performed in this study the thickness of the Ge film was on the order of hundreds of nanometers. These two observations yield useful information in regard to how to properly model the liquid metal Hg – liquid electrolyte interface in these studies.

In contrast to a simple Ge^0 adlayer, we chose to use a porous "sponge" structure on top of the liquid Hg to reflect the structure seen in Figure 4.2. That is, a microporous Ge film infiltrated with electrolyte was assumed to interpret the XRR after appreciable dissolved GeO_2 had been reduced. Accordingly, the electron density of pure water (ρ_{H2O}) was no longer operative. Instead, a value that represented the average electron density of microporous film (i.e. as determined by the volume ratios of Ge^0 and H_2O in the microporous layer) was used throughout. A schematic depiction illustrating this concept is shown in Figure 4.3.

Because the liquid metal surface is no longer in contact with just H_2O but instead compositionally complex surface layer, the initial normalization of the data merits further detail. Specifically, the critical angle defined by the X-ray absorptivity of this hybrid layer should be different than that of either water or solid Ge. The critical angle, q_c, for each raw XRR curve was first modified empirically until the intensity of the primary beam was set to 1.

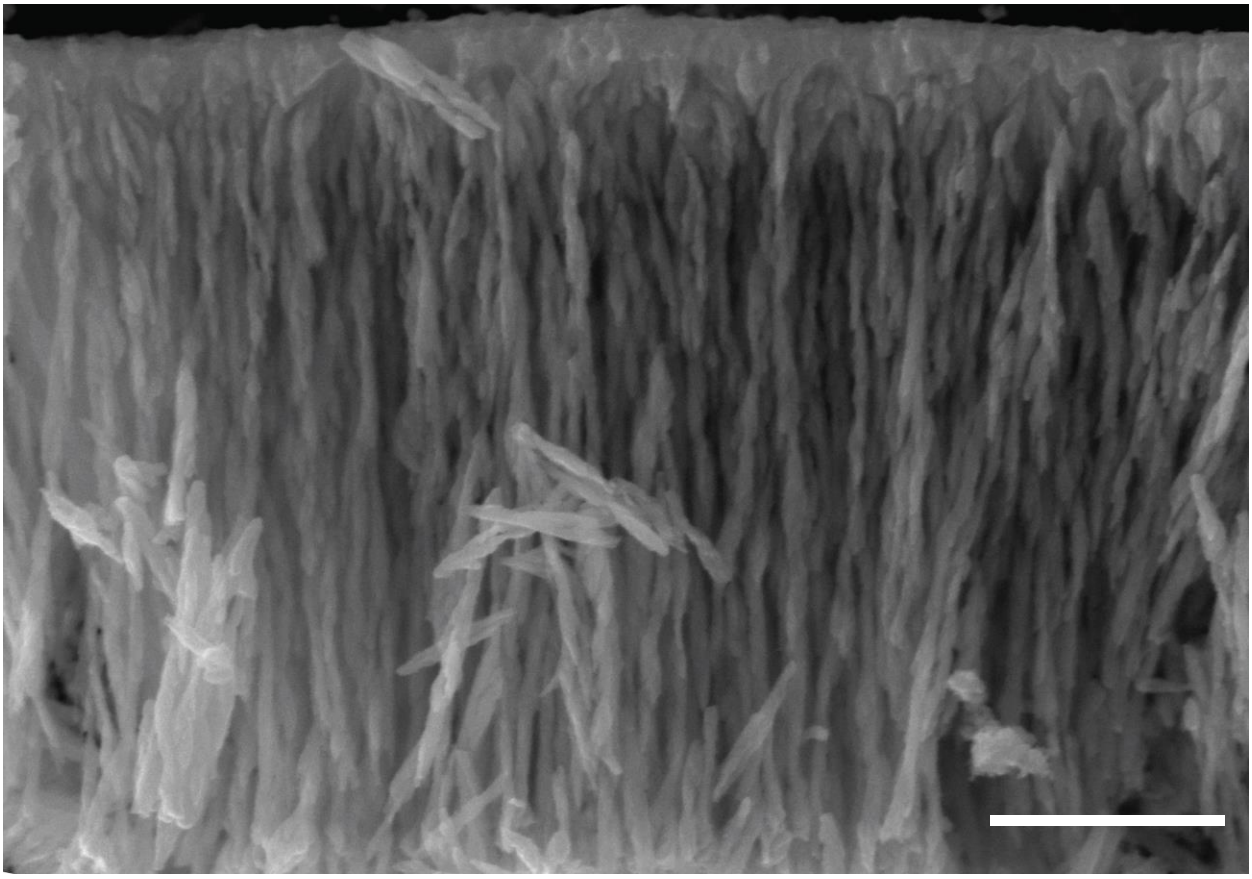

Figure 4.2 Cross section scanning electron micrograph of a polycrystalline Ge film grown by ec-LLS at a liquid metal Hg electrode. Scale bar: 1 μm.

Table 4.1. Microporous Film Thickness for Ge Grown from Hg Biased at -1.70 V

Duration /s	Charge /C	Calculated Ge Thickness /nm
60	0.1137	169
180	0.3266	486
420	0.8621	1284
600	1.2549	1869

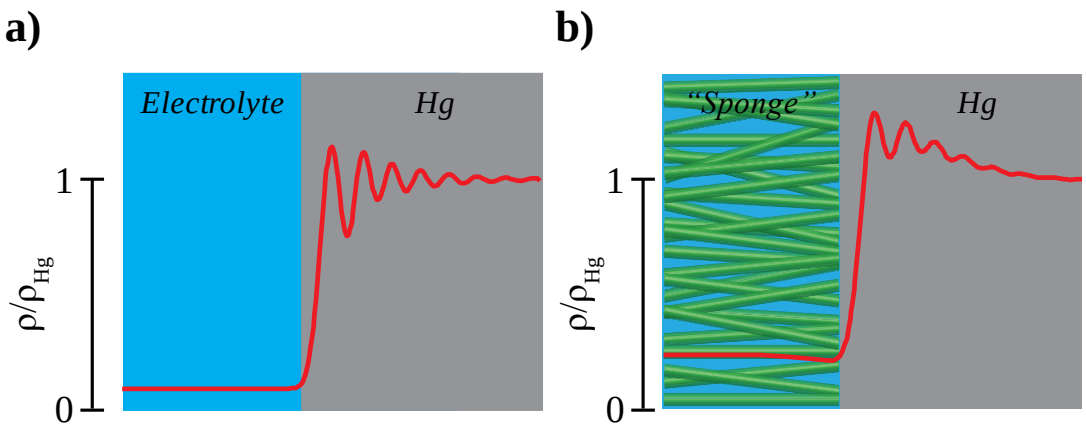

Figure 4.3 Schematic depictions of the physical structure of the liquid Hg-liquid electrolyte interface and corresponding electron density profiles for a) pristine Hg-electrolyte interface b) Hg-Ge/H_2O porous "sponge" interface.

Following this step, a specific composition of the microporous Ge/H_2O film was inferred from this value of q_c through equations 4.2 & 4.3,

$$q_c = 4\pi\sqrt{\frac{r_e}{\pi}(\rho_1 - \rho_0))} \tag{4.2}$$

$$\rho_1 = (\rho_{Ge} \cdot f_{Ge}) + (\rho_{H_2O} \cdot (1 - f_{Ge})) \tag{4.3}$$

where λ is the X-ray wavelength, r_e is the classical electron radius, ρ is the electron density of each respective layer, and f_{Ge} is the fractional composition of Ge in the microporous layer. The atomic ratio of Ge to H_2O was estimated through the value of ρ_1. The electron density of a material was calculated using equation 4.4, where δ is the real component of the complex refractive index:

$$\rho_e = \frac{2\pi}{\lambda^2 r_e}\delta \tag{4.4}$$

Figure 4.4 shows absolute and normalized X-ray reflectivity data collected during the first set of experiments along with the electron density profiles generated from these fits. Here, the electrode was first biased to -1.70 V to stimulate the growth of crystalline Ge for a predetermined amount of time before stepping the potential to -1.20 V to pause the reaction. Two notable features are apparent from the reflectivity curves and electron density profiles in Figure 4.4. First, the intensity of the layering peak in liquid Hg, while still present, was significantly diminished compared to either a pristine Hg surface or a Hg surface with an adsorbate layer such as those shown in Chapter 3.[12, 17, 19] For reference, the colored dashed lines in Figure 4.4 corresponds to an interface with a monotonic electron density profile with a roughness of 1.00 Å (i.e. no surface layering within Hg). Second, a distinct "dip" was noticed between the porous Ge/H_2O layer and the Hg interface in the electron density profiles corresponding to the best fit for each curve.

For the second set of experiments, the Hg working electrode was biased to -1.70 V *during* the x-ray reflectivity scan. In this scenario the reflectivity curve directly probes the surface of the Hg electrode as crystalline Ge growth occurs over the course of approximately 1.5 hours. Over the course of the measurement, the surface of the liquid Hg electrode changed from a lustrous silver to a muted grey color, and finally the surface appeared to be covered in a field of black precipitate. Figure 4.5 shows absolute and normalized X-ray reflectivity data collected during these experiments along with the electron density profiles generated from these fits. Table 4.2 shows the parameters corresponding to the best fit of the curves collected in both sets of experiments.

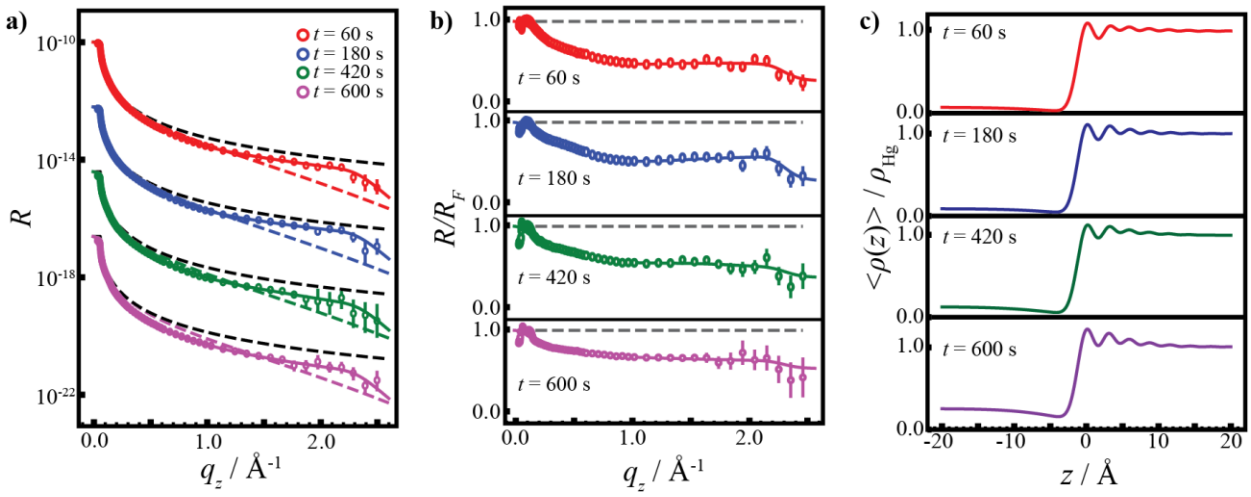

Figure 4.4 a) Plot of a) the absolute X-ray reflectivity vs. momentum transfer perpendicular to the surface and b) the same X-ray reflectivity normalized to the Fresnel reflectivity (bottom) for a Hg electrode immersed in deaerated electrolyte containing 0.1 M $Na_2B_4O_7$ and a formal concentration of 0.05 M GeO_2 at four different deposition times, t = 60 s (red symbols), 180 s (blue symbols), 420 s (green symbols), and 600 s (pink symbols). Curves are offset for clarity. Solid lines denote the corresponding best fit of the data while the dashed lines correspond to the reflectivity of an interface with a monotonic electron density profile with a roughness of 1.00 Å. c) Electron density profiles corresponding to the fitted data shown in b).

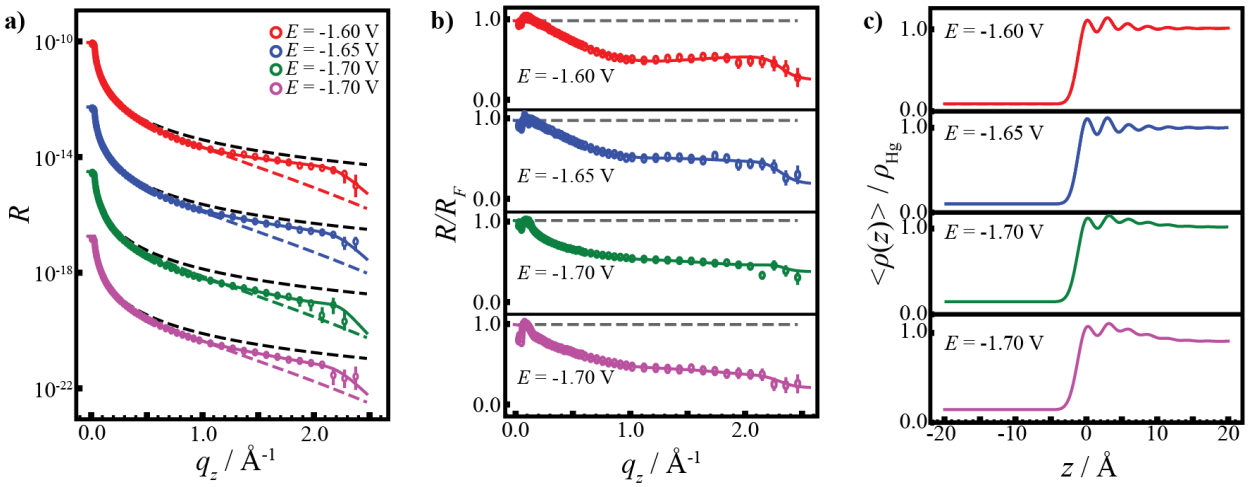

Figure 4.5 a) Plot of a) the absolute X-ray reflectivity vs. momentum transfer perpendicular to the surface and b) the same X-ray reflectivity normalized to the Fresnel reflectivity (bottom) for a Hg electrode immersed in deaerated electrolyte containing 0.1 M $Na_2B_4O_7$ and a formal concentration of 0.05 M GeO_2. Reflectivity curves were collected while the electrode was biased at at four different potentials: E = -1.6 V (red symbols), -1.65 V (blue symbols), -1.7 V (green symbols), -1.7 V (pink symbols). Curves are offset for clarity. Solid lines denote the corresponding best fit of the data while the dashed lines correspond to the reflectivity of an interface with a monotonic electron density profile with a roughness of 1.00 Å. c) Electron density profiles corresponding to the fitted data shown in b).

Table 4.2. XRR Fitting Parameters for Hg in 0.1 M $Na_2B_4O_7$ + 0.05 M GeO_2

Condition	Duration	Potential	ρ(H_2O)/ρ(Hg)	z (H_2O) /Å	σ (H_2O) /Å	σ_i /Å	σ_b /Å
Static							
	--	-1.50 V	0.10	-1.00	1.05 ± 0.01	1.05 ± 0.01	0.49 ± 0.01
	60 s @ -1.70 V	-1.20 V	0.11	-0.45	-7.77 ± 0.22	1.21 ± 0.01	0.49 ± 0.01
	180 s @ -1.70 V	-1.20 V	0.13	-0.45	-7.64 ± 0.18	1.21 ± 0.01	0.49 ± 0.01
	420 s @ -1.70 V	-1.20 V	0.20	-0.45	-7.92 ± 0.17	1.22 ± 0.01	0.50 ± 0.01
	600 s @ -1.70 V	-1.20 V	0.30	-0.45	-7.12 ± 0.17	1.22 ± 0.01	0.50 ± 0.01
Dynamic							
	--	-1.60 V	0.11 ± 0.02	4.44 ± 0.18	-1.28 ± 0.14	1.17 ± 0.01	0.50 ± 0.01
	--	-1.65 V	0.12 ± 0.02	4.21 ± 0.18	-2.53 ± 0.16	1.19 ± 0.01	0.50 ± 0.01
	--	-1.70 V	0.24 ± 0.03	4.72 ± 0.21	-6.16 ± 0.20	1.25 ± 0.01	0.50 ± 0.01
	--	-1.70 V	0.18 ± 0.02	5.26 ± 0.24	-6.64 ± 0.19	1.23 ± 0.01	0.50 ± 0.01

Table 4.2. XRR Fitting Parameters for Hg in 0.1 M $Na_2B_4O_7$ + 0.05 M GeO_2 (Cont.)

Condition	Duration	Potential	d /Å	d_{fl} /Å	ρ_{fl}/ρ (Hg)	θ (Ge Adlayer)	z (Ge Adlayer) /Å	σ (Ge Adlayer) /Å
Static								
	--	-1.50 V	2.75	3.00	1.00 ± 0.01	0.40 ± 0.03	-3.97 ± 0.18	1.05 ± 0.01
	60 s @ -1.70 V	-1.20 V	2.75	3.00	0.97 ± 0.01	--	--	--
	180 s @ -1.70 V	-1.20 V	2.75	3.00	0.98 ± 0.01	--	--	--
	420 s @ -1.70 V	-1.20 V	2.75	3.00	0.99 ± 0.01	--	--	--
	600 s @ -1.70 V	-1.20 V	2.75	3.00	1.01 ± 0.01	--	--	--
Dynamic								
	--	-1.60 V	2.75	3.00	0.96 ± 0.01	--	--	--
	--	-1.65 V	2.75	3.00	0.98 ± 0.01	--	--	--
	--	-1.70 V	2.75	3.00	0.94 ± 0.01	--	--	--
	--	-1.70 V	2.75	3.00	0.94 ± 0.01	--	--	--

The intensity of the layering peak was still much lower than observed for the pristine Hg/electrolyte interface. Additionally, the best fits for these data occurred when the microporous Ge layer was pushed slightly (~4.5 $Å^{-1}$) into the Hg surface. The fit quality was severely diminished if the microporous Ge film was forced deeper towards the bulk of the Hg in the model, indicating the Ge was only in contact with Hg right at the interface. Specifically, numerous oscillations appear for the fitted curve in the low q_z region (0-0.5 $Å^{-1}$). Lastly, the electron density of the first layer in the liquid metal Hg was lower in these dynamic measurements than the electron densities determined in the data for static XRR measurements. These points will be discussed in more detail in the following section.

4.4 Discussion

The data collected while the Hg electrode was biased at -1.5 V indicate the presence of two possible adlayers. The first option is that the single Ge gaussian present in the electron density profile simply represents an adlayer of Ge^0 on the surface of the electrode. An alternative possibility is that the Ge adlayer could be Ge-H_n. In this scenario the $HGeO_3^-$ is reduced to a hydride species onto the surface of the Hg electrode. It is worth noting that in these experiments the H atoms do not scatter x-rays strongly enough to make an impact on the reflectivity and therefore would not show up in the electron density profile.

At more negative potentials, the cumulative data speak to two main points. First, the electron density profiles for the best fits of the XRR curves collected during Ge ec-LLS suggest that the crystal nucleation and growth steps occur at the surface level of the liquid metal Hg electrode. Second, although the layering peak intensity is diminished, the ordered structure at the liquid Hg surface is still present *during* and following crystalline Ge growth via ec-LLS. The following paragraphs elaborate on these two points and their bearing on our understanding of the ec-LLS process.

A key question surrounding the growth of crystalline inorganic covalent semiconductor material via ec-LLS is whether the nucleation and growth steps occur deep into the bulk of the liquid metal or near the liquid metal-liquid electrolyte interface. For the XRR curves which were collected from a static H_2O/Ge-Hg interface the electron density profiles corresponding to the best fits show a dip in the electron density immediately before the Hg surface, implying a physical separation (Figure 4.6a). That is, the XRR data indicate the electrodeposited Ge crystals are

separated from Hg by several angstroms. Upon termination of crystal growth, Ge separates from Hg and is no longer dissolved in Hg. This likely occurs for two reasons. First, Ge is known to not readily be wet by Hg at room temperature. Second, the density of Ge is much less than Hg (5.32 vs 13.53 g cm^{-3}).[24-25] Hence, XRR is clear that there is a strong tendency for Ge to leave the Hg solvent. Upon exiting Hg and without potential control, it seems likely that the surface of the Ge crystallites oxidizes somewhat, facilitating wetting by the electrolyte.

The XRR curves collected under dynamic conditions were best fit with the porous Ge layer inserted *into* the Hg surface (Figure 4.6b). This point confirms that the nuclei and nascent crystals form within Hg, despite the minimal attraction between Hg and Ge. Ge crystallites growing inside the surface layering regime of the Hg electrode would explain the lowered electron density observed in the first layer. If the first layer of the Hg is no longer composed solely of Hg but instead Hg and Ge, the average electron density would be lowered in the first layer. This is reflected in the electron density profiles generated from the fitted data collected during crystal growth. Specifically, the first oscillation of the mercury surface layering exhibits a lower intensity for the reflectivity curves collected during Ge crystal growth compared to curves which were collected after the growth reaction had been stopped.

These collective findings are consistent with crystal growth in ec-LLS occurring inside the liquid metal working electrode, in agreement with previous studies.[1-2, 4] If the crystal nucleation and growth steps occurred at the liquid metal/liquid electrolyte interface instead, then the XRR data collected in the static vs dynamic modes ought to have been equivalent. An alternative hypothesis is that the nucleation step occurs in the bulk of the liquid Hg electrode in small clusters before floating up to the interface where the actual crystal growth step occurs. If this scenario were operative, then the crystalline Ge would be composed of numerous small crystalline grains and exhibit purely polycrystalline nature. This prediction is in fact precisely what is seen by TEM from the growth of crystalline Ge from a liquid Hg electrode via ec-LLS.[1] These two facets in conjunction with the data presented in this study strengthen the hypothesis that the crystal nucleation and growth steps in ec-LLS occur inside the liquid metal electrode.

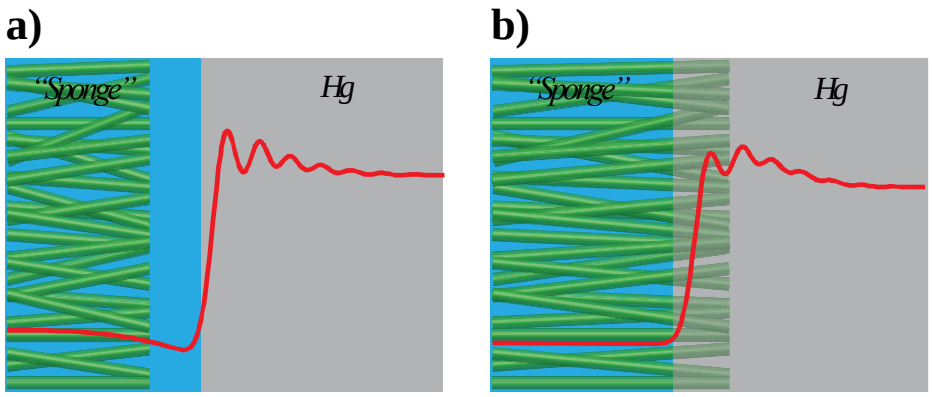

Figure 4.6 Schematic depictions of the physical structure of the liquid Hg-liquid electrolyte interface and corresponding electron density profiles for a) Hg-Ge/H_2O porous "sponge" interface with a gap between the porous germanium and Hg and b) Hg-Ge/H_2O porous "sponge" interface with the germanium nanofilaments penetrating the liquid Hg surface.

The surface ordering of the liquid metal Hg is surprisingly still partially maintained during ec-LLS. If the emergent Ge were intimately wet by Hg, the driving force for layering should be diminished. Conversely, the presence of strong Hg surface layering indicates that Ge is not solvated extensively by Hg. The extent that this point affects crystal growth is unclear but it also is expected based on the low solubility of Ge in Hg (2×10^{-7} M).[26] In some electrodeposition processes, the Hg surface layering is in fact influential on the resultant crystal morphology.[17] The data here did not support or refute this point with respect to ec-LLS. In the limited X-ray diffraction data obtained at the Hg/electrolyte interface, no preferred orientation or anisotropic crystal shape were observed for the Ge crystallites. Accordingly, we infer the persistence of Hg surface layering indicates Ge nuclei that form very close to the Hg/electrolyte interface but are not strongly wet by Hg.

4.5 Conclusions

The work presented here represents an initial fitting strategy for gauging the product from Ge ec-LLS at Hg electrodes. Further models to describe the microporous Ge films produced by ec-LLS should be considered to determine if there are further aspects that can be understood from the XRR data profiles. Still, the crude 'sponge' model used here suggests that not only do the crystal nucleation and growth steps occur in the near-surface region of the liquid metal electrode, but the Ge nucleation/crystal growth doesn't eliminate the Hg surface layering behavior. These results likely reflect the different surface energetics of liquid Hg and solid Ge. A prediction that this work makes is that the nucleation and crystal growth may show a different influence on surface layering in other liquid metal solvents if they have better wetting behavior toward Ge. One candidate liquid metal that could be used to test this point is $Hg_{1-x}In_x$, which can be both liquid at room temperature and 70 atomic % Indium. Indium is known to strongly wet Ge surfaces.[14] The data shown here provide a basis to understand how the atomic structures of the interface and of the near-surface regions of liquid metals impact ec-LLS and, more generally, all semiconductor crystal growth methods based on liquid metals.

4.6 References

1. Carim, A. I.; Collins, S. M.; Foley, J. M.; Maldonado, S., Benchtop Electrochemical Liquid–Liquid–Solid Growth of Nanostructured Crystalline Germanium. *Journal of the American Chemical Society* **2011,** *133* (34), 13292-13295.
2. DeMuth, J.; Ma, L.; Lancaster, M.; Acharya, S.; Cheek, Q.; Maldonado, S., Eutectic-Bismuth Indium as a Growth Solvent for the Electrochemical Liquid-Liquid-Solid Deposition of Germanium Microwires and Coiled Nanowires. *Crystal Growth & Design* **2018,** *18* (2), 677-685.
3. Fahrenkrug, E.; Maldonado, S., Electrochemical Liquid–Liquid–Solid (ec-LLS) Crystal Growth: A Low-Temperature Strategy for Covalent Semiconductor Crystal Growth. *Accounts of Chemical Research* **2015,** *48* (7), 1881-1890.
4. Acharya, S.; Ma, L.; Maldonado, S., Critical Factors in the Growth of Hyperdoped Germanium Microwires by Electrochemical Liquid–Liquid–Solid Method. *ACS Applied Nano Materials* **2018,** *1* (10), 5553-5561.
5. Fahrenkrug, E.; Biehl, J.; Maldonado, S., Electrochemical Liquid–Liquid–Solid Crystal Growth of Germanium Microwires on Hard and Soft Conductive Substrates at Low Temperature in Aqueous Solution. *Chemistry of Materials* **2015,** *27* (9), 3389-3396.
6. Ma, L.; Fahrenkrug, E.; Gerber, E.; Crowe, A. J.; Venable, F.; Bartlett, B. M.; Maldonado, S., High-Performance Polycrystalline Ge Microwire Film Anodes for Li Ion Batteries. *ACS Energy Letters* **2017,** *2* (1), 238-243.
7. Ma, L.; Lee, S.; DeMuth, J.; Maldonado, S., Direct electrochemical deposition of crystalline silicon nanowires at T ≥ 60 °C. *RSC Advances* **2016,** *6* (82), 78818-78825.
8. Acharya, S.; Lancaster, M.; Maldonado, S., Semiconductor Ultramicroelectrodes: Platforms for Studying Charge-Transfer Processes at Semiconductor/Liquid Interfaces. *Analytical Chemistry* **2018,** *90* (20), 12261-12269.
9. Aoki, K., Theory of ultramicroelectrodes. *Electroanalysis* **1993,** *5* (8), 627-639.
10. Zhang, T.; Fahrenkrug, E.; Maldonado, S., Electrochemical Liquid-Liquid-Solid Deposition of Ge at Hg Microdroplet Ultramicroelectrodes. *Journal of The Electrochemical Society* **2016,** *163* (9), D500-D505.
11. DeMuth, J.; Fahrenkrug, E.; Maldonado, S., Controlling Nucleation and Crystal Growth of Ge in a Liquid Metal Solvent. *Crystal Growth & Design* **2016,** *16* (12), 7130-7138.
12. Elsen, A.; Murphy, B. M.; Ocko, B. M.; Tamam, L.; Deutsch, M.; Kuzmenko, I.; Magnussen, O. M., Surface Layering at the Mercury-Electrolyte Interface. *Physical Review Letters* **2010,** *104* (10), 105501.
13. Magnussen, O. M.; Ocko, B. M.; Regan, M. J.; Penanen, K.; Pershan, P. S.; Deutsch, M., X-Ray Reflectivity Measurements of Surface Layering in Liquid Mercury. *Physical Review Letters* **1995,** *74* (22), 4444-4447.
14. Pattadar, D.; Cheek, Q.; Sartori, A.; Zhao, Y.; Giri, R. P.; Murphy, B.; Magnussen, O.; Maldonado, S., Evidence for Facilitated Surface Transport during Ge Crystal Growth by Indium in Liquid Hg–In Alloys at Room Temperature. *Crystal Growth & Design* **2021,** *21* (3), 1645-1656.
15. Regan, M. J.; Pershan, P. S.; Magnussen, O. M.; Ocko, B. M.; Deutsch, M.; Berman, L. E., Capillary-wave roughening of surface-induced layering in liquid gallium. *Physical Review B* **1996,** *54* (14), 9730-9733.
16. Tostmann, H.; DiMasi, E.; Pershan, P. S.; Ocko, B. M.; Shpyrko, O. G.; Deutsch, M., Surface structure of liquid metals and the effect of capillary waves: X-ray studies on liquid indium. *Physical Review B* **1999,** *59* (2), 783-791.
17. Elsen, A.; Festersen, S.; Runge, B.; Koops, C. T.; Ocko, B. M.; Deutsch, M.; Seeck, O. H.; Murphy, B. M.; Magnussen, O. M., In situ X-ray studies of adlayer-induced crystal nucleation at the liquid–liquid interface. *Proceedings of the National Academy of Sciences* **2013,** *110* (17), 6663.
18. Mechler, S.; Pershan, P. S.; Yahel, E.; Stoltz, S. E.; Shpyrko, O. G.; Lin, B.; Meron, M.; Sellner, S., Self-Consistent Interpretation of the 2D Structure of the Liquid

${\mathrm{Au}}_{82}{\mathrm{Si}}_{18}$ Surface: Bending Rigidity and the Debye-Waller Effect. *Physical Review Letters* **2010,** *105* (18), 186101.
19. Runge, B.; Festersen, S.; Koops, C. T.; Elsen, A.; Deutsch, M.; Ocko, B. M.; Seeck, O. H.; Murphy, B. M.; Magnussen, O. M., Temperature- and potential-dependent structure of the mercury-electrolyte interface. *Physical Review B* **2016,** *93* (16), 165408.
20. Murphy, B. M.; Greve, M.; Runge, B.; Koops, C. T.; Elsen, A.; Stettner, J.; Seeck, O. H.; Magnussen, O. M., A novel X-ray diffractometer for studies of liquid-liquid interfaces. *Journal of Synchrotron Radiation* **2014,** *21* (1), 45-56.
21. James Anthony, S.; John, M. B.; Karen, K. L. In *Flat-field correction technique for digital detectors*, Proc.SPIE, 1998.
22. Murphy, B. M.; Festersen, S.; Magnussen, O. M., The Atomic scale structure of liquid metal–electrolyte interfaces. *Nanoscale* **2016,** *8* (29), 13859-13866.
23. Calderín, L.; González, L. E.; González, D. J., Ab initio molecular dynamics study of the free surface of liquid Hg. *Physical Review B* **2013,** *87* (1), 014201.
24. Bigg, P. H., The density of mercury. *British Journal of Applied Physics* **1964,** *15* (9), 1111-1113.
25. Dismukes, J. P.; Ekstrom, L.; Paff, R. J., Lattice Parameter and Density in Germanium-Silicon Alloys1. *The Journal of Physical Chemistry* **1964,** *68* (10), 3021-3027.
26. Karpiński, Z. J.; Kublik, Z., Voltammetric and chronoamperometric investigation of germanium amalgams: Part I. Properties of the homogenous amalgam. *Journal of Electroanalytical Chemistry and Interfacial Electrochemistry* **1977,** *81* (1), 53-66.

CHAPTER 5

Resolved and Unresolved Work

5.1 Resolved Work

This thesis describes methods to study the ec-LLS process for crystalline germanium growth directly as it occurs in real time. Specifically, this work shows how *in-situ* liquid-cell transmission electron microscopy (LC-TEM) was utilized to directly study germanium nanowire growth through ec-LLS and *in-situ* electrochemical x-ray reflectivity (XRR) allowed for investigations into the liquid electrolyte/liquid metal interface at potentials commonly employed during ec-LLS. The data presented in this thesis answer the following questions: 1) What is the degree of supersaturation required for ec-LLS? 2) What is the growth rate limiting step for semiconductor nanowire growth in ec-LLS? 3) How does the micro- and nanowire growth rate influence the defect formation in ec-LLS? 4) Is there evidence for the formation of any adsorbate layers on the liquid metal electrode surface prior to the nucleation and growth of crystalline material in ec-LLS? 5) Where does crystal nucleation and growth occur in ec-LLS?

Chapter 2 detailed the first demonstration of electron-beam-initiated nanowire ec-LLS inside an environmental TEM cell. Through studies of liquid metal nanodroplets swelling during Ge^0 dissolution, the degree of germanium supersaturation required for nucleation to occur was identified to be 10^4. Additionally, the rate limiting step in the growth process was determined to be the feed rate of Ge^0 into the liquid metal bulk. Lastly, the propensity for kinks in the growing nanowire was shown to be a function of the crystal growth rate. These points provide answers to the degree of supersaturation in ec-LLS, the growth rate limiting step in ec-LLS, and a plausible method to mitigate defect formation in growing micro- and nanowires in ec-LLS.

Chapter 3 represents the first use of XRR to study changes at the liquid electrolyte/liquid metal interface during ec-LLS. In this work the liquid metal electrode was exclusively biased at

potentials positive of the $4e^-$ reduction of $HGeO_3^-$ to Ge^0 to probe the nature of the Hg/electrolyte interface in the absence of ec-LLS. This work showed the formation of a solid adlayer at more positive potentials which decays to $HGeO_3^-$ as the potential moves to more negative potentials. Ultimately, this work reveals that the liquid metal – liquid electrolyte interface is permanently changed upon the insertion of dissolved GeO_2, resulting in the formation of an adsorbate layer prior to crystal growth in ec-LLS.

Chapter 4 builds on the use of XRR to specifically monitor crystal growth *during* ec-LLS. This work demonstrated that the surface layering of liquid Hg is maintained during the growth of crystalline Ge. The XRR data are consistent with the solute (Ge) and the solvent (Hg) having minimal affinity for each other. In this case, this work establishes a necessary baseline for future XRR studies of ec-LLS where the liquid metal and solute have a stronger affinity.

5.2 Unresolved Work

5.2.1 Electrochemical Liquid Solid Solid (ec-LSS) Nanowire Growth

Two common techniques employed for the growth of semiconductor nanowires are vapor liquid solid (VLS) growth (described in Chapter 1) and vapor solid solid (VSS). VSS is based on a solid seed to initiate and to sustain crystal growth. VSS offers several advantages.[1] First, a solid metal seed can reduce the possibility of impurities in the resultant crystal. Because adatom diffusion across the surface, as opposed to diffusion through the bulk, is the primary growth path in VSS, the metal seed atoms are less likely to get trapped in the growing nanowire. Third, VSS can occur at lower temperatures as compared to VLS (e.g. 300^o C for Au in VSS vs. 600^o C for Au in VLS).[1-2] Fourth, the uniformity of the diameter of a nanowire as a function of length can be higher with a solid metal seed because volume fluctuations in the metal seed are minimal. To date, the solid crystal seed concept has not been explored in any electrochemical context.

Indium nanodroplets were shown in Chapter 2 to support e^--beam-induced ec-LLS. The growth rate vs nanodroplets size dependence suggested that appreciable growth rates could be obtained with In particles that were too small to remain molten. Specifically, indium nanoparticles with a diameter >30 nm are solid.[3] This was supported experimentally by selected area electron diffraction of indium nanoparticles larger than 30 nm (Figure 5.1). The diffraction pattern reveals multiple diffraction spots consistent with a solid and crystalline material. Therefore, any nanowires

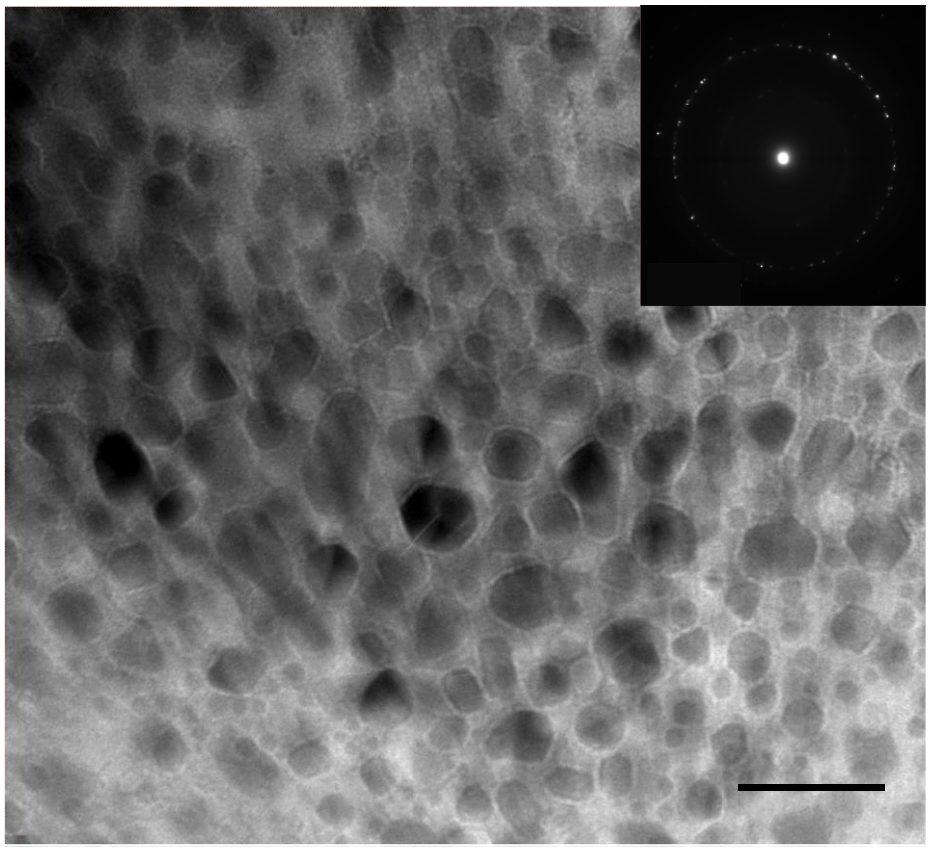

Figure 5.1 Transmission electron micrograph of In nanoparticles synthesized inside a liquid cell via electron beam irradiation of a solution containing dissolved 0.01 M $InBr_3$. Inset: Selected area electron diffraction pattern from In nanoparticles in this figure. Scale Bar: 125 nm

grown from indium nanoparticles greater than this critical diameter would be an ec-LSS growth event as opposed to an ec-LLS event.

Even with a change in physical state, the necessary requirements to carry out ec-LSS were identical to those for ec-LLS. First, the concentration ligand dissolved in the electrolyte solution was critical. If the ligand concentration was < 0.005 M, the indium nanoparticle exhibited instability under electron beam irradiation and rapidly dissolved upon imaging. Conversely, if the ligand concentration was > 0.02 M no nanowire growth events were observed. This is likely due to passivation of the nanoparticle surface blocking any Ge growth.

An example of Ge ec-LSS growth using solid indium particles is shown in Figure 5.2. This figure shows a germanium nanowire growth from a solid indium nanoparticle. The experimental set up employed to obtain this data is identical to those outlines in chapter 2 of this thesis. At 8.45 seconds, a collision between two growing nanowires from ec-LSS occurred. This observation is significant as it provides evidence of the solid nature of the indium nanoparticles. If In was liquid, indicating ec-LLS, coalescence would be expected between the In caps of the two colliding nanowires.

Several attempts were made to replicate these ec-LSS observations outside of the TEM using In and other solid metal nanoparticles including Au and Bi. In these experiments, metal nanoparticles were first electrodeposited onto a solid working electrode, typically Si or FTO. The decorated working electrode was then immersed in electrolyte containing 0.01 M $Na_2B_4O_7$ and 0.05 M GeO_2 and biased to -1.4 V vs. Ag/AgCl for 30 minutes to perform Ge electrodeposition. Following, the working electrode was imaged via scanning electron microscopy.

In nanoparticles were used first to directly emulate the results obtained from the liquid TEM work. Although this method successfully yielded Ge nanowires, in accord with our group's earlier observation[4] and a report from the Switzer group,[5] all In nanoparticles remained affixed to the silicon wafer instead of being at the front of the Ge nanowire (Figure 5.3a). This observation was interpreted to imply that In wetted the Si surface strongly. FTO was then used an alternative working electrode to remedy this point, with minimal expected affinity between In and the substrate. This substrate produced nanowires which appeared to be consistent with the general morphology for ec-LLS nanowires (i.e. the metal cap was at the top of the nanowire) (Figure 5.3b).

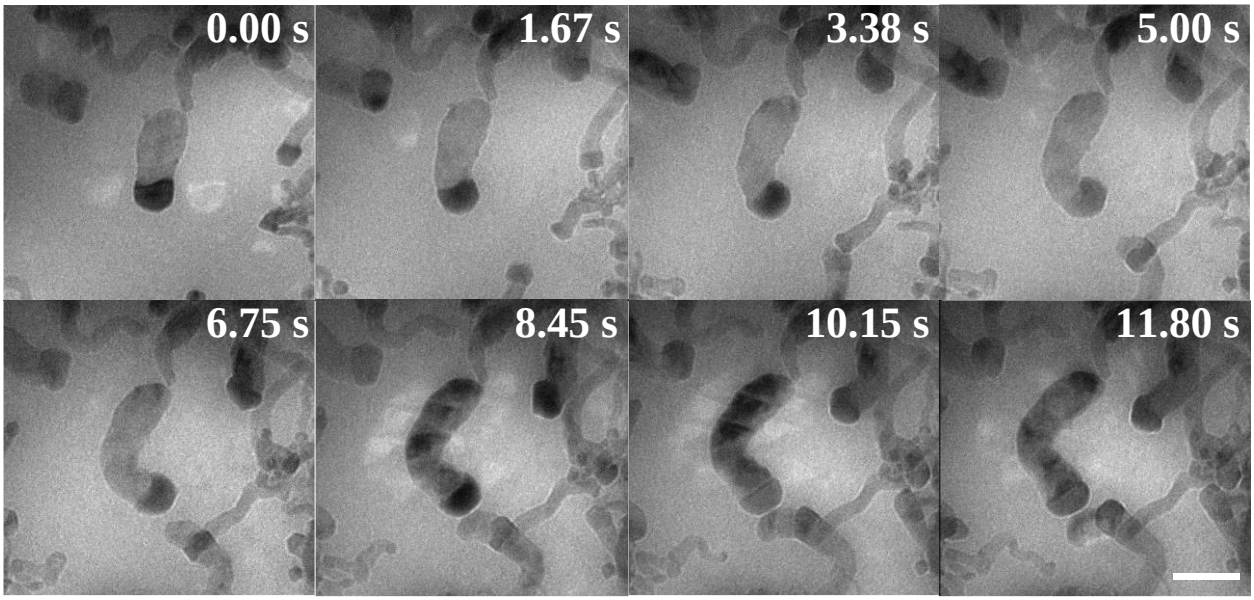

Figure 5.2 Frame grabs from a TEM video of a Ge nanowire growth event with solid In nanoparticles immersed in aqueous electrolyte containing dissolved GeO_2. Scale Bar: 100 nm

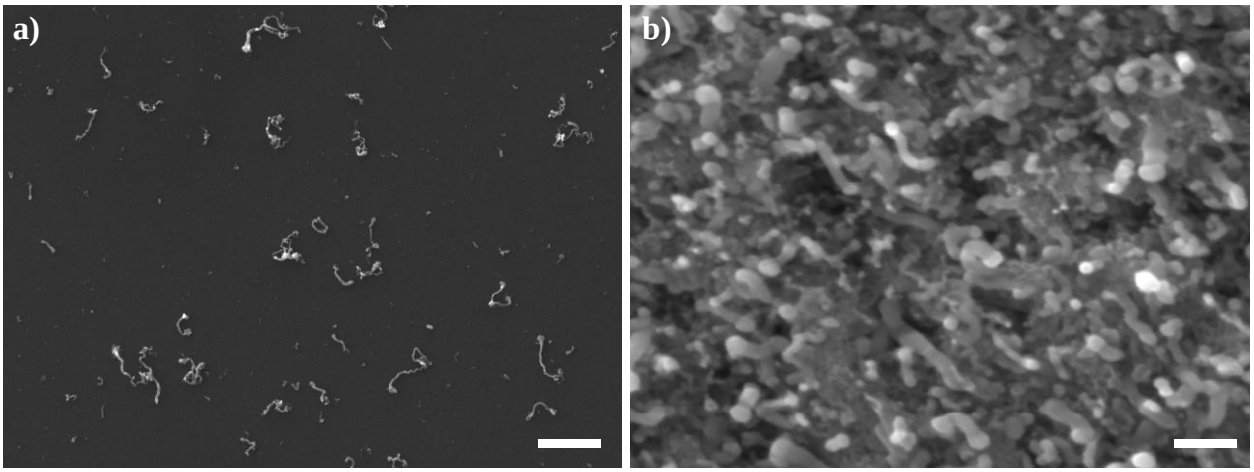

Figure 5.3 Ge nanowires grown from In via ec-LLS on a) silicon working electrode and b) FTO working electrode. Scale bars: a) 1 μm and b) 100 nm.

However, the size of the In caps were not sufficiently large to conclusively rule out an ec-LLS mechanism, i.e. the In could have been molten. Efforts to electrodeposit larger In nanoparticles with a diameter > 30 nm always resulted in a film of contiguous indium as opposed to a field of discrete nanoparticles. Although it is likely that some combination of electrodeposition parameters would favor discrete, large In nanoparticles, no methodology was identified at this time.

Ge nanowire growth by ec-LSS was separately attempted with solid Au nanoparticles. Upon attempting Ge electrodeposition with these platforms, the vast majority of Au nanoparticles detached following the electrochemical reduction of GeO_2. A control experiment was performed in which the Au nanoparticles were left to soak in the electrolyte solution employed for the electrodepositions. No loss of Au nanoparticles was observed in this experiment indicating the electrolyte itself was not particularly corrosive towards the Au nanoparticles. Similar results were observed in analogous experiments performed in the liquid TEM cell, i.e. no dissolution of Au was observed. However, after introduction and subsequent electroreduction of dissolved GeO_2, the Au nanoparticles became much more mobile. That is, initially the Au nanoparticles were affixed on the windows. However, if liquid was flowing in the liquid TEM cell, the Au nanoparticles were mostly swept out of the cell. The leading hypothesis for this observation is that the reduced Ge forms a thin coating over the Au nanoparticles, causing it to lose its adhesion to the substrate. A similar phenomenon is observed in metal induced crystallization in which a thin layer of group IV semiconductor material forms on the surface of a metal film before crystallization occurs.[6-8]

Lastly, Bi nanoparticles were tested as a possible metal nanoparticle to support ec-LSS. Curiously, these nanoparticles resulted in a film of elemental Ge as opposed to discrete nanowires. That is, electroreduction resulted in a significant quantity of elemental Ge but the form was much different than what would be expected by ec-LLS or ec-LSS. This point was sufficiently interesting that it prompted further analysis, discussed later in this chapter (Section 5.2.6). For the discussion here, the general point was that solid Bi nanoparticles also did not readily support the premise of ec-LSS.

Several pertinent questions remain about the viability of ec-LSS:

1. Do Ge nanowires grown via ec-LSS have a decreased propensity for directional changes during growth compared to ec-LLS? The work in chapter 2 of this thesis illustrated how growth rate influences the formation of kinks. Because growth of a nanowire is generally slower with a solid

cap than with a liquid cap,[9] it would be expected that ec-LSS occurs at slower growth rates than ec-LLS. This could prove to be a viable method for the mitigation of growth defects in electrochemically grown nanowires. In this context, realizing ec-LSS could be highly advantageous.

2. Do Ge nanowires grown via ec-LSS contain less metallic impurities than those grown via ec-LLS? It is known that the conductivity of the semiconductor nanowire will be dependent on the level of metallic impurities.[10] Therefore, if ec-LSS affords a greater degree of control over the metal impurity concentration, a greater tunability over the electrical properties of the nanowires might be possible.

3. How does the crystallinity of ec-LSS grown nanowires compare to those grown via ec-LLS using otherwise identical conditions? If the defect density of nanowires grown via ec-LSS is in fact lower than ec-LLS, then what dictates the defect density. In ec-LLS, the premise is the extent of supersaturation is a large factor in driving the formation of crystallographic defects. In ec-LSS, this point is not relevant.

5.2.2 Liquid Cell TEM Study of Germanium Nanowire Growth Using ec-LLS Under Direct Potentiostatic Control

Although using the e^- beam of the TEM to initiate nanowire growth is facile and convenient, it comes at the cost of full control over the growth process. The original version of the experiment where the liquid metal was 'wired' to an electrode so that an applied potential can be used to drive ec-LLS was never adequately performed. There is no fundamental reason preventing this experiment and it can be readily done with the existing equipment.

To do this type of in-situ ec-LLS experiment, several points should be considered. First, metal nanodroplets can be electrochemically deposited onto the working electrode integrated into the top chip of the liquid cell. Figure 5.4 shows this for Au nanoparticles which were selectively deposited onto the working electrode of the liquid cell. A solution of 0.01 M $HAuCl_4$ and 0.1M KCl was injected into the liquid cell containing Pt electrodes. A potential of -1.00 V was then applied for 5-10 seconds to electrochemically deposit the Au nanoparticles.

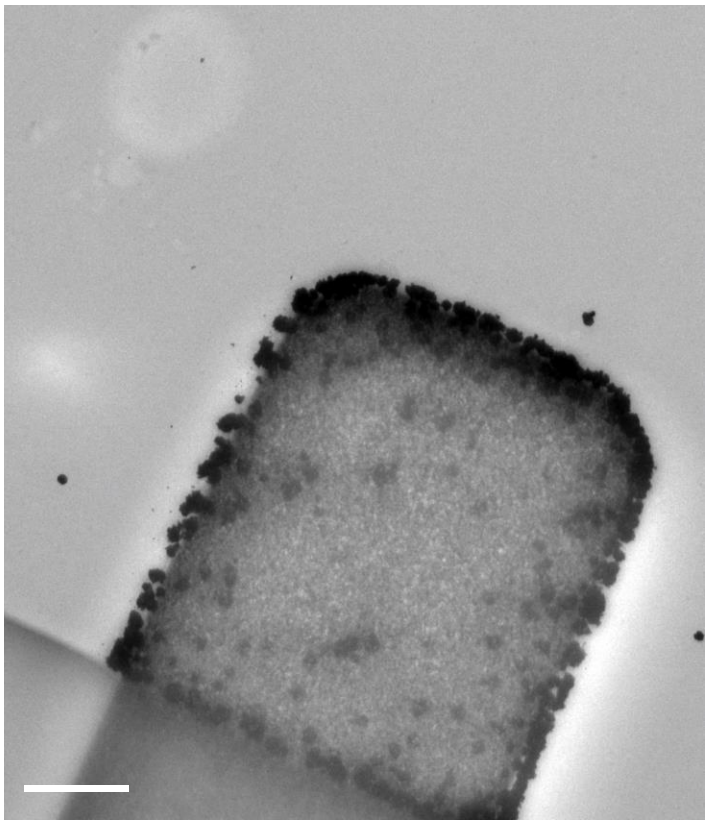

Figure 5.4 Transmission electron micrograph showing Au nanoparticles electrodeposited onto the integrated Pt working electrode in the liquid TEM cell. Scale bar: 2.5 μm.

Because nanowire growth would now be dictated by the applied bias of an external potentiostat as opposed to the concentration of solvated electrons in the viewing area, this method allows for greater clarity in studying the nanowire growth process. Previously, a large concentration of metal nanoparticles was required to facilitate the production of solvated electrons necessary for the reduction of dissolved GeO_2 (Chapter 2). This high spatial density of material cause many of the nanowire growths to overlap and become obscured. Thus, a less cluttered viewing area could prove useful in better analyzing the growing nanowires, particularly through automated means. Second, in addition to ec-LLS by a simple potential step waveform, a repeating, pulsed waveform could also be explored. This point is interesting as it could allow for better control over the degree of Ge supersaturation in the liquid metal nanoparticles. In such experiments a potential would be applied to initiate the reduction of dissolved GeO_2 for a short time (microseconds to milliseconds) before stepping to a potential where no electrochemical processes occur to allow the system to rest. These steps are repeated rapidly until the nanowire has reached the desired length.

The idea is that if the flux of Ge^0 into the liquid metal is pulsed into the liquid metal, the concentration of Ge in the liquid metal at any point in time is just enough to promote crystal nucleation to keep supersaturation to a minimum. This aspect could be another route to increase our control over the growth of crystalline material in ec-LLS. Third, the dose rate for imaging can be significantly lowered, eliminating complications from radiolytic processes caused by the beam on the electrolyte[11] and increasing the stability of the metal nanodroplets in the absence of any surface ligand.

Using an external potentiostat for LC-TEM, several precautions must be taken. A previous student (Dr. E Fahrenkrug) fully described the propensity for ground loops and other measurement artifacts, indicating the design of the employed potentiostat must be compatible with this type of experiment.[12] Specifically, a potentiostat where the working electrode is floating rather than grounded appears necessary.

5.2.3 X-Ray Reflectivity Studies of HgIn Surface Structure

A primary target for ec-LLS studies is to increase our understanding of how solvent choice affects the crystal growth process.[10, 13-14] Liquid metal alloys are an attractive growth solvent as

they are a natural choice for the growth of inorganic crystalline material.[15-17] Of particular interest for ec-LLS studies are Hg containing alloys. Hg alloys are attractive due to their low melting point, facilitating their use in aqueous solvents. Recent work by our group detailed the compositional effects of Hg_xIn_{1-x} alloys on the morphology of crystalline germanium grown via ec-LLS.[14] We found that In atoms near the surface of the liquid metal alloy enhance the mobility of germanium adatoms; altering the morphology of the grown crystalline material. Therefore, a study of structural and compositional changes at the surface of a bimetallic alloy would be beneficial to better understand solvent selection for ec-LLS.

The work detailed here focuses on a $Hg_{0.3}In_{0.7}$ alloy immersed in 0.1 M $Na_2B_4O_7$. The alloy was able to easily be prepared through the dissolution of In pellets into a pool of liquid Hg via vigorous stirring. The experimental set up and methods employed to collect the data are identical to those presented in Chapters 3 and 4 of this thesis utilizing the LISA diffractometer and synchrotron source at DESY PETRA III.

Figure 5.5 shows fitted XRR curves for both a pure Hg working electron and a $Hg_{0.3}In_{0.7}$ alloy. One obvious distinction between the two liquid metals is that the intensity of the layering peak for the $Hg_{0.3}In_{0.7}$ alloy is approximately five time greater than observed in pure mercury. From the fitting parameters, this seems to be due to a significantly lower capillary wave surface roughness in the $Hg_{0.3}In_{0.7}$ alloy compared to pure Hg. Furthermore, despite the relatively high fractional composition of In in the bulk alloy, the top atomic layer of the alloy appeared to be composed solely of Hg. This point is consistent with the thermodynamic expectation based on the surface tension of the constituent metals[18] but confirms that it only holds at the outermost surface layer. Below that layer, the composition of the liquid metal appears to be the same as the bulk, i.e. there is not a long compositional gradient.

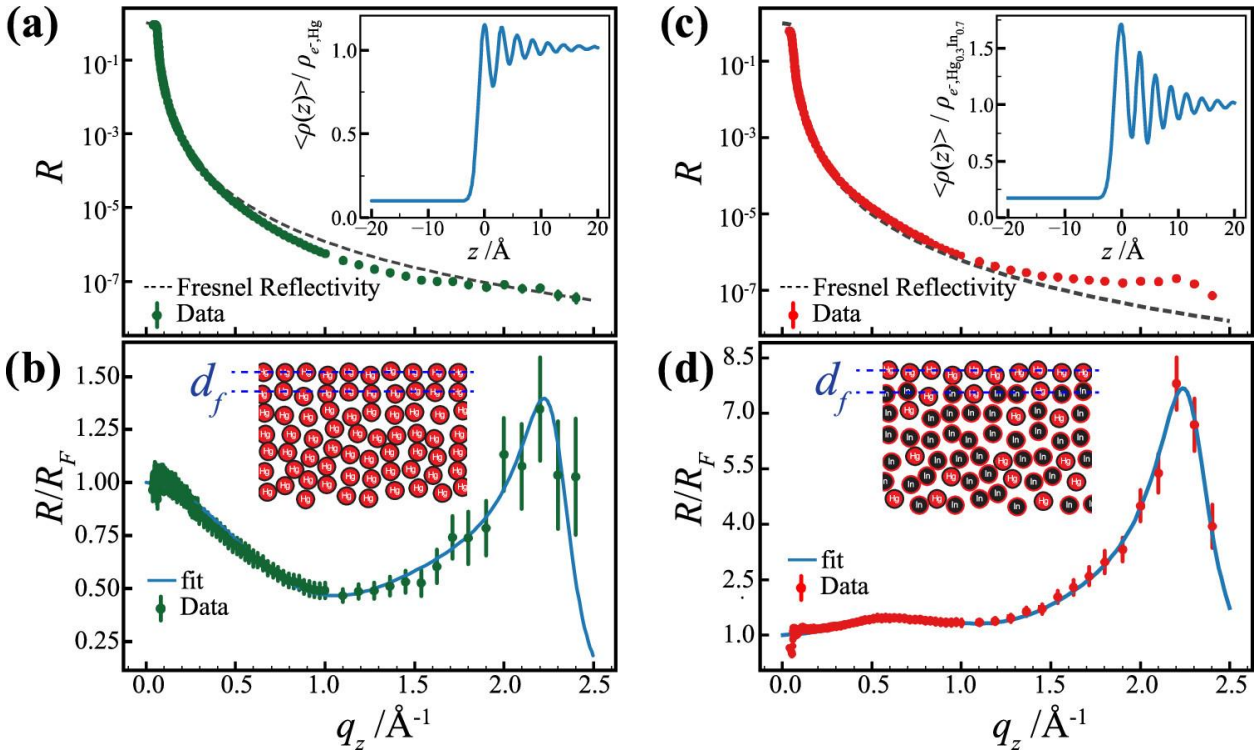

Figure 5.5 (a) Measured and (b) RF-normalized X-ray reflectivity of (a, b) liquid Hg and (c, d) liquid $Hg_{0.3}In_{0.7}$ in 0.1 M $Na_2B_4O_7$ at a potential of −1.4 V. The dashed lines in (a, c) indicate the Fresnel reflectivity, and the solid lines in (b, d) indicate the best fit by the model described in the text. The insets in (a) and (c) are the real-space profiles of the total electron density along the surface-normal vector, while those in (b) and (d) are schematic presentations of the interface structure for each liquid metal. Figure adapted from reference 10.

Previous work presented in Chapter 3 provide evidence for the innocent nature of this electrolyte (i.e. the electrolyte maintains a pristine Hg-electrolyte interface without any adsorbate layer). Therefore, any changes to the structure of composition of the surface in this alloy should strictly be the result of a change in the applied potential and not the formation of an adsorbate layer. A spike in the reflected x-ray intensity was observed at q_z = 0.08 $Å^{-1}$ when the applied potential was more positive than -1.7 V vs. $Hg/HgSO_4$ (Figure 5.6). Upon visualizing the x-ray intensity on the 2D-detector image potentials more positive than -1.7 V, two specular beams were observed. This splitting of the specular reflectance caused the observed intensity spike (Figure 5.7). This observation could be explained by two critical angles for the incident X-ray beam, i.e. each metal (the surface layer and the bulk) resulted in two separate reflections at shallow angles. This point needs further development to confirm or refute. Nevertheless, this observation does not appear to be the result of just a non-flat, i.e. rounded, interface. This point was initially suspected as the source of this artifact and earlier observations indicated this liquid metal was less flat than pure Hg. However, repetitions of the experiment indicated this was a reproducible occurrence.

The electrochemical data also exhibited potential dependent anomalies which were influenced by sample history. Figure 5.8 shows a plot of the measured current-time transients when the $Hg_{0.3}In_{0.7}$ electrode was biased at different potential employed in the study. The primary observations are as follow. First, the magnitude of the current noise increased at more negative potentials. Second, current spikes were observed in regular intervals which corresponded to a bubble detaching from the surface of Hg and a deformation in shape. The propensity for these current spikes greatly increased at more negative potentials. Third, the current magnitudes between E = -1.75 V to -1.55 V were larger when the potential was stepped more positive after reaching the most negative potentials. These anomalies would imply a potential dependent change in the surface composition of the alloy. Given that the morphology of crystalline inorganic material grown via ec-LLS is dependent on the liquid metal alloy composition, the applied growth potential may have more influence than previously thought.

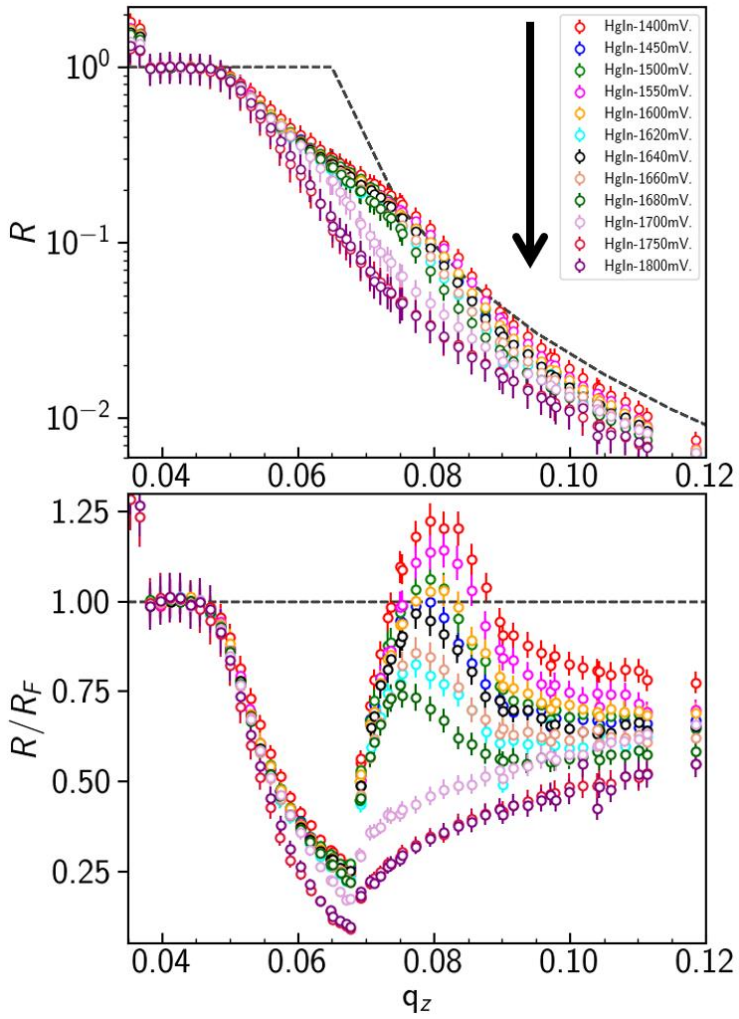

Figure 5.6 Plot of the absolute X-ray reflectivity vs. momentum transfer perpendicular to the surface (top) and the same X-ray reflectivity normalized to the Fresnel reflectivity (bottom) for a $Hg_{0.3}In_{0.7}$ electrode immersed in deaerated 0.1 M $Na_2B_4O_7$. Listed potentials are referenced to a $Hg/HgSO_4$ reference electrode.

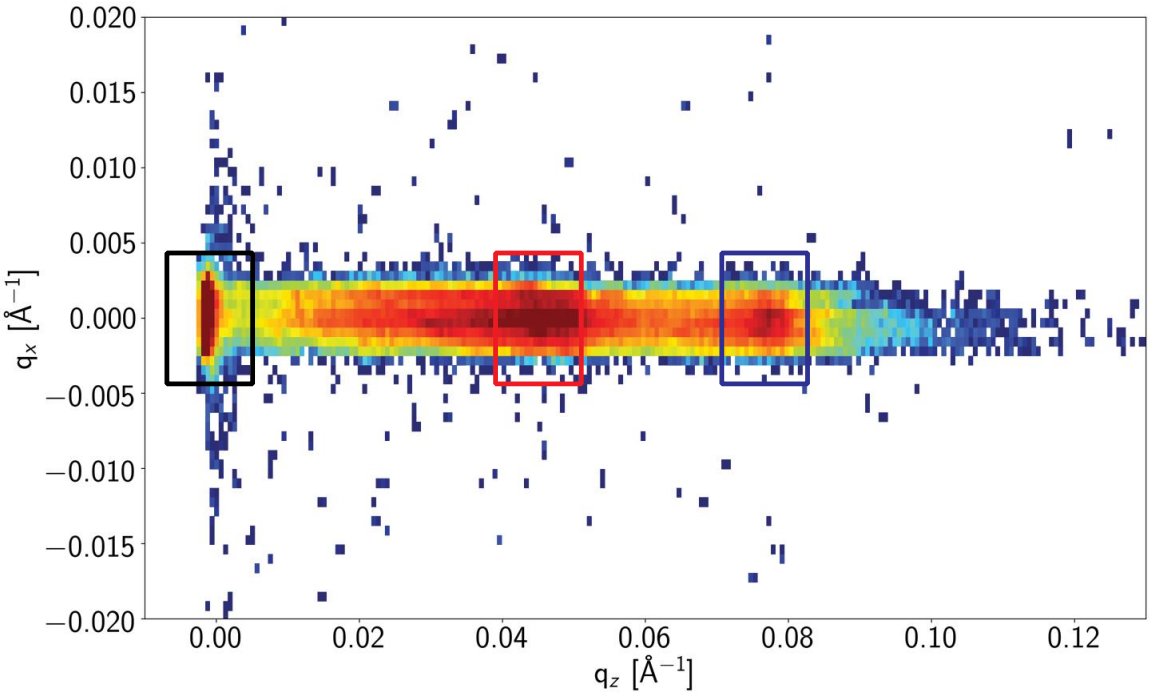

Figure 5.7 2D Detector image of the collected x-ray intensity from a $Hg_{0.3}In_{0.7}$ working electrode biased at -1.4 V vs. $Hg/HgSO_4$. The colored rectangles correspond to the primary beam (black), the first specular beam (red) and the second specular beam (blue).

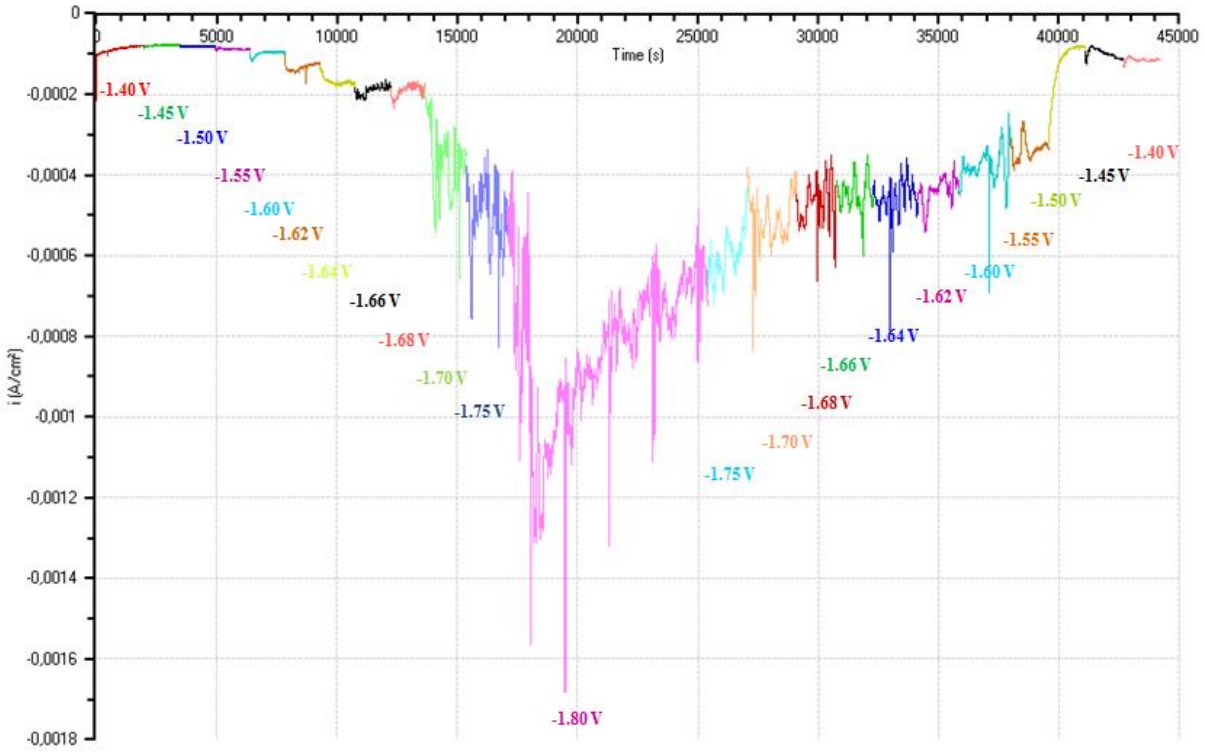

Figure 5.8 Compiled chronoamperometry plots for a $Hg_{0.3}In_{0.7}$ electrode immersed in 0.1 M $Na_2B_4O_7$ over the course of 12 hours. All potentials referenced against $Hg/HgSO_4$ and current is in IUPAC format.

5.2.4 XRR of Liquid Gallium Surfaces in Aqueous Electrolytes

Gallium (Ga) is an important metal for the preparation of both photovoltaic and semiconductor material.[19-20] Ga is also of particular interest for ec-LLS since its melting temperature is only slightly above room temperature. The interfacial chemistry of Ga in ambient conditions and immersed in water is poorly understood. Although studies have been reported on the liquid gallium-air interface which show a temperature depending layering peak centered at q_z = 2.4 Å^{-1},[21-22] there is no description of the liquid gallium-water interface. More specifically, although it is known that gallium is readily oxidized, the composition of those oxides is not clear and it is unknown whether the electrolyte type or electrode history affect the oxide structure/composition. Separately, it is not known if any condition exists where the gallium/water interface is devoid of interfacial oxides. Such conditions would be advantageous for the further development of ec-LLS processes.

The preliminary work shown here was conducted at Argonne National Lab with a beam energy of 30 keV. Despite being at a different beamline than the works in Chapter 3 and 4, the same electrochemical cell and apparatus was used. Electrochemical experiments were conducted using a Ag/AgCl references electrode. The following electrolyte compositions were explored in this study: **1)** 0.01 mM $HClO_4$ + 0.01 M Na_2SO_4 (>99%), **2)** 0.01 M NaOH (97%), **3)** 0.1 M $Na_2B_4O_7$, **4)** 0.1 M NaOH (97%) + 0.01 M Na_2SO_4 (>99%), and **5)** 0.1 M NaOH (99.99%).

The reflectivity curves collected in the $HClO_4$ solution exhibited a dip in the reflected x-ray intensity at q_z = 0.50 Å^{-1} (Figure 5.9a). This feature is indicative of the presence of a surface oxide and has previously been reported for both liquid Ga and liquid GaHg surfaces.[23] Solutions with more acidic pH were investigated but ultimately avoided in order to prevent dissolution of Ga. Similar features were also observed in the electrolyte containing dissolved $Na_2B_4O_7$. The more alkaline solutions (pH 12-13) appeared to result in an oxide free surface when the applied potential was sufficiently negative (E< -1.1 V), in agreement with the Pourbaix diagram for Ga (Figure 5.9a).[24] In particular, the previously observed intensity minimum at q_z = 0.50 Å^{-1} is significantly less prominent, which would indicate the absence of, or at least a considerably less thick, surface oxide on the Ga surface.

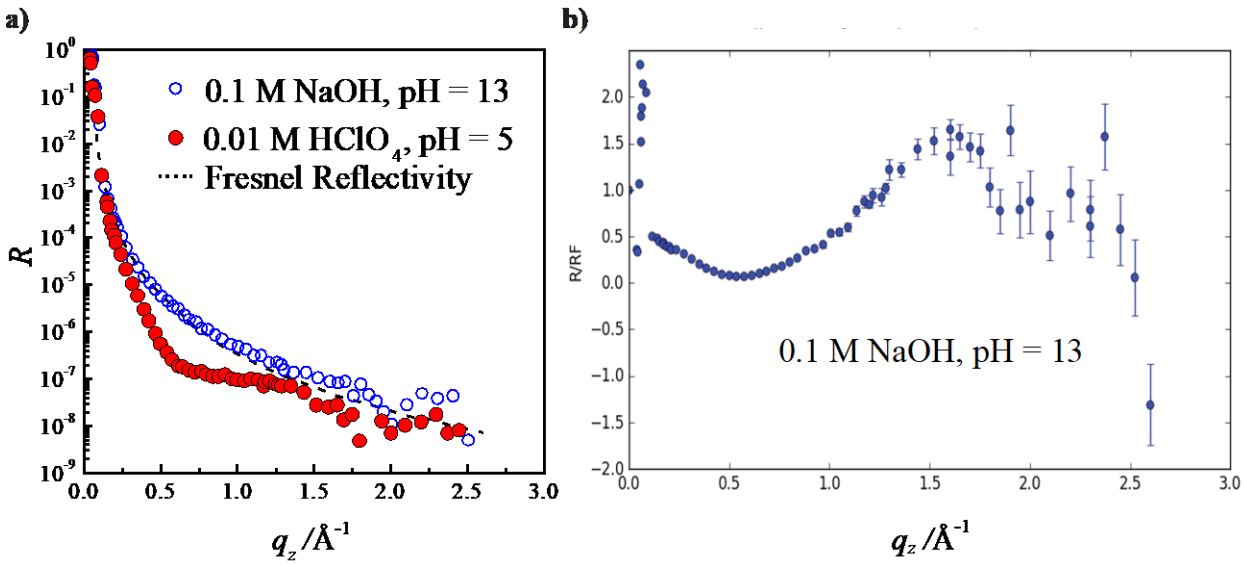

Figure 5.9 a) Plot of the absolute X-ray reflectivity vs. momentum transfer perpendicular to the surface for a liquid Ga electrode immersed in 0.1 M NaOH (hollow blue circles) or 0.01 M $HClO_4$ (solid red circles) and b) X-ray reflectivity normalized to the Fresnel reflectivity for a liquid Ga electrode immersed in 0.1 M NaOH.

Lastly, a prominent peak was observed in our studies of the liquid Ga/liquid electrolyte interface (Figure 5.9b). Curiously, this peak was centered at q_z = 1.50 Å^{-1}, significantly shifted from expected the layering peak at q_z = 2.40 Å^{-1} for liquid Ga.[21-22] Accordingly, this peak was NOT related to Ga atomic layering but could indicate some adlayer. More measurements are needed to assess this peak, since the signal to noise was poor. Although the intention of using the beamline at Argonne was to be able to take measurements with good signal to noise out to larger q_z values, we encountered technical issues that prevented such measurements. Besides sample instability, which was a prominent obstacle for some electrolytes (i.e. the surface of liquid Ga shifted over the course of data collection because electrolytes with inadequate purity levels such as 97% were used by gross negligence), there was an issue with the detector and beam tracking. Even though we could not address the technical issues in real time, using higher purity electrolytes did help to improve the stability of the Ga surface.

5.2.5 Electroless Deposition of In_2Se_3 Thin Films on Indium Foil

Although the simplest iterations of ec-LLS have the cathode serving two roles, previous group members demonstrated the possibility of a third role. The liquid metal can also serve as an active reactant, alloying with the solute to produce a binary compound. For example, the growth of III-V crystalline semiconductor materials by ec-LLS has been demonstrated.[25-26]

The premise for this work was that the exoergic ΔG_{rxn} values for the reaction between group III and group VI elements also allow for a spontaneous alloying reaction to occur, suggesting the synthesis of III-VI compounds may be possible.

Indium selenide, In_2Se_3 is a popular III-VI material[27-29] commonly used as a precursor to copper indium gallium selenide (CIGS) and copper indium selenide (CIS) photovoltaic films, UV detectors, optical windows, and memristors.[30-31] The work discussed below focuses on the spontaneous galvanic reaction between In and Se^{2-} atoms in solution for the formation of an In_2Se_3 thin film on the surface of the metal foil. Although the intent was to develop the basis for a new ec-LLS method, the resultant data argue a different synthetic pathway was operative.

To remove any barrier surface oxides, the In foil was intentionally stripped of surface oxides (In_2O_3). Surface oxides were removed by placing a drop of concentrated HCl on the surface of the In foil for 15 seconds. The foil was then vigorous washed with nanopure water to remove

any residual acid from the surface. Following this, the foil was plasma etched using argon gas for 2 minutes. The In foil exhibited a lustrous surface following these two steps. Then, the In foil was immersed in a solution containing dissolved SeO_2 with a formal concentration of 0.1 mM and the pH of the solution was adjusted with H_2SO_4 to 2. The foil was then left in the reaction solution for 48-96 hours. The resultant films were then characterized via Raman spectroscopy and scanning electron microscopy.

When the pH of the reaction solution was ≤ 2, the surface of the In foils exhibited a golden bronze hue. Raman spectra showed peaks consistent with the phonon modes for both In_2Se_3 (twin peaks at 210 cm^{-1} and 225 cm^{-1}) and Se^0 (single peak at 250 cm^{-1}, Figure 5.10).[32-33] When the pH was equal to 3, no discernible peaks were present in the Raman spectrum. Finally, when the pH was ≥ 4, the foil exhibited a maroon color and Raman spectra with peaks which were solely consistent with Se^0. To summarize, a pH ≤ 2 the deposited film is a combination of In_2Se_3 and Se^0, when the pH is equal to 3 no discernable deposition of In_2Se_3 or Se^0 was observed, and lastly at pH ≥ 4 only the accumulation of Se^0 observed on the In foil. Surface etching of the indium foil was observed at pH ≤ 2 (Figure 5.11). These data suggest that the formation of In^{3+} from acidic etching of the In foil surface occurred. Dissolved In^{3+} then served as the reactant with SeO_2. When the solution pH was more basic than 2, the solution was not acidic enough to oxidize the metal to generate In^{3+}. In this case, only Se^0 deposited on the surface of the foil.

When a combination of In_2Se_3 and Se^0 was present on the foil's surface (reaction solution pH ≤ 2), it was possible to selectively remove Se^0 from the surface of In foil without damaging the underlying In_2Se_3 layer. Specifically, if the In_2Se_3/Se^0 film is biased to -1.10 V vs. Ag/AgCl the Se^0 will be reduced to Se^{2-} leaving only the In_2Se_3 behind. Furthermore, the golden bronze film is now black in color and the Raman spectra for these films display only the peaks corresponding to the In_2Se_3 phonon modes with the Se^0 peaks being removed (Figure 5.12).

Although a facile two-step procedure for the spontaneous generation of In_2Se_3 was determined, further characterization of the films is warranted. When X-Ray Diffraction (XRD) was performed on the films only In^0 peaks were observed in the diffraction pattern. However, grazing XRD should be performed to properly assess the crystalline nature of the film itself.

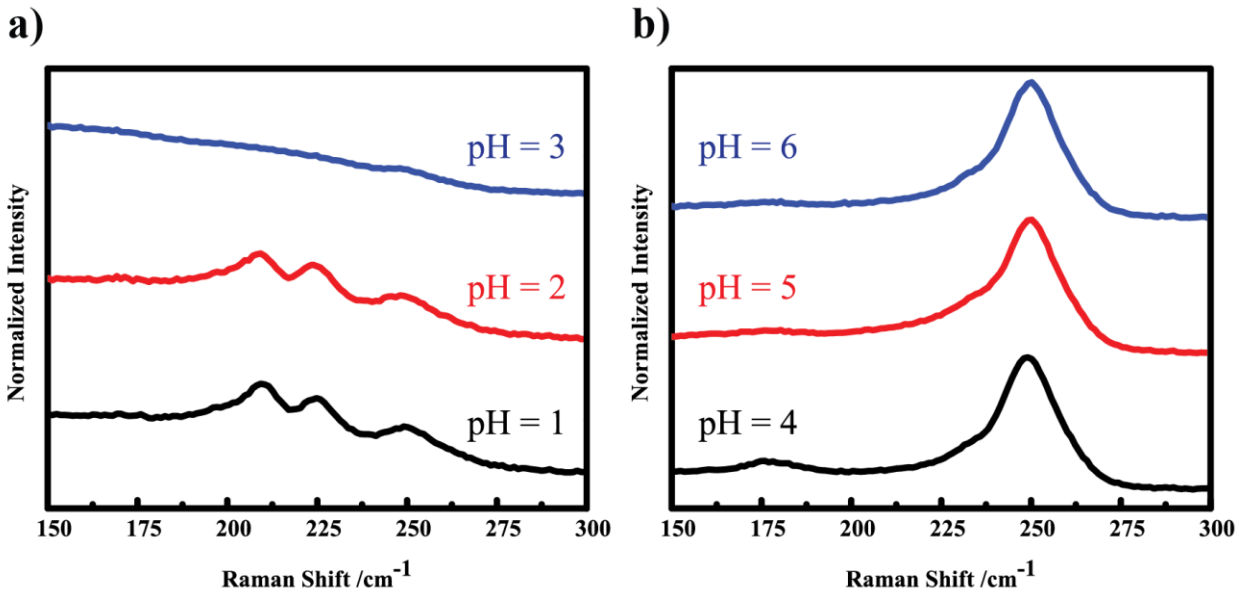

Figure 5.10 Raman spectra for Indium foil immersed in 0.1 mM SeO_2 for 72 hours at a) pH = 1 (black), 2 (red), or 3 (blue) and b) pH = 4 (black), 5 (red), or 6 (blue). The spectra have been offset for clarity.

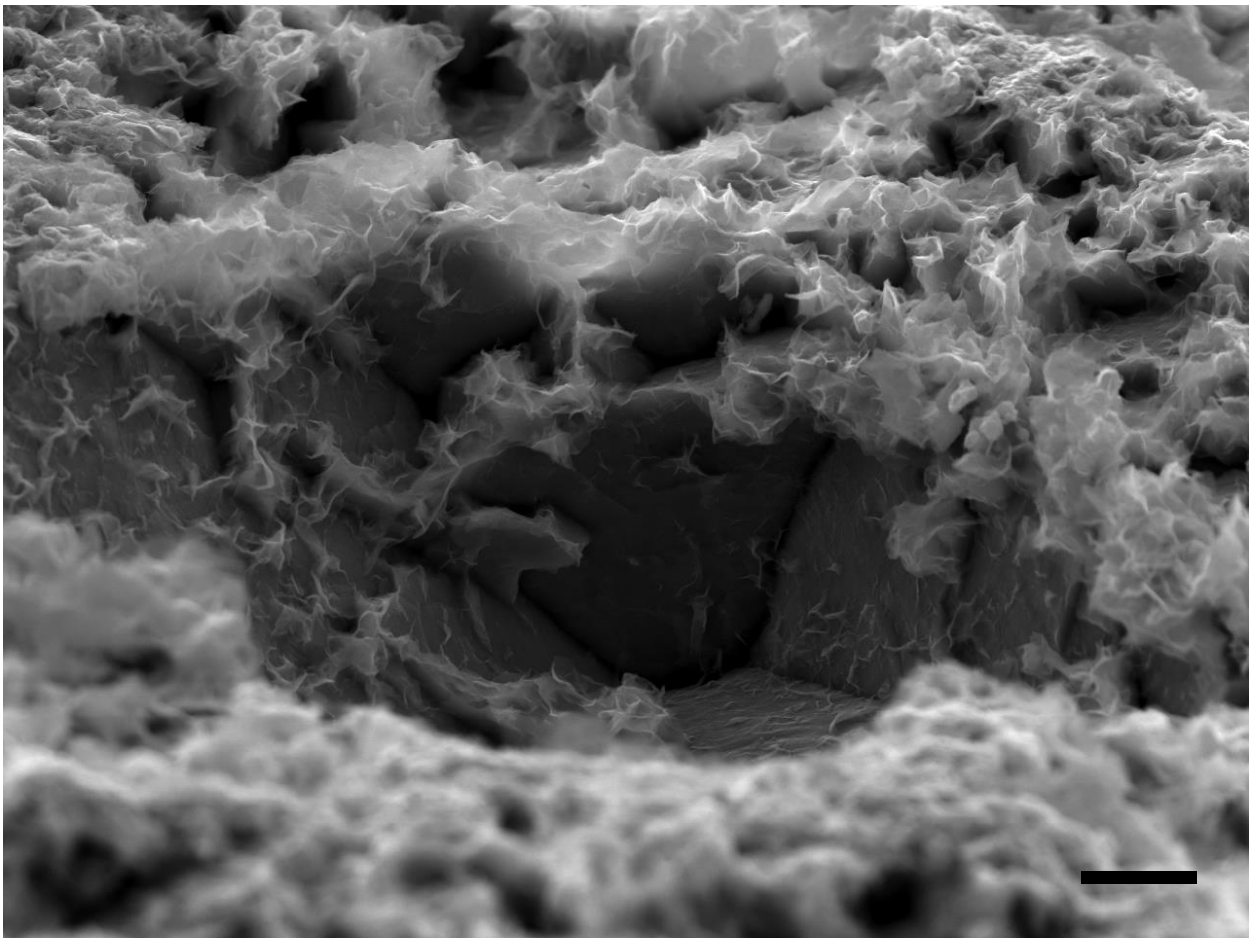

Figure 5.11 Scanning electron micrograph of etching observed on indium foil covered in an In_2Se_3 film. Scale Bar: 1 μm.

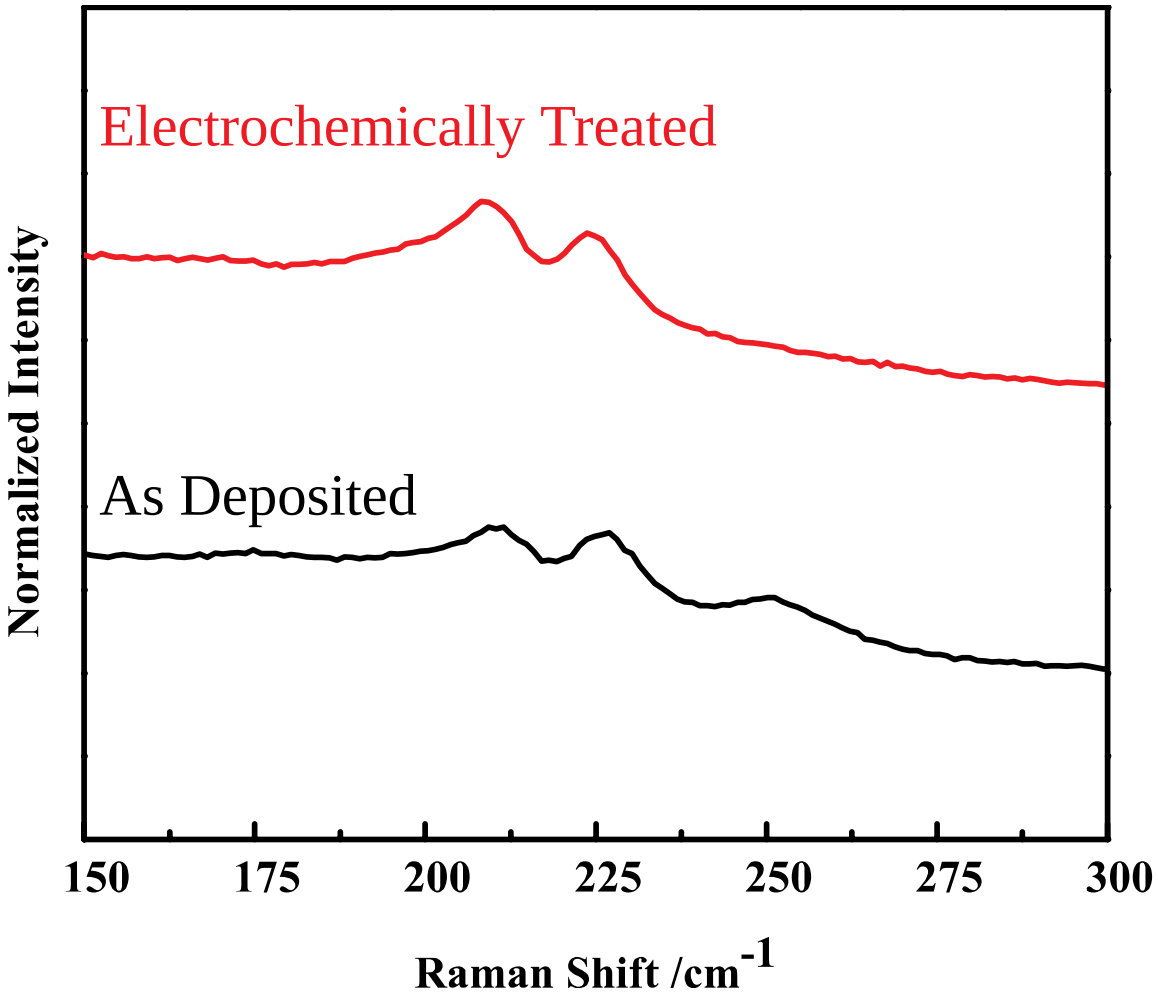

Figure 5.12 Raman spectra for Indium foil immersed in 0.1 mM SeO_2 for 72 hours either a) as deposited or b) after electrochemically stripping of amorphous Se^0 from the surface.

Second, no thorough studies were performed to assess the thickness of the In_2Se_3. A series of time-dependent growth followed by cross-sectional scanning electron microscopy would be useful in determining the growth rate of the film as well as the maximum thickness before Se^0 deposition dominates. Such measurements could be readily collected and were not by choice, preventing publication of this particular work.

5.2.6 Hydride Assisted Electroreduction of Dissolved GeO_2

The electrodeposition of group IV semiconductor onto solid metal electrodes is challenging. The cumulative data from our group and others is that only a few monolayers of material are deposited before the electrodeposition self terminates. The mechanism for why this occurs has never been reported.

In the case of Ge electrodeposition, a hypothesis was developed in our lab that the presence or involvement of surficial hydride groups facilitates electroreduction of dissolved GeO_2. The premise is based on the fact that the dominant species in solution at alkaline pH values (i.e. $HGeO_3^-$) would require removal of several Ge-O bonds. The action of a sufficiently potent hydride could catalyze such bond scissions.[34-35] One possibility on solid electrodes like Au and glassy carbon is that electroreduction of dissolved GeO_2 occurs initially but quickly coats the surface with elemental Ge, which does do not natively have surface hydride groups that facilitate the electroreduction reaction. Accordingly, in the absence of a mechanism to remove elemental Ge (and/or its surface hydrides), the electrode reaction stops.

Bismuth as an additive in ec-LLS was explored because bismuth can be reduced in water to generate $BiH_3(g)$,[36] i.e. the solid Bi is gasified and physical removed from the surface. Two primary strategies were explored for incorporating Bi into the ec-LLS process. The first approach involved the electrodeposition of Bi nanoparticles onto the working electrode surface. This was accomplished by immersing the working electrode in an electrolyte containing 0.02 M $Bi(NO_3)_3$ and 1.00 M HNO_3 follow by biasing the electrode to -0.65V vs. Ag/AgCl for 7.00 s. The electrolyte solution was then swapped out for one containing 0.01 M $Na_2B_4O_7$ and 0.05 M GeO_2. Lastly, the solution was heated to 70^o C and the electrode was biased to -1.50 V vs. Ag/AgCl for 20 minutes. The second approach utilized a one-pot synthesis technique using an electrolyte containing 0.005 M $Bi(NO_3)_3$, 0.01 M $Na_2B_4O_7$, and 0.05 M GeO_2. A lower concentration of $Bi(NO_3)_3$ needs to be used as the solubility of the compound is low in nonacidic solutions. The deposition process was

then carried out identically to the first approach. In both cases the surface of the silicon wafer in contact with the electrolyte changed to a light grey color following the deposition. Under identical conditions but in the absence of any bismuth additives, no color change was observed on the surface of the silicon working electrode.

Scanning electron microscopy, energy dispersive x-ray spectroscopy (EDS), and Raman spectroscopy analysis were performed to ascertain the morphology and chemical composition of the surface following the deposition. Figure 5.13 shows scanning electron micrographs for a silicon wafer immersed in 0.01 M $Na_2B_4O_7$ and 0.05 M GeO_2 biased to -1.50 V vs. Ag/AgCl for 20 minutes with and without bismuth additives. The solution containing bismuth revealed a rough film on the surface of the working electrode, while the solution without bismuth failed to yield any noticeable deposition. EDS analysis revealed that the film was composed primarily of germanium with some bismuth impurities (Figure 5.14a). Raman analysis corroborated these observations in that a peak at 300 cm^{-1} which is consistent with the phonon mode for elemental germanium (Figure 5.14b).[37] The broad shoulder observed in this peak is likely indicative of its amorphous nature.[38]

To better understand the fate of the bismuth nanocrystals a series of control experiments were performed. Bismuth nanocrystals were first deposited on a silicon wafer using the methods described above. Submerging these nanocrystals in a 0.01 M $Na_2B_4O_7$ solution for 8 hours resulting in no change in the crystal structure macroscopically or microscopically. When the same silicon wafer was biased to -1.5 V vs. Ag/AgCl for 20min a large amount of the nanocrystals were no longer present following the electrolysis. Figure 5.15 illustrates this point by showing a side-by-side comparison of the as-deposited bismuth nanocrystals and the same nanocrystals following the electrolysis step.

Additionally, LC-TEM experiments were carried out to observe the Bi nanoparticles in the presence of the solvated electrons and hydride ions produced in water from electron beam irradiation. An electrolyte solution containing 0.02 M $Bi(NO_3)_3$ and 1.00 M HNO_3 was injected into the liquid TEM cell and imaged using a sufficiently high dose rate to initiate the growth of Bi nanoparticles. Within 10 seconds the nanoparticles began to deteriorate and appear to bubble (Figure 5.16). This observation supports the hypothesis that the Bi nanoparticles are reduced to $BiH_3(g)$ in solution. Still, a more cogent and direct study is needed to confirm the presence of this species in the electrolyte solution during Ge deposition.

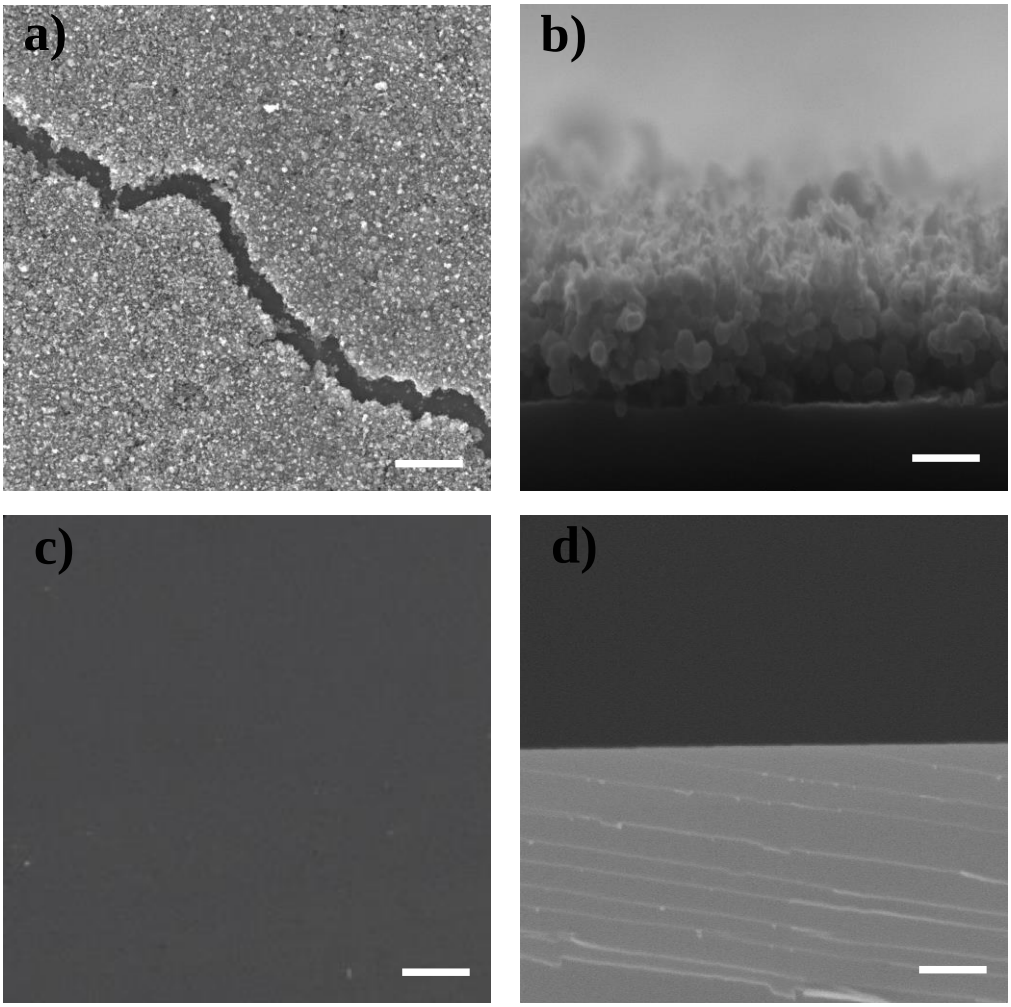

Figure 5.13 a) Top-down scanning electron micrographs of a silicon working electrode immersed in an electrolyte containing 0.01 M $Na_2B_4O_7$ and 0.05 M GeO_2 biased at -1.50 V for 20 minutes with bismuth nanocrystals present on the surface. b) Cross sectional scanning electron micrograph of the sample from a). c) Top-down scanning electron micrographs of a silicon working electrode under the same experimental conditions as (a) without bismuth nanocrystals present on the surface. d) Cross sectional scanning electron micrograph of the sample from c). Scale Bars: a) 2 μm, b) 100 nm, c) 2 μm, d) 200 nm

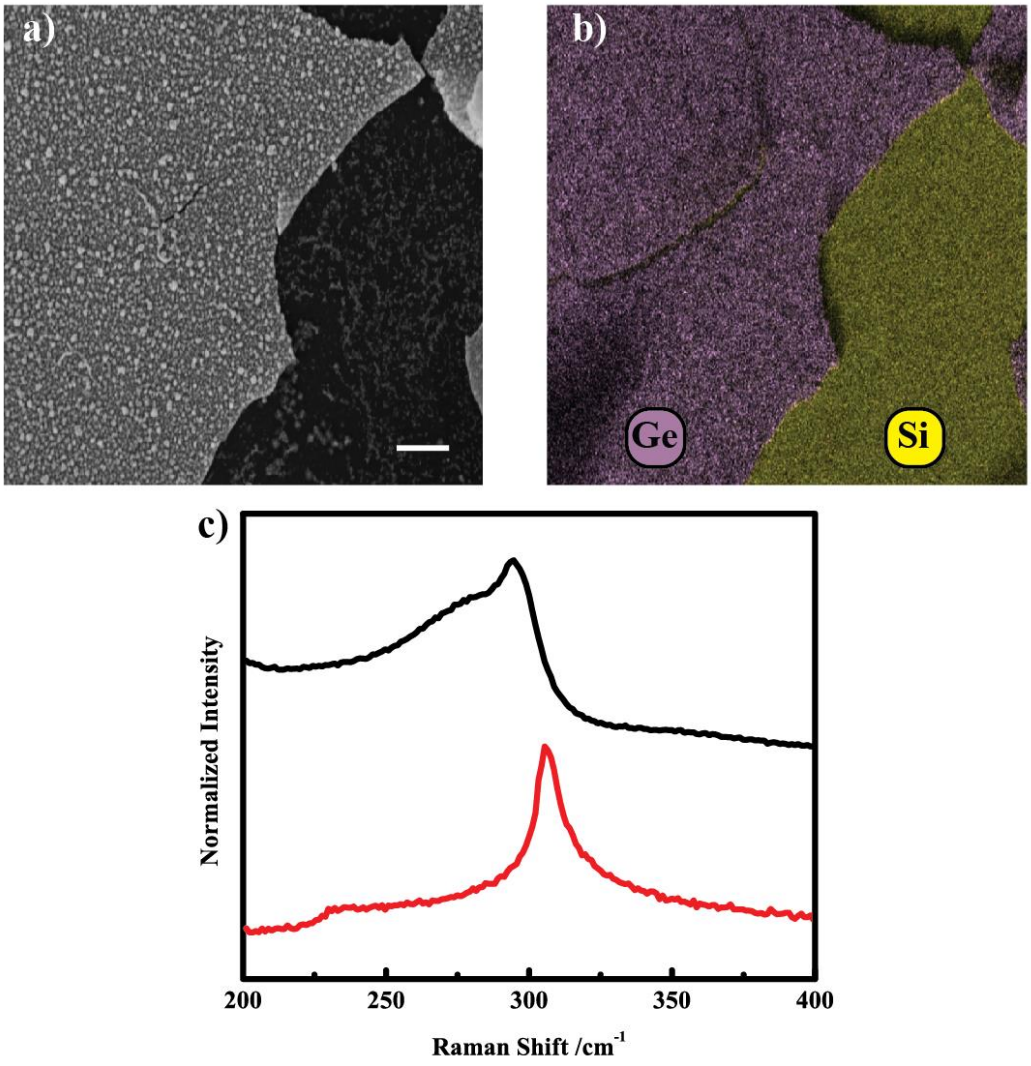

Figure 5.14 a) Top-down scanning electron micrographs of a silicon working electrode immersed in an electrolyte containing 0.01 M $Na_2B_4O_7$ and 0.05 M GeO_2 biased at -1.50 V for 20 minutes with bismuth nanocrystals present on the surface. b) EDS elemental map of the sample area shown in a) c) Raman spectra for the film shown in a) (black) and the silicon substrate (red). Scale Bar: 5 μm

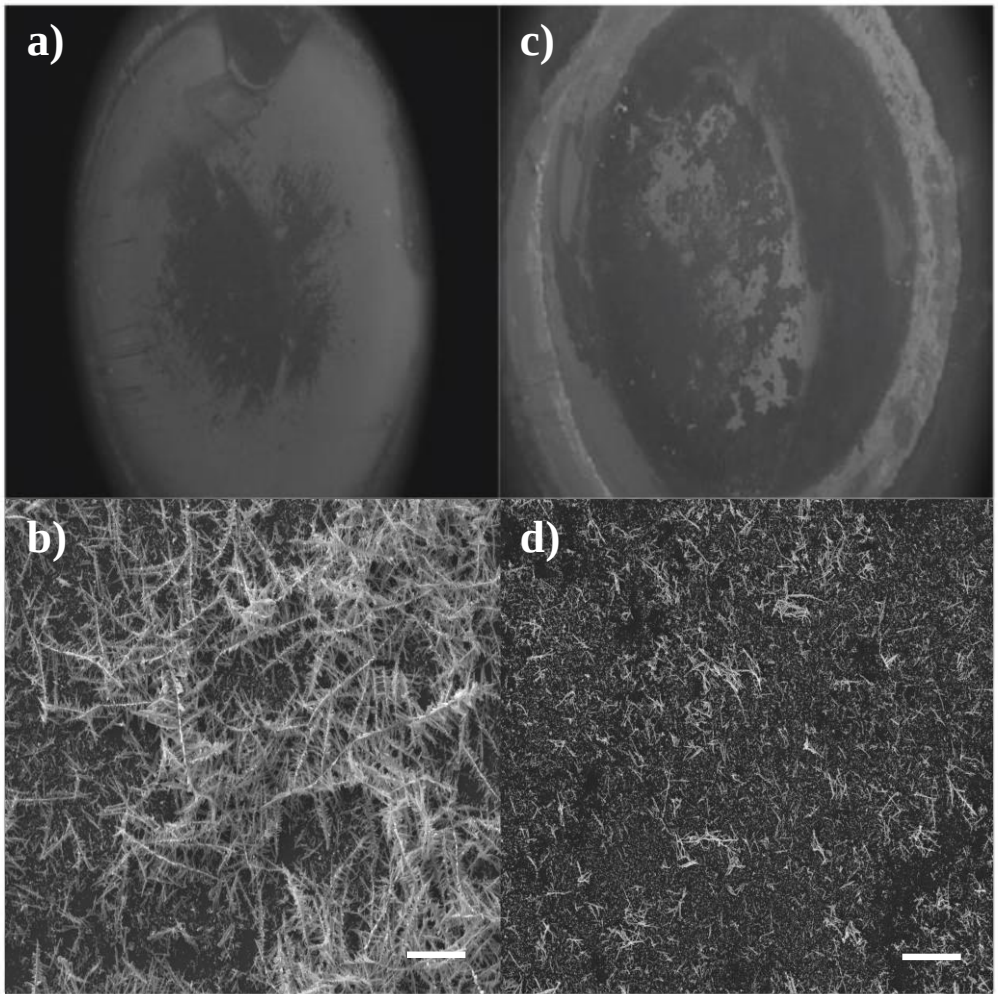

Figure 5.15 a) Top-down scanning electron micrograph of the deposited Bi crystals before electrolysis and b) high magnification image of the crystals in a). c) Top-down scanning electron micrograph of the deposited Bi crystals after electrolysis and d) high magnification image of the crystals in c). Scale bars: b) and d) 5 μm

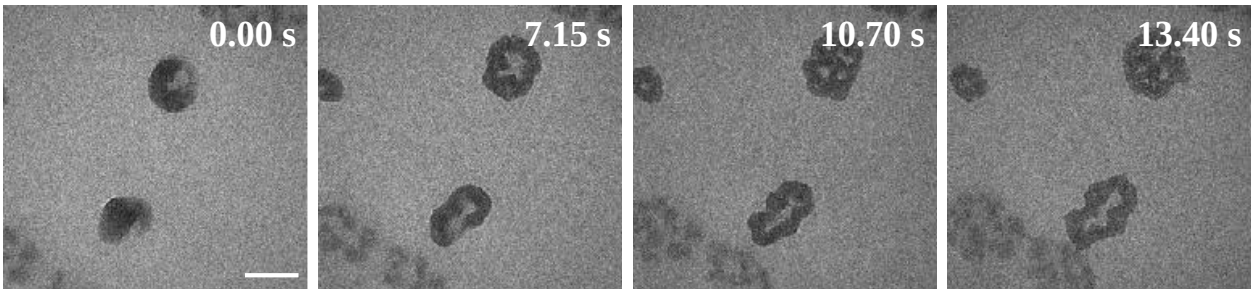

Figure 5.16 Frame grabs from a TEM video of two Bi nanoparticles deteriorating upon electron beam irradiation. Scale Bar: 50 nm

The cumulative data collected here suggest two points. First, at the potentials used in this study, Bi nanocrystals are unstable and dissolve away into solution. This point is consistent with the conversion to BiH_3(g). Second, the presence of Bi nanocrystals specifically allowed for the deposition of copious amounts of elemental Ge not possible under otherwise identical conditions. That is, the inclusion of Bi was necessary to realize thick Ge films. These films were particulate and poorly crystalline, yet arbitrarily thick. The mechanism was not unambiguously identified but the data are consistent with the possibility that bismuth hydrides are relevant. This aspect may explain a subtle detail in the use of Hg and Ga for ec-LLS in water. If accurate, the intentional inclusion of other hydrides (e.g. $NaBH_4$) may prove useful in the electrodeposition of group IV materials.

5.3 Summary

The conclusions from the preceding chapters bear direct relevance to the prospect of electrodeposition as a means to produce semiconductor materials. The un-finished work detailed in this chapter also suggests interesting new and underexplored directions. Further LC-TEM studies would provide valuable insight to the mechanism(s) of semiconductor nanowire growth by ec-LLS and potentially by ec-LSS. Further XRR work would provide separate atomic-level detail on how the solute and liquid metal interact. Future researchers aiming to resolve these works should aim to develop a strong skillset in the sample preparation, data collection, and data analysis for the techniques required to carry out the characterization techniques discussed in this chapter. Additionally, planning and committing to the plan of these complex experiments will be necessary to develop these ideas into publications. In addition to the obvious and implied direct experimental skills necessary to do electrochemistry, TEM work, and beamline analysis, the ability to program in a scientific coding language (preferably Python) is essential for the modeling and data analysis of these works. Automation of the data analysis (e.g., nanowire tacking) for the liquid TEM projects and pattern recognition algorithms will help further mine the data for insights beyond those described within this chapter.

5.4 References

1. Lensch-Falk, J. L.; Hemesath, E. R.; Perea, D. E.; Lauhon, L. J., Alternative catalysts for VSS growth of silicon and germanium nanowires. *Journal of Materials Chemistry* **2009,** *19* (7), 849-857.
2. Gunawan, O.; Guha, S., Characteristics of vapor–liquid–solid grown silicon nanowire solar cells. *Solar Energy Materials and Solar Cells* **2009,** *93* (8), 1388-1393.
3. Zhang, J.; Zheng, Y.; Zhao, D.; Yang, S.; Yang, L.; Liu, Z.; Zhang, R.; Wang, S.; Zhang, D.; Chen, L., Ellipsometric Study on Size-Dependent Melting Point of Nanometer-Sized Indium Particles. *The Journal of Physical Chemistry C* **2016,** *120* (19), 10686-10690.
4. Gu, J.; Collins, S. M.; Carim, A. I.; Hao, X.; Bartlett, B. M.; Maldonado, S., Template-Free Preparation of Crystalline Ge Nanowire Film Electrodes via an Electrochemical Liquid–Liquid–Solid Process in Water at Ambient Pressure and Temperature for Energy Storage. *Nano Letters* **2012,** *12* (9), 4617-4623.
5. Mahenderkar, N. K.; Liu, Y.-C.; Koza, J. A.; Switzer, J. A., Electrodeposited Germanium Nanowires. *ACS Nano* **2014,** *8* (9), 9524-9530.
6. Pereira, L.; Águas, H.; Martins, R. M.; Fortunato, E.; Martins, R., Polycrystalline silicon obtained by gold metal induced crystallization. *Journal of Non-Crystalline Solids* **2004,** *338-340*, 178-182.
7. Pereira, L.; águas, H.; Vilarinho, P.; Fortunato, E.; Martins, R., Metal induced crystallization: Gold versus aluminium. *Journal of Materials Science* **2005,** *40* (6), 1387-1391.
8. Yang, R.-Y.; Weng, M.-H.; Liang, C.-T.; Su, Y.-K.; Shy, S.-L., Low Temperature Metal Induced Crystallization of Amorphous Silicon by Nano-Gold-Particles. *Japanese Journal of Applied Physics* **2006,** *45* (No. 43), L1146-L1148.
9. Kodambaka, S.; Tersoff, J.; Reuter, M. C.; Ross, F. M., Germanium Nanowire Growth Below the Eutectic Temperature. *Science* **2007,** *316* (5825), 729.
10. DeMuth, J.; Ma, L.; Lancaster, M.; Acharya, S.; Cheek, Q.; Maldonado, S., Eutectic-Bismuth Indium as a Growth Solvent for the Electrochemical Liquid-Liquid-Solid Deposition of Germanium Microwires and Coiled Nanowires. *Crystal Growth & Design* **2018,** *18* (2), 677-685.
11. *Liquid Cell Electron Microscopy*. Cambridge University Press: Cambridge, 2016.
12. Fahrenkrug, E.; Alsem, D. H.; Salmon, N.; Maldonado, S., Electrochemical Measurements in In Situ TEM Experiments. *Journal of The Electrochemical Society* **2017,** *164* (6), H358-H364.
13. Acharya, S.; Ma, L.; Maldonado, S., Critical Factors in the Growth of Hyperdoped Germanium Microwires by Electrochemical Liquid–Liquid–Solid Method. *ACS Applied Nano Materials* **2018,** *1* (10), 5553-5561.
14. Pattadar, D.; Cheek, Q.; Sartori, A.; Zhao, Y.; Giri, R. P.; Murphy, B.; Magnussen, O.; Maldonado, S., Evidence for Facilitated Surface Transport during Ge Crystal Growth by Indium in Liquid Hg–In Alloys at Room Temperature. *Crystal Growth & Design* **2021,** *21* (3), 1645-1656.
15. Benbow, E. M.; Dalal, N. S.; Latturner, S. E., Crystal growth and magnetic behavior of R6T13−xAlxMy phases (R=La, Nd; T=Mn, Fe; M=main group) grown from lanthanide-rich eutectic fluxes. *Journal of Solid State Chemistry* **2009,** *182* (11), 3055-3062.
16. He, H.; Tyson, C.; Saito, M.; Bobev, S., Synthesis and structural characterization of the ternary Zintl phases AE3Al2Pn4 and AE3Ga2Pn4 (AE=Ca, Sr, Ba, Eu; Pn=P, As). *Journal of Solid State Chemistry* **2012,** *188*, 59-65.
17. Kanatzidis, M. G.; Pöttgen, R.; Jeitschko, W., The Metal Flux: A Preparative Tool for the Exploration of Intermetallic Compounds. *Angewandte Chemie International Edition* **2005,** *44* (43), 6996-7023.
18. Dumke, M. F.; Tombrello, T. A.; Weller, R. A.; Housley, R. M.; Cirlin, E. H., Sputtering of the gallium-indium eutectic alloy in the liquid phase. *Surface Science* **1983,** *124* (2), 407-422.
19. Metaferia, W.; Schulte, K. L.; Simon, J.; Johnston, S.; Ptak, A. J., Gallium arsenide solar cells grown at rates exceeding 300 μm h−1 by hydride vapor phase epitaxy. *Nature Communications* **2019,** *10* (1), 3361.

20. Tang, C.; Fan, S.; Lamy de la Chapelle, M.; Dang, H.; Li, P., Synthesis of Gallium Phosphide Nanorods. *Advanced Materials* **2000,** *12* (18), 1346-1348.
21. Regan, M. J.; Pershan, P. S.; Magnussen, O. M.; Ocko, B. M.; Deutsch, M.; Berman, L. E., Capillary-wave roughening of surface-induced layering in liquid gallium. *Physical Review B* **1996,** *54* (14), 9730-9733.
22. Regan, M. J.; Tostmann, H.; Pershan, P. S.; Magnussen, O. M.; DiMasi, E.; Ocko, B. M.; Deutsch, M., X-ray study of the oxidation of liquid-gallium surfaces. *Physical Review B* **1997,** *55* (16), 10786-10790.
23. Plech, A.; Klemradt, U.; Metzger, H.; Peisl, J., In situ x-ray reflectivity study of the oxidation kinetics of liquid gallium and the liquid alloy ? *Journal of Physics Condensed Matter* **1998,** *10*, 971.
24. Pourbaix, M., *Atlas of electrochemical equilibria in aqueous solutions*. 2d English ed.; National Association of Corrosion Engineers: Houston, Tex., 1974; p 644 p.
25. Fahrenkrug, E.; Gu, J.; Maldonado, S., Electrodeposition of Crystalline GaAs on Liquid Gallium Electrodes in Aqueous Electrolytes. *Journal of the American Chemical Society* **2013,** *135* (1), 330-339.
26. Fahrenkrug, E.; Rafson, J.; Lancaster, M.; Maldonado, S., Concerted Electrodeposition and Alloying of Antimony on Indium Electrodes for Selective Formation of Crystalline Indium Antimonide. *Langmuir* **2017,** *33* (37), 9280-9287.
27. Jacobs-Gedrim, R. B.; Shanmugam, M.; Jain, N.; Durcan, C. A.; Murphy, M. T.; Murray, T. M.; Matyi, R. J.; Moore, R. L.; Yu, B., Extraordinary Photoresponse in Two-Dimensional In2Se3 Nanosheets. *ACS Nano* **2014,** *8* (1), 514-521.
28. Julien, C.; Eddrief, M.; Kambas, K.; Balkanski, M., Electrical and optical properties of In2Se3 thin films. *Thin Solid Films* **1986,** *137* (1), 27-37.
29. Zhou, Y.; Wu, D.; Zhu, Y.; Cho, Y.; He, Q.; Yang, X.; Herrera, K.; Chu, Z.; Han, Y.; Downer, M. C.; Peng, H.; Lai, K., Out-of-Plane Piezoelectricity and Ferroelectricity in Layered α-In2Se3 Nanoflakes. *Nano Letters* **2017,** *17* (9), 5508-5513.
30. Czerniawski, J. M.; Stickney, J. L., Electrodeposition of In2Se3 Using Potential Pulse Atomic Layer Deposition. *The Journal of Physical Chemistry C* **2016,** *120* (29), 16162-16167.
31. Mukherjee, S.; Dutta, D.; Mohapatra, P. K.; Dezanashvili, L.; Ismach, A.; Koren, E., Scalable Integration of Coplanar Heterojunction Monolithic Devices on Two-Dimensional In2Se3. *ACS Nano* **2020,** *14* (12), 17543-17553.
32. Weszka, J.; Daniel, P.; Burian, A.; Burian, A. M.; Nguyen, A. T., Raman scattering in In2Se3 and InSe2 amorphous films. *Journal of Non-Crystalline Solids* **2000,** *265* (1), 98-104.
33. Weszka, J.; Daniel, P.; Burian, A. M.; Burian, A.; Elechower, M.; Nguyen, A. T., Raman scattering in amorphous films of In1−xSex alloys. *Journal of Non-Crystalline Solids* **2003,** *315* (3), 219-222.
34. Carolan, D.; Doyle, H., Size Controlled Synthesis of Germanium Nanocrystals: Effect of Ge Precursor and Hydride Reducing Agent. *Journal of Nanomaterials* **2015,** *2015*, 506056.
35. Wu, J.; Sun, Y.; Zou, R.; Song, G.; Chen, Z.; Wang, C.; Hu, J., One-step aqueous solution synthesis of Ge nanocrystals from GeO2 powders. *CrystEngComm* **2011,** *13* (11), 3674-3677.
36. Romann, T.; Lust, E., Electrochemical properties of porous bismuth electrodes. *Electrochimica Acta* **2010,** *55* (20), 5746-5752.
37. Parker, J. H.; Feldman, D. W.; Ashkin, M., Raman Scattering by Silicon and Germanium. *Physical Review* **1967,** *155* (3), 712-714.
38. Lannin, J. S.; Maley, N.; Kshirsagar, S. T., Raman scattering and short range order in amorphous germanium. *Solid State Communications* **1985,** *53* (11), 939-942.